Spring 2019

THE SAUDI ARAMCO JOURNAL OF TECHNOLOGY
A quarterly publication of the Saudi Arabian Oil Company

Saudi Aramco

Journal of Technology

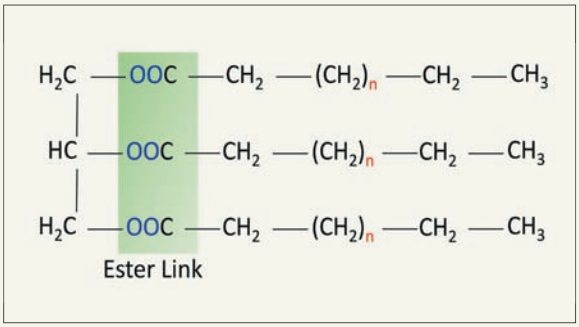

Triglycerides present in waste vegetable oil are the potential source of fatty acids and their derivatives, which have several applications in the drilling fluids industry.

On the Cover

Fatty acids and their derivatives have been used as emulsifiers, lubricants, etc., in drilling fluids. Waste vegetable oil is a good source of triglycerides. Fatty acids and the methyl ester of fatty acids can be isolated from triglycerides by a simple base hydrolysis. These in-house developed products show exceptional properties as primary emulsifiers for invert-emulsion oil-based mud (OBM), and as lubricants for water-based mud and base oil for OBM.

MORE SAUDI ARAMCO JOURNAL OF TECHNOLOGY ARTICLES AVAILABLE ON THE INTERNET.

Additional articles that were submitted for publication in the *Saudi Aramco Journal of Technology* are being made available online. You can read them at this link on the Saudi Aramco Internet Website: www.saudiaramco.com/jot

The *Saudi Aramco Journal of Technology* is published quarterly by the Saudi Arabian Oil Company, Dhahran, Saudi Arabia, to provide the company's scientific and engineering communities a forum for the exchange of ideas through the presentation of technical information aimed at advancing knowledge in the hydrocarbon industry.

Complete issues of the Journal in PDF format are available on the Internet at: http://www.saudiaramco.com (click on "publications").

SUBSCRIPTIONS

Send individual subscription orders, address changes (see page 84) and related questions to:

Saudi Aramco Corporate Communications
Support Department
JOT Distribution
Box 5000
Dhahran 31311, Saudi Arabia
Website: www.saudiaramco.com/jot

CONTRIBUTIONS

Relevant articles are welcome. Submission guidelines are printed on the last page. Please address all manuscript and editorial correspondence to:

EDITOR

William E. Bradshaw
The *Saudi Aramco Journal of Technology*
C-11B, Room AN-1080
North Admin Building #175
Dhahran 31311, KSA
Tel: +966-013-876-0498
Email: william.bradshaw.1@aramco.com.sa

Unsolicited articles will be returned only when accompanied by a self-addressed envelope.

PRODUCTION COORDINATION

Richard E. Doughty

DESIGN

Graphic Engine Design Studio,
Austin, Texas, U.S.A.

ISSN 1319-2388.

The *Saudi Aramco Journal of Technology* gratefully acknowledges the assistance, contribution and cooperation of numerous operating organizations throughout the company.

أرامكو السعودية
saudi aramco

Spring 2019

THE SAUDI ARAMCO JOURNAL OF TECHNOLOGY
A quarterly publication of the Saudi Arabian Oil Company

Saudi Aramco Journal of Technology

Contents

Waste Cooking Oil — A Potential Source of Raw Material for Localization of Green Products Development

Dr. Md. Amanullah, Mohammed K. Arfaj, and Dr. Jothibasu Ramasamy

ABSTRACT

The oil and gas industry has a long-standing initiative to develop and use the most environmental solutions in the exploration and recovery of oil and gas resources. As part of this continual effort, research is ongoing to create eco-friendly, virtually nontoxic and readily biodegradable base fluids, lubricants, and emulsifiers to successfully complete drilling and completion requirements, without causing any damage to the environment or other resources.

There is a significant volume of waste vegetable oil (WVO) generated by the food and catering industry, which has no aromatic oil content, is virtually nontoxic, and readily biodegradable, and therefore, can be a potential source for the development of eco-friendly base fluids, lubricants, emulsifiers, and spotting fluids to be in the forefront of best drilling practices. This article describes a set of newly developed green mud additives that have been synthesized using waste cooking oil generated by the food and catering industry. Recycling of the waste cooking oil not only provides a technical solution for the oil and gas industry, but also addresses the disposal problems of the food and catering industry.

Experimental results demonstrating the various applications of the newly developed green products indicate similar or better performance compared to the commercially available equivalent products used by the oil and gas industry. Subsequently, the newly developed products are viable alternatives for some of the imported non-eco-friendly or less eco-friendly oil-based products, used for exploration and exploitation of oil and gas resources. Due to the replacement of equivalent imported products, these locally developed products will significantly reduce the mud additive import cost. Also, due to the eco-friendly nature of these products, they will help in the exploration and exploitation of oil and gas resources without causing any negative impact on other marine and terrestrial resources.

INTRODUCTION

The oil and gas industry uses various types of chemicals and additives to design various fluid systems to explore and exploit hydrocarbon resources to meet the global energy demand. Some of these additives and products are not eco-friendly and therefore have serious limitations in their applications, due to their detrimental impact on the surrounding environments, including ecosystems, habitats, water resources, farming lands, the local population, and rig site workers, etc.[1-3].

That's why the regional, federal and global environmental agencies are enacting increasingly strict environmental rules and regulations to safeguard the local, regional, and global environments, and also to avoid any short- and long-term detrimental impact on marine and terrestrial resources, habitats, population, etc. Due to the concern of the global communities, the industry has realized the need for a replacement for the non-eco-friendly additives and fluids — to be in the forefront of the best drilling practices. There is an expected annual growth of 7% to 10% of eco-friendly lubricants in the U.S. market over the next few years, compared to an overall 2% growth rate of conventional lubricants. This is reflected in the increasing research to develop green additives and base fluids to replace or reduce the use of less eco-friendly additives and products[3, 4-6].

Currently, many countries of the world have prohibited the use of non-eco-friendly additives and fluids in environmentally sensitive areas, to prevent damage and degradation of the environment and surrounding ecosystems. The operating companies all over the world take extra care to avoid any damage and degradation of the environment by introducing new products in the market and providing well-defined operational guidelines. In spite of strict operational guidelines, accidental spills, leakage and discharge of any less eco-friendly products in the surrounding environment can cause environmental damage and pollution to the water systems, farming land, top soil, coastal areas, etc. Therefore, identification of a better alternative is always encouraged by the industry.

The oil-based muds (OBMs) leaked or disposed after washing the mud tanks, mud pumps, and flow lines, may travel into the surrounding ecosystems, water reserves, subsurface water table, etc., and can cause serious contamination due to the incorporation of benzene-like toxins in the surface and subsurface water system. Its detrimental impact — both on the soil and drinking water — could be a serious health hazard for the surrounding environment, habitats, and

population. The rain and storm water runoff can also carry the residual hydrocarbon wastes into the canals, lakes, rivers, and oceans, leading to damage and degradation of the water system, and also the contamination of the marine and coastal areas. Subsequently, replacement of the diesel, mineral, and synthetic oil-based products by eco-friendly, nontoxic and readily biodegradable products is the best strategy to safeguard the global environment.

Vegetable oils (VOs) generated by the agricultural industry, and the waste vegetable oils (WVOs) generated by the food and catering industry, have a renewable source of supply for sustainable product development, and are potential candidates for green additives development for the oil and gas field, and other industrial applications. According to Amanullah and Arfaj (2017)[7] the food industry has the priority for VOs over other industries to avoid any negative impact on the consumer market; therefore, WVO is the most suitable candidate.

The WVOs produced by the food and catering industry have no major industrial uses other than their use in manufacturing some soap and animal feeds, and is thereby usually discarded as a waste product, especially in underdeveloped countries. According to Chhetri et al. (2008)[8] even though some of this WVO is used for soap production, a major part of it is discharged into the environment due to the lack of any recycling and reuse processing for other industrial applications. Like the pure VOs, the waste cooking oil is eco-friendly, readily biodegradable, and virtually nontoxic and organic in nature. It has no aromatic and sulfur content like hydrocarbon oils and also has no occupational health and safety (OHS) issues like diesel and mineral oils (MOs). Waste cooking oil is a perpetual waste product generated by the food and catering industry, and thereby provides a sustainable source of supply of raw materials for green product development for current and future industrial applications. Because of the lack of a viable disposal route, most of the WVO is discharged into the surrounding environment. Therefore, its use as a raw material for green product development will solve the overall disposal problem, and will also ensure a sustainable source of supply of eco-friendly additives for exploration and exploitation of oil and gas resources, without any damage or degradation of other marine and terrestrial resources.

The high fire and flash points of VO, along with WVO, ensures a much lower risk of causing fire hazards. Therefore, its application in high-pressure, high temperature (HPHT) environments will reduce the probability and likelihood of causing a fire during handling, mixing, transporting, etc. Due to the absence of any toxic materials in the WVO composition, it has no or negligible occupational health issues, and is therefore very friendly for occupational health, safety, and environmental purposes. The safe nature of the WVOs and their derivatives dramatically reduces the risk of creating any occupational health hazards. Amanullah and Arfaj (2017)[7], Srivastava and Prasad (2000)[9], How et al. (2012)[10], and Sidibé et al. (2010)[11], have all provided a comprehensive description of the advantages of vegetable or WVO-based base fluids and other products, over diesel and mineral oil-based products.

DEVELOPMENT STRATEGY

The goal of this innovative research of using WVO as a raw material to produce eco-friendly green products is far-reaching. One of the major objectives is to provide a sustainable source of locally developed eco-friendly products to replace the equivalent commercial products imported for oil and gas field applications. The second objective of the research is to provide a complete localization of product development by identifying eco-friendly raw materials that are available locally for green product development for the oil and gas field applications. Therefore, emphasis was given not to use any raw materials that are not locally available. The third objective is to provide a sustainable source of raw material development, e.g., lubricants, emulsifiers, and base stocks, as the hydrocarbon-based oil has a finite source of supply.

The fourth objective is to solve the disposal problem of food and catering industries by identifying a viable commercial route for the disposal of a huge volume of WVO generated by the industry each year. The fifth objective of this innovative research is to play a pivotal role in the growth of existing industries and development of new industries and enterprises to capture the local, regional, and part of the global additive market. The sixth objective is the creation of new job opportunities for the public and low income people to uplift their social and economic conditions and fulfill the citizenship charter of the company.

PHYSICAL PROCESSING AND CHEMICAL MODIFICATION

The WVO as received is not suitable to use as a base fluid, emulsifier or lubricant for oil and gas field applications due to some unfavorable technical characteristics such as the presence of suspended particles and food debris, high viscous

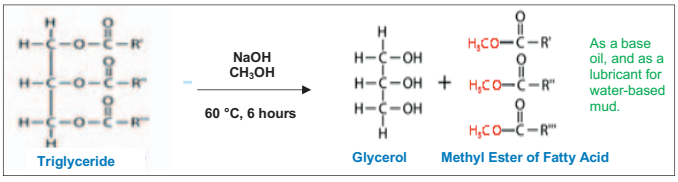

Fig. 1. Diagram showing the chemical modification of WVO using CH_3OH and NaOH.

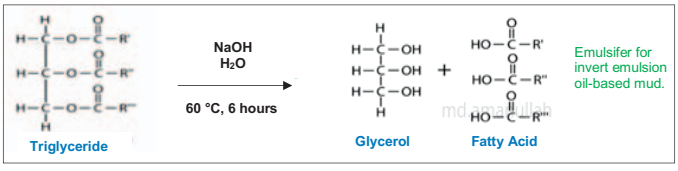

Fig. 2. Diagram showing the chemical modification of WVO using water and NaOH.

characteristics, low oxidative stability, and poor low temperature flow behavior, etc. Subsequently, an initial physical treatment was conducted using a filter paper, and a low-pressure test chamber to remove the dispersed particles and any large food debris from the waste cooking oil. After physical treatment, chemical modification was done by water hydrolysis and methanol (CH_3OH) esterification to improve the viscous characteristics, low temperature flow behavior, and interface infiltration characteristics. Figures 1 and 2 show the two chemical modification methods used and the reaction products generated by the interactions. Figure 1 shows esterification using CH_3OH and sodium hydroxide (NaOH), and Fig. 2 shows a chemical modification using water and NaOH.

GREEN PRODUCTS

The WVO-based base stocks developed by hydrolysis and an esterification process were used to developed eco-friendly OBM and a spotting fluid known as ARC Eco-Spot. The base stocks were also used to assess their suitability as lubricants, to reduce the frictional resistance of water-based muds (WBMs) and emulsifiers, to create a stable and tight emulsion in invert emulsion mud systems. A detailed description of the experimental results along with the interpretation of the data are given next.

Eco-Friendly Base Stock

The esterification process provided an eco-friendly base stock with viscous characteristics similar to mineral, diesel, and a highly refined Saudi Arabian oil (SAO) widely used as the base stocks for conventional OBM development. Figure 3 shows the rheological profile (viscous characteristics) of the original WVO and WVO ester produced after chemical modification, along with the rheological profiles of diesel and MO. The data clearly indicates very high viscous characteristics for the WVO. That's why the as received WVO is not suitable for development of an OBM system with desirable mud properties. After chemical processing, the refined WVO (RWVO) shows a viscous profile very similar to the viscous profiles of diesel and MOs. This indicates its suitability to use as a base stock for a new generation of OBM development with technical performance similar or equivalent to the conventional diesel and mineral OBMs. Due to the eco-friendly nature of the

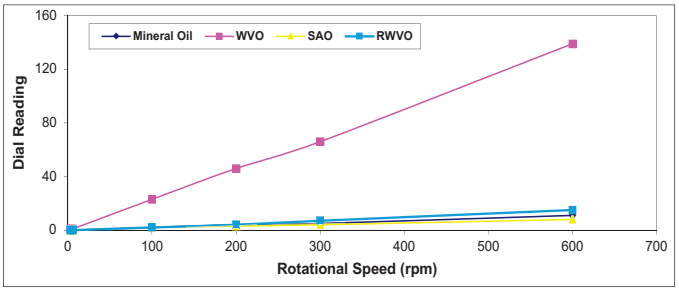

Fig. 3. Rheological profiles of the MO, WVO, SAO, and RWVO-based base fluid.

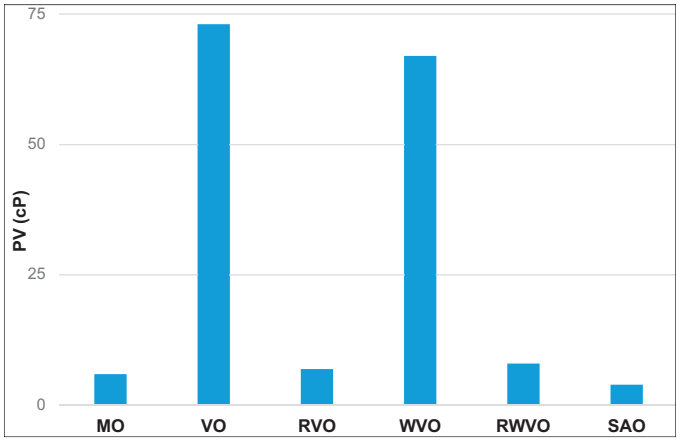

Fig. 4. PV values of MO, VO, RVO, WVO, RWVO, and SAO.

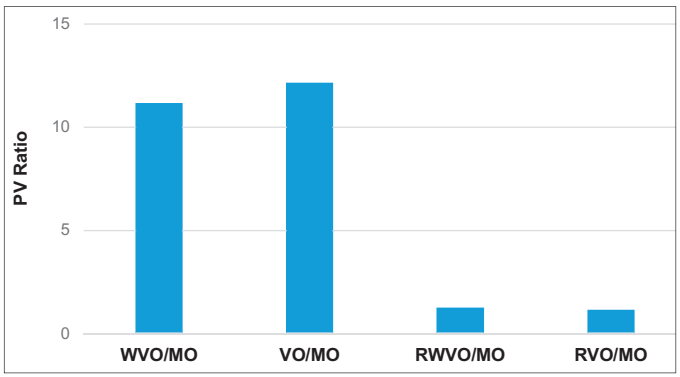

Fig. 5. PV ratios of VO, RVO, WVO, RWVO with respect to the PV value of the MO.

base stock, it will provide an OBM system with environmental characteristics similar to WBM systems.

The comparison of plastic viscosity (PV) values of the MO shown in Fig. 4 with the PV values of VO, refined VO (RVO), WVO, RWVO, and SAO indicate extremely high PV values for VO and WVO with respect to the PV value of the MO, but close PV values for the RVO and RWVO. This indicates that the original VO and WVO are not suitable for a functional OBM formulation, due to excessive PV values. After chemical modification, these oils have PV values close to the MO's PV, and is thereby suitable for OBM formulations.

Figure 5 shows the analyses of the PV ratios of VO and MO, WVO and MO, RVO and MO, and RWVO and MO. The data indicates more than 11 times higher PV ratios for the as received VO and WVO, but less than 1.5 PV ratios for the RVO and RWVO. This again demonstrates the suitability of the chemically modified VO and WVO for developing a new generation of OBM systems with superior environmental properties. The marginally higher PV values of RVO and RWVO will have a positive impact as it will reduce the amount of geltone necessary to produce desirable mud properties for efficient cuttings suspension and hole cleaning.

Eco-Friendly OBM

An eco-friendly RWVO OBM with a 70/30 oil-water ratio

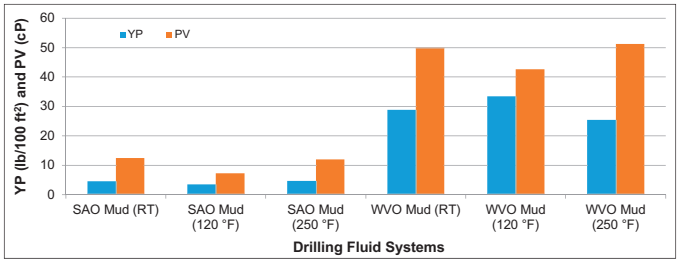

Fig. 6. Comparison of PV and YP of SAO and WVO OBM.

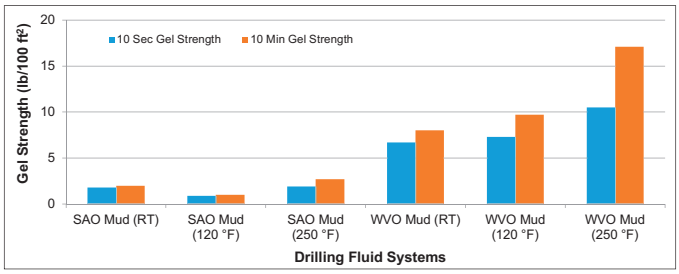

Fig. 7. Comparison of 10 seconds and 10 minutes gel strength of the SAO and WVO OBM.

was formulated using the WVO-based base stock to assess its suitability to formulate an eco-friendly OBM system. Due to the non-aqueous and eco-friendly nature of the base stock, it will perform technically like a conventional OBM system and environmentally like a conventional WBM system, to explore oil and gas resources without causing any detrimental impact to other marine and terrestrial resources.

The PV and yield point (YP) data of the SAO and the WVO OBM, Fig. 6, clearly indicates a much better rheological property for the WVO OBM compared to the PV and YP values of a conventional OBM system. Therefore, the newly developed RWVO OBM will provide better cuttings carrying capacity, and also hole cleaning efficiency compared to the conventional OBM system. The analyses of the 10 seconds and 10 minutes gel strength of the SAO and the WVO OBM, Fig. 7, also indicate superior properties for the RWVO OBM system. The higher gel strength of the mud will ensure excellent cuttings suspension capacity after the cession of the drilling operation. Measurement at room temperature, at 120 °F and also after thermal aging at 250 °F, indicates superior properties for the RWVO OBM system compared to the conventional OBM system.

Green Lubricants Development

Two methods of chemical modification of the WVO, previously shown in Fig. 2, provided two base stocks as the end products. Initially, the first base stock developed by esterification of the WVO was tested using a standard lubricity tester to evaluate its performance as an eco-friendly lubricant. This lubricant product is known as ARC Eco-lube. Figure 8 clearly indicates that the RWVO derived lubricant, ARC Eco-Lube, has good friction reducing properties. That's why it was able to knock down the coefficient of friction (COF) value of bentonite mud from 0.344 to 0.126 — an approximate 63% reduction of the COF value of the original bentonite mud. Comparison of the lubricating performance of the ARC Eco-Lube with respect to the commercial green lubricant (CGL) indicates somewhat better performance for the ARC Eco-Lube with respect to the CGL.

In the case of the low solids non-dispersed (LSND) mud system, the ARC Eco-Lube showed lubricating performance similar or better than diesel, SAO, and MOs, and thereby demonstrates good lubricating potential, Fig. 9. The data clearly indicates an approximate 29% decrease in the COF value with respect to the original COF value of the LSND mud. Comparison of the lubricating performance of the ARC Eco-Lube with respect to the CGL indicates better performance for the CGL. This performance difference may be due to the presence of additional lubricating chemicals in the CGL. It may be mentioned that no additional materials were added in the ARC Eco-Lube to enhance its lubricating potential. The data undoubtedly proves that the base stock developed after esterification has significant potential to be used as a green lubricant for oil and gas field applications.

The second eco-friendly lubricant developed after treatment of the WVO using water + NaOH is known as the ARC Veg-Lube. Its performance was tested and evaluated in four different WBMs such as calcium chloride ($CaCl_2$) mud, LSND mud, a potassium chloride (KCl) polymer mud, and bentonite mud, Fig. 10. Again, a CGL was also used for comparative

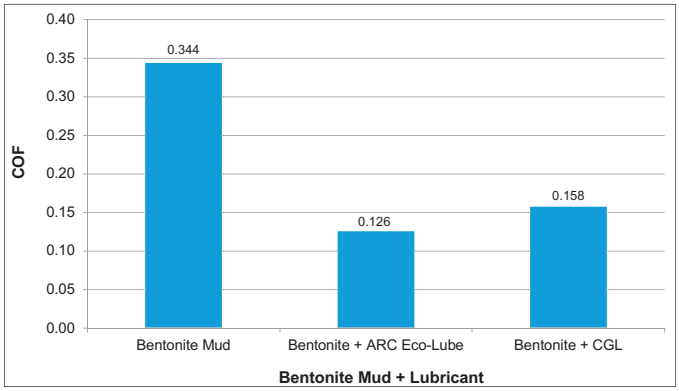

Fig. 8. The COF value of bentonite mud, bentonite mud + ARC Eco-Lube, and bentonite mud + CGL.

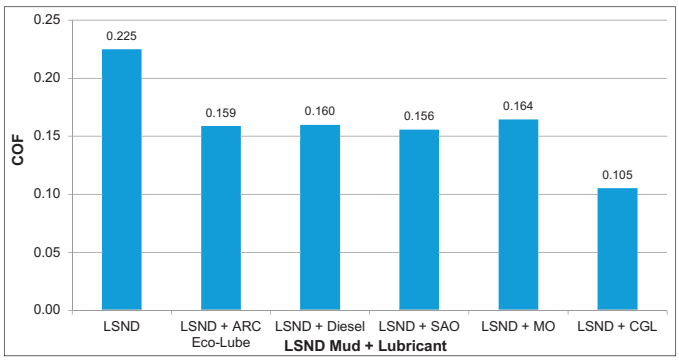

Fig. 9. The COF value of the LSDN mud, LSDN mud + ARC Eco-Lube, LSDN mud + diesel, LSDN mud + SAO, LSDN mud + MO, and LSDN mud + CGL.

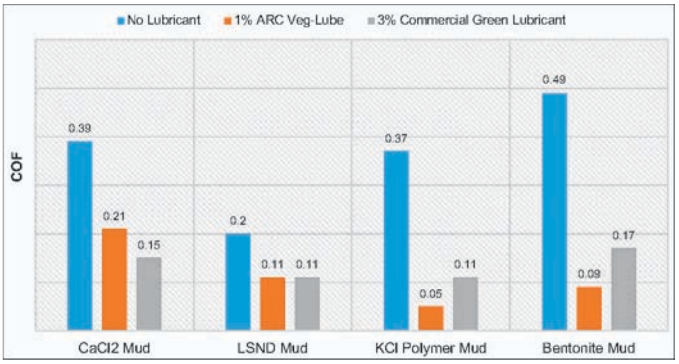

Fig. 10. Comparative evaluation of the performance of WVO oil-based green lubricant — ARC Veg-Lube in the presence of various WBM systems.

assessment of the performance of the newly developed green lubricant ARC Veg-Lube. The data clearly shows that even at a 1% concentration, the newly developed green lubricant was able to significantly knock down the COF values of all the mud systems. This observation is reflected by a 46% reduction in the COF value of the $CaCl_2$ mud, 45% reduction of the COF value of the LSND mud, 86% reduction of the COF value of the KCl polymer mud, and an 82% reduction of the COF value of the bentonite mud. With respect to the 3% CGL containing mud, the 1% ARC Veg-Lube containing mud showed a lower performance in the $CaCl_2$ mud, a similar performance in the LSND mud, and a better performance in the KCl polymer and bentonite mud.

Eco-Friendly Emulsifier

An eco-friendly emulsifier known as ARC Eco-Mul was synthesized by chemical modification of WVO by treating it with water and a NaOH solution to isolate the glycerol and the fatty acids. After the glycerol and fatty acid separation reaction, the alkaline fatty acid was washed using brine, followed by acid neutralization to prepare the base stock and use as an eco-friendly emulsifier for the creation of a tight emulsion in an invert emulsion mud system. To evaluate the performance of the newly developed emulsifier, an OBM was formulated and prepared using the newly developed ARC Eco-Mul as the primary emulsifier. Another mud was also prepared using the same amount of a commercial primary emulsifier known as Invermul®, Table 1. The effectiveness of the new and the conventional emulsifiers were evaluated by measuring the electrical stability (ES) values, and fluid loss behavior of the mud systems.

Figure 11 shows the ES values of the OBM + commercial primary emulsifier containing mud, along with the ES values of the OBM + ARC Eco-Mul. The results indicate good ES values for both of the mud systems. A comparative assessment of the ES values of the two mud systems shows higher ES values for the OBM containing commercial emulsifier. Both of them created a tight emulsion in the invert emulsion mud systems. This was reflected by having no separation of the phases, both before and after the hot rolling at 300

Mud System	Formulation Invermul®	Formulation
ARC Eco-Mul		
SAO (ml)	218	218
Invermul® (ml)	12	0
ARC Eco-Mul (ml)	0	12
EZ-mul (ml)	4	4
Lime (g)	6	6
Geltone (g)	4	4
Duratone (g)	6	6
Brine (61 g $CaCl_2$ in 85 cc water) (ml)	85	85
Barite (g)	161	161

Table 1. Invert emulsion mud formulation using Invermul® and ARC Eco-Mul

°F. Therefore, the results demonstrate the suitability of the WVO-based emulsifier for designing OBM systems with ES values that are sufficient to create a tight emulsion in the mud system.

Figure 12 shows the HPHT spurt and fluid loss behavior of the new and commercial emulsifier containing muds measured at 300 °F and 500 psi. The data clearly indicates the superior fluid loss behavior of the ARC Eco-Mul containing mud system compared to the mud containing the commercial primary emulsifier. Due to the ability of the emulsifier to create a tighter and stable emulsion, there was no spurt loss in the mud containing the newly developed primary emulsifier. The tightness of the emulsion is further reflected by a very low all oil

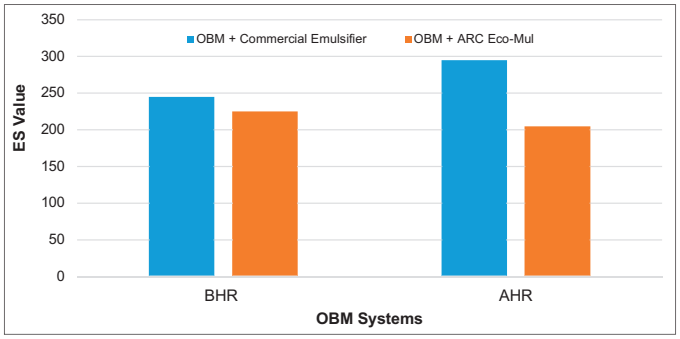

Fig. 11. The ES values of the OBM + commercial emulsifier containing mud, and the OBM + ARC Eco-Mul.

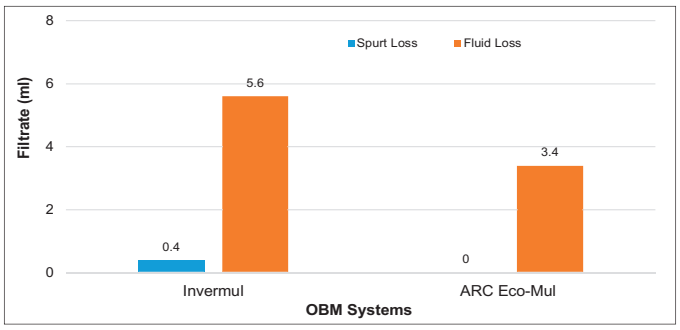

Fig. 12. The HPHT spurt and fluid loss of the Invermul® and ARC Eco-Mul formulation (tested at 300 °F and a pressure of 500 psi).

Mud System				
O/W Ratio	**80/20**	**80/20**	**80/20**	**80/20**
SAO (cc)	218	218	218	218
ARC Eco-Mul (cc)	12	6	4	0
EZ-Mul (cc)	4	4	4	4
Lime (g)	6	6	6	6
Geltone (g)	4	4	4	4
Duratone (g)	6	6	6	6
Brine (61 g $CaCl_2$ in 56.6 cc water	85	85	85	85
Barite (g)	161	161	161	161

Table 2. Screening of the concentration of ARC Eco-Mul to identify the optimum range

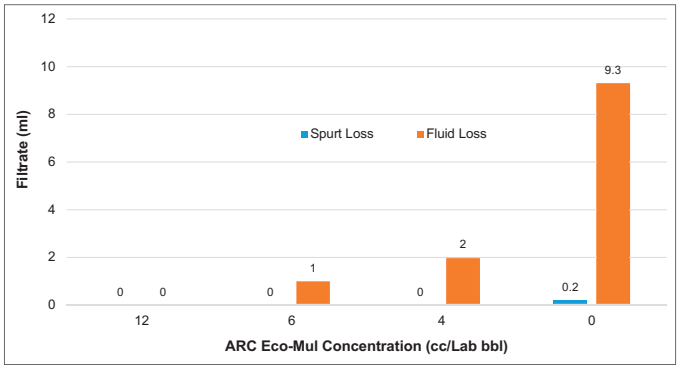

Fig. 13. The API spurt and fluid loss for formulations having different concentrations of ARC Eco-Mul.

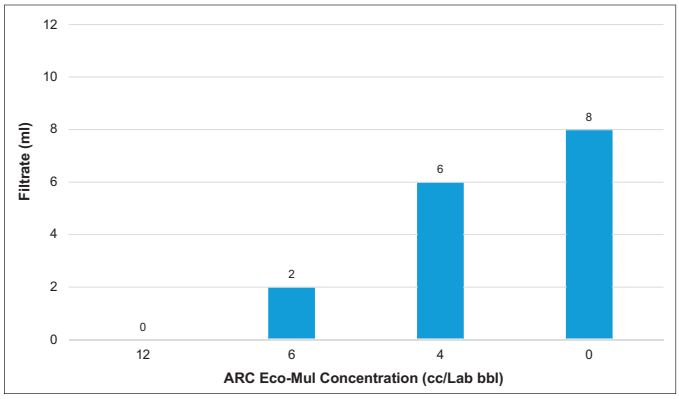

Fig. 14. The HPHT spurt loss for formulations having different concentrations of ARC Eco-Mul (tested at 300 °F and a pressure of 500 psi).

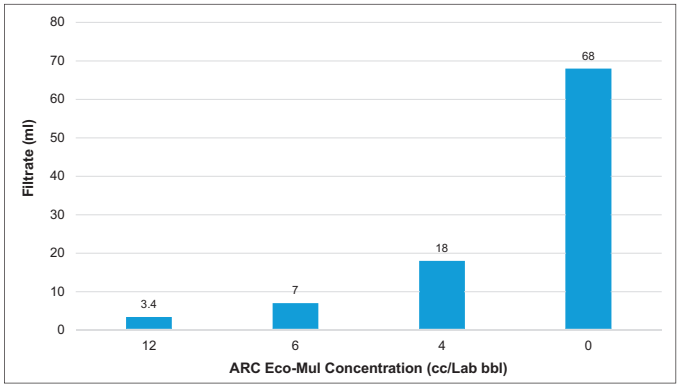

Fig. 15. The HPHT fluid loss for formulations having different concentrations of ARC Eco-Mul (tested at 300 °F and a pressure of 500 psi).

HPHT fluid loss. The OBM system containing the commercial primary emulsifier has a higher fluid loss and slight spurt loss.

OBM systems with different concentrations of ARC Eco-Mul were formulated to identify the optimum concentration range of the ARC Eco-Mul, Table 2. API and HPHT fluid loss behavior were used to define the optimum concentration range.

Figure 13 shows the API fluid loss behavior of the OBM system in the presence of different concentrations of the ARC Eco-Mul. The data clearly shows the requirement of at least 6 cc of ARC Eco-Mul to maintain the spurt and API fluid loss behavior close to zero. OBM containing 12 ppb of ARC Eco-Mul shows virtually no spurt and API fluid loss. According to the API test results, it could be concluded that an optimum concentration range of 8 ppb to 12 ppb will be able to create a tight emulsion with desirable mud properties.

Figure 14 shows the HPHT spurt loss measured at 300 °F and 500 psi using various concentrations of ARC Eco-Mul. The data clearly indicates some spurt loss at a concentration of 6 cc/350 cc lab mud, and a higher spurt loss with a reduced concentration. The OBM with an ARC Eco-Mul concentration of 12 ppb shows virtually no spurt loss. Based on this information, it can be concluded that a concentration range of 8 cc to 12 cc for 350 cc of lab mud will provide desirable HPHT fluid loss behavior.

Figure 15 shows the HPHT fluid loss measured at 300 °F and 500 psi using various concentrations of ARC Eco-Mul. The data clearly indicates acceptable HPHT fluid loss behavior at a concentration of 6 ppb and higher. The OBM with a 12 cc ARC Eco-Mul concentration shows only 3.4 cc fluid loss. The data again indicates that a concentration range of 8 cc to 12 cc per lab bbl of OBM (1 lab bbl = 350 cc) is sufficient enough to provide a good invert emulsion mud system with a desirable HPHT fluid loss behavior.

Eco-Friendly Spotting Fluid

Pipe sticking while drilling is one of the major drilling challenges that we face in most of our drilling operations. Some of the critical factors that can trigger a pipe sticking event are

improper drilling practices, inadequate hole cleaning, wellbore instability, excessive reaming or back reaming, poor mud rheology, deposition of thick mud cake, the presence of a high permeable formation, quality of the mud, and the deposited mud cakes, etc.[12-15].

Various types of aqueous and non-aqueous spotting fluids are used by the industry to recover a stuck pipe. Conventional non-aqueous spotting fluids are commonly designed using diesel, MOs, or base stocks derived from these oils. Due to negative environmental characteristics, poor biodegradation properties and unacceptable toxicity, these oils have severe restrictions for sensitive environments. Therefore, the industry needs an eco-friendly base stock to formulate green spotting fluids to overcome the limitations of non-eco-friendly spotting fluids used by the industry. Bearing this in mind, an eco-friendly base stock derived from WVO has been used to formulate a green spotting fluid known as ARC Eco-Spot. Table 3 shows the formulation of the ARC Eco-Spot along with three conventional spotting fluids to compare and evaluate the performance of the newly developed ARC Eco-Spot.

To evaluate the performance of the ARC Eco-Spot, tests were conducted to determine the sticking bond modulus (SBM), and ultimate sticking bond strength (USBS) of a 10 mm thick mud cake, deposited by a weighted KCl polymer mud in the absence of any spotting fluid, to use as base line information. Table 3 lists the various spotting fluids used to evaluate their ability to reduce the SBM and the USBS. The mud cake was prepared by running a filtration test for more than 48 hours at 100 psi and at an ambient temperature[7]. The tests were conducted after 6 and 16 hours of soaking time, using mud cake of a similar thickness, and deposited by the same drilling mud, i.e., weighted KCl polymer mud. Figures 16 to 19 show the SBM and the USBS of the base mud cake, and also the mud cakes tested after 6 and 16 hours of soaking time in the presence of various spotting fluids, respectively.

Figure 16 shows the average SBM of the original mud cake and also the mud cakes soaked for 6 hours in various spotting fluids. A comparison of average SBMs of the original mud cake and the various spotting fluid soaked mud cakes indicate that all the spotting fluids reduce the SBM of the mud cake as a result of weakening, damage, and degradation of the sticking bonds, due to the interactions of the spotting fluids with the mud cakes at the mud cake spherical foot interface. The data further shows that the glycol-based spotting fluid, fluid C, shows the maximum reduction in SBM, the non-environment friendly spotting fluid, fluid B, caused the second maximum reduction in the SBM after 6 hours of soaking time, and spotting fluid A shows the minimum reduction in SBM.

Spotting Fluid A			
Components	**Field Formulation (bbl)**	**Concentration (%)**	**Lab Formulation (cc)**
Diesel	64	0.64	224
E-Z Spot	8	0.08	28
Water	28	0.28	98
Total Volume	100		350
Spotting Fluid B			
Components	**Field Formulation (bbl)**	**Concentration (%)**	**Lab Formulation (cc)**
Diesel	64	0.64	224
Pipe-Lax	8	0.08	28
Water	28	0.28	98
Total Volume	100		350
Spotting Fluid C			
Components	**Field Formulation (bbl)**	**Concentration (%)**	**Lab Formulation (cc)**
Glycol	85	0.80	281
Lubricant	16	0.15	52
Pipe-Lax	5	0.05	17
Total Volume	106		350
ARC Eco-Spot			
Components	**Field Formulation (bbl)**	**Concentration (%)**	**Lab Formulation (cc)**
Eco-Friendly Base Fluid (cc)	64	0.64	224
E-Z Spot (cc)	8	0.08	28
Water (cc)	28	0.28	98
Total Volume	100		350

Table 3. The formulation of ARC Eco-Spot and commercial spotting fluids

The ARC Eco-Spot shows a much higher reduction in SBM values than spotting fluid A, but a slightly higher value than spotting fluids B and C. As the difference of performance between spotting fluid B and ARC Eco-Spot is marginal, its performance is comparable to the performance of the commercial spotting fluid B. The data clearly indicates that the newly developed ARC Eco-Spot has either a similar or better performance, compared to the two non-eco-friendly non-aqueous based spotting fluids, fluids A or B.

Figure 17 shows the average SBMs of the original mud cake and also the mud cakes soaked for 16 hours in various spotting fluids. A comparison of SBM values determined after 16 hours of soaking time indicates a higher reduction of SBM value for spotting fluid B compared to other spotting fluids. The lowest reduction of SBM for spotting fluid A after 6 hours of soaking time, and the highest reduction of SBM after 16 hours of soaking time indicates that some fluids may need a longer soaking time for effective damage and degradation of the mud cake.

Interestingly, spotting fluid B indicates an increase in SBM value after 16 hours of soaking time compared to the SBM value determined after 6 hours of soaking time. This indicates that spotting fluid B has a time dependent stiffening effect, and therefore, causes an increase in SBM. This indicates that for some spotting fluids, soaking beyond an optimum time period may make it more difficult to recover a stuck pipe. Subsequently, identification of the optimum soaking time of various spotting fluids is very important to recover a stuck pipe easily and quickly. The newly developed ARC Eco-Spot showed no or negligible time dependent stiffening effect, and therefore has a superior long-term behavior compared to spotting fluid B. This fluid causes degradation and weakening of sticking bonds within a short time period (less than 6 hours), and therefore has a superior short-term behavior compared to spotting fluid A. Recovery of a stuck pipe after a short soaking time has high technical and economic benefits.

Figure 18 shows the average USBS of the original mud cake and also the mud cakes soaked for 6 hours in various spotting fluids. The comparison of the average USBS of the original mud cake and the mud cake soaked for 6 hours indicate that all of the spotting fluids reduced the USBS of the mud cake as a result of weakening, damage, and degradation of the sticking bonds, due to the interactions of the spotting fluids with the mud cake. The data further shows that spotting fluid C caused the maximum reduction in USBS after 6 hours of soaking time, and spotting fluid A has the minimum reduction in USBS. The ARC Eco-Spot shows a much higher reduction in USBS values than spotting fluid A, but a slightly lower reduction than spotting fluid B.

Figure 19 shows the average USBS of the original mud cake and also the mud cakes soaked for 16 hours in various spotting fluids. The comparison of USBS values determined after 16 hours of soaking time indicates a slightly higher reduction of USBS value for spotting fluid A, compared to spotting

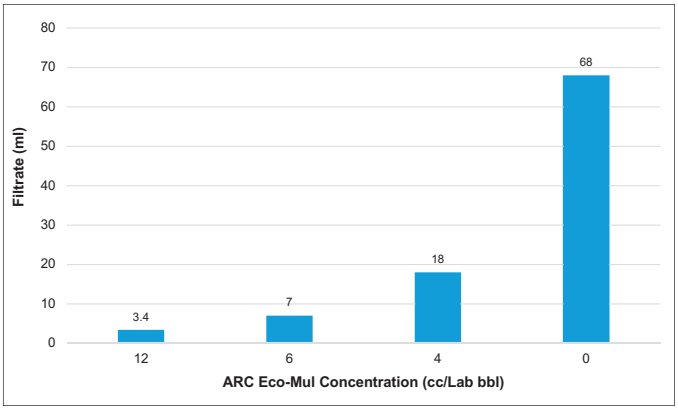

Fig. 16. Experimentally determined SBM of the original and various spotting fluid soaked mud cakes, after 6 hours of soaking time.

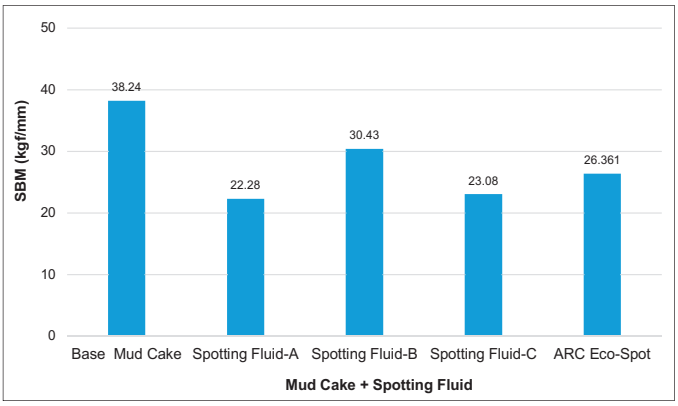

Fig. 17. Experimentally determined SBM of the original and various spotting fluid soaked mud cakes, after 16 hours of soaking time.

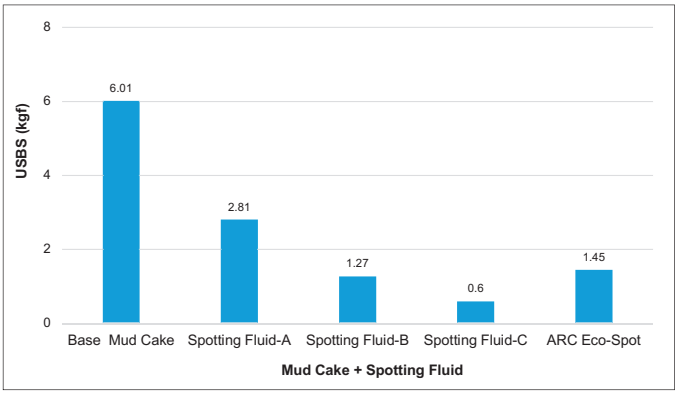

Fig. 18. Experimentally determined USBM of the original and various spotting fluid soaked mud cakes, after 6 hours of soaking time.

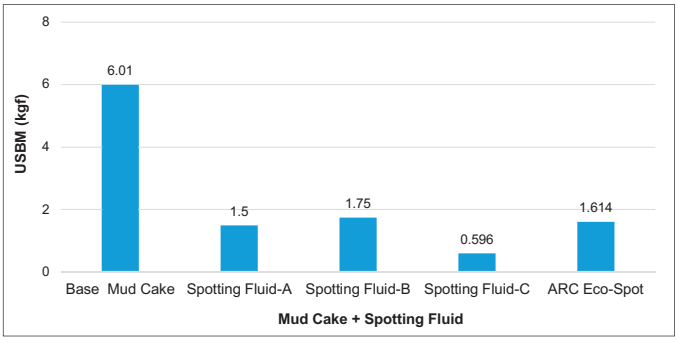

Fig. 19. Experimentally determined USBM of the original and various spotting fluid soaked mud cakes, after 16 hours of soaking time.

fluids B and ARC Eco-Mul. The glycol-based spotting fluid C showed the maximum reduction in USBS. This is consistent with the findings previously described. As before, spotting fluid B indicates an increase in USBS after 16 hours of soaking time, due to the time dependent stiffening effect of this fluid. This highlights again that some spotting fluids can reduce the ease of recovery of a stuck pipe, if soaked beyond an optimum time period due to the time dependent enhancement of the SBM and strength (USBS). Therefore, care should be taken to determine the optimum soaking time to improve the ease of recovery of a stuck pipe. The ARC Eco-Spot fluid has shown negligible time dependent stiffening and hardening effect, and therefore has a superior long-term behavior compared to spotting fluid B.

CONCLUSIONS

1. The huge amount of WVO produced by the food industry locally, regionally, and globally can effectively be used for other industrial applications, if appropriate treatment, processing, upgrading, and formulation are done to fulfill the functional tasks.
2. Refined WVO-based products developed after chemical modification of waste cooking oil has the potential to provide a suite of eco-friendly additives to overcome the current and future environmental challenges faced by the oil and gas industry.
3. Base stocks, emulsifiers and lubricants developed using the waste cooking oil, demonstrated similar or better performance, compared to commercially available equivalent products supplied by various vendors and service companies.
4. The eco-friendly OBM system formulated using the WVO showed better rheological and gel strength properties, compared to a conventional OBM, and therefore, is expected to show better technical performance without any negative impact to the surrounding environment.
5. A comparative evaluation of the ARC Eco-Spot performance in reducing the SBM and USBS, with respect to some commercial spotting fluids used by the industry, indicates that it has the ability to outperform some of the commercial spotting fluids.
6. The green lubricants developed using WVO as the raw material could provide a viable alternative to imported green lubricant products, and therefore can significantly reduce the additive import cost.
7. The renewable nature of WVOs, with the potential to generate a huge volume annually, indicates these oils could be a sustainable source of raw materials for green product development for various industrial applications.
8. The recycling and reusing of WVO for oil and gas field applications will solve the disposal problem of a huge amount of WVO produced by the food and catering industry.
9. The superior fire and flash point characteristics of WVO-based products ensures higher handling, transportation and operating safety, and therefore reduces the likelihood of fire hazards and operational risk.
10. The excellent OHS characteristics of VO-based green products ensures no detrimental impact on the health of workers.

ACKNOWLEDGMENTS

The authors would like to thank the management of Saudi Aramco for their support and permission to publish this article. The authors would also like to acknowledge the support provided by Turki Alsubaie and Ali Radwan for testing and evaluation of the products.

This article was presented at the Annual Technical Symposium and Exhibition, Dammam, Saudi Arabia, April 23-26, 2017.

REFERENCES

1. Daan, R. and Mulder, M.: "Long-Term Effects of OBM Cutting Discharges in the Sandy Erosion Area of the Dutch Continental Shelf," Netherlands Institute for Sea Research Report NIOZ 1994-10, 1994, 26 p.
2. Friedheim, J.E. and Conn, H.L.: "Second Generation Synthetic Fluids in the North Sea: Are They Better?" SPE paper 35061, presented at the SPE/IADC Drilling Conference, New Orleans, Louisiana, March 12-15, 1996.
3. Rae, P., Lullo, G.D. and Ahmad, A.B.: "Toward Environmentally Friendly Additives for Well Completion and Stimulation Operations," SPE paper 68651, presented at the SPE Asia Pacific Oil and Gas Conference and Exhibition, Jakarta, Indonesia, April 17-19, 2001.
4. Amanullah, M.: "Physio-Chemical Characterization of Vegetable Oils and Preliminary Test Results of Vegetable Oil-based Muds," SPE paper 97008, presented at the SPE/IADC Middle East Drilling Technology Conference and Exhibition, Dubai, UAE, September 12-14, 2005.
5. Peresich, R.L., Burrell, B.R. and Prentice, G.M.: "Development and Field Trial of a Biodegradable Invert Emulsion Fluid," SPE paper 21935, presented at the SPE/IADC Drilling Conference, Amsterdam, the Netherlands, March 11-14, 1991.
6. Bland, R.G., Clapper, D.K., Fleming, N.M. and Hood, C.A.: "Biodegradation and Drilling Fluid Chemicals," SPE paper 25754, presented at the SPE/IADC Drilling Conference, Amsterdam, the Netherlands, February 22-25, 1993.
7. Amanullah, M. and Al-Arfaj, M.K.: "Novel Method and Apparatus for Sticking Fluid Performance Evaluation," SPE paper 187982, presented at the SPE Kingdom of Saudi Arabia Annual Technical Symposium and Exhibition,

Dammam, Saudi Arabia, April 24-27, 2017.

8. Chhetri, A.B., Watts, K.C. and Islam, M.R.: "Waste Cooking Oil as an Alternate Feedstock for Biodiesel Production," *Energies*, Vol. 1, Issue 1, June 2008, pp. 3-18.
9. Srivastava, A. and Prasad, R.: "Triglycerides-based Diesel Fuels," *Renewable and Sustainable Energy Reviews*, Vol. 4, Issue 2, June 2000, pp. 111-133.
10. How, H.G., Teoh, Y.H., Masjuki, H.H. and Kalam, M.A.: "Impact of Coconut Oil Blends on Particulate-phase PAHs and Regulated Emissions from a Light-Duty Diesel Engine," *Energy*, Vol. 48, Issue 1, December 2012, pp. 500-509.
11. Sidibé, S.S., Blin, J., Vaitilingom, G. and Azoumah, Y.: "Use of Crude Filtered Vegetable Oil as a Fuel in Diesel Engines State-of-the-Art: Literature Review," *Renewable and Sustainable Energy Reviews*, Vol. 14, Issue 9, December 2010, pp. 2748-2759.
12. Amanullah, M. and Tan, C.P.: "A Field Applicable Laser-based Apparatus for Mud Cake Thickness Measurement," SPE paper 68673, presented at the SPE Asia Pacific Oil and Gas Conference and Exhibition, Jakarta, Indonesia, April 17-19, 2001.
13. Amanullah, M.: "Experimental Determination of Adhesive-Cohesive Bond Strength (ACBS) and Adhesion-Cohesion Modulus (ACM) of Mud Cakes," SPE paper 77198, presented at the IADC/SPE Asia Pacific Drilling Technology Jakarta, Indonesia, September 8-11, 2002.
14. Aadnoy, B.S., Larsen, K. and Berg, P.C.: "Analysis of Stuck Pipe in Deviated Boreholes," SPE paper 56628, presented at the SPE Annual Technical Conference and Exhibition, Houston, Texas, October 3-6, 1999.
15. Hunter, D., Baroid, N.L. and Adams, N.: "Laboratory and Field Data Indicate Water-base Drilling Fluids that Resist Differential Pressure Pipe Sticking," OTC paper 3239, presented at the Offshore Technology Conference, Houston, Texas, May 8-11, 1978.

BIOGRAPHIES

Dr. Md. Amanullah is a Senior Petroleum Engineering Consultant working at Saudi Aramco's Exploration and Petroleum Engineering Center – Advanced Research Center (EXPEC ARC). Prior to joining Saudi Aramco, he worked as a Principal Research Scientist at CSIRO in Australia.

Aman is the lead inventor of a vegetable oil-based dielectric fluid (patented) that led to the formation of a spinoff company in Australia for commercialization of the product.

He has published more than 100 technical papers and filed more than 70 patents, with 18 already granted. Two of Aman's patents were highlighted in scholarly editions of two books published in the U.S.

He is one of the recipients of the 2005 Green Chemistry Challenge Award from the Royal Australian Chemical Institute. Aman also received the CSIRO Performance Cash Reward in 2006, the Saudi Aramco Mentorship Award in 2008 and 2010, the World Oil Certificate Award for nano-based drilling fluid development in 2009, the Intellectual Asset Recognition Award in 2014, and the Award of Recognition for Outstanding Contribution to the success of agricultural waste and environmental protection in 2014. His date tree waste-based product development was highlighted in *The Arabian Sun*, the *Arab News* and also in the *Al Riyadh* newspaper.

Aman is a member of the Society of Petroleum Engineers (SPE). He received the SPE Regional Service Award in 2014 and also the SPE Middle East Drilling Engineering Award in 2016 for his contribution to the industry. Aman also received the Middle East Oil and Gas Technical Innovation of the Year Award in 2017, and in 2018, he received the Board of Engineers Recognition Certificate for Date Seed-based ARC Plug development.

Aman received his M.S. degree (First Class) in Mechanical Engineering from the Moscow Oil and Gas Institute, Moscow, Russia, and his Ph.D. degree in Petroleum Engineering from Imperial College, London, U.K.

Mohammed K. Al-Arfaj joined Saudi Aramco in 2006 as a Petroleum Engineer, working with the Drilling Technology Team in the Exploration and Petroleum Engineering Center – Advanced Research Center (EXPEC ARC). He works in the area of drilling and completion, and has conducted several projects in the areas of shale inhibition, drilling nano-fluids, loss circulation materials, spotting fluids, swellable packers, completion fluids, and oil well cementing.

Mohammed received his B.S. degree in Chemical Engineering from King Fahd University of Petroleum and Minerals (KFUPM), Dhahran, Saudi Arabia, in 2006. In 2009, he received his M.S. degree in Petroleum Engineering from Heriot-Watt University, Edinburgh, Scotland, U.K. In 2017, Mohammed received his Ph.D. degree in Petroleum Engineering specializing in molecular modeling and experimental studies of shale fluid interactions from KFUPM.

Dr. Jothibasu Ramasamy is a Petroleum Scientist working with the Drilling Technology Team of Saudi Aramco's Exploration and Petroleum Engineering Center – Advanced Research Center (EXPEC ARC). He joined Saudi Aramco in July 2013. Prior to this, he worked as a Research Fellow with the Department of Chemistry at the National University of Singapore and as a Postdoctoral Fellow with the Catalysis Center at the King Abdullah University of Science and Technology (KAUST), Saudi Arabia.

Jothibasu received his B.S. degree in Chemistry from Bharathidasan University, Tiruchirappalli, India, and his M.S. degree, also in Chemistry, from Anna University, Chennai, India. In 2010, he received his Ph.D. degree in Chemistry from the National University of Singapore, Singapore.

Jothibasu has published 20 conference papers, 18 journal articles, and filed more than 15 patent applications, with two granted patents received.

Iron Sulfide Deposition in Sour Gas Wells: A Root Cause Analysis

Dr. Tao Chen, Dr. Qiwei Wang, Dr. Fakuen F. Chang, and Amro E. Mukhles

ABSTRACT

Iron sulfide is one of the exotic scales formed in oil and gas fields, particularly for those deep sour gas wells producing from high-pressure, high temperature (HPHT) reservoirs. Compared to the conventional carbonate and sulfate scale, the mitigation of iron sulfide deposition is notoriously difficult.

To develop a suitable mitigation strategy, it is essential to understand the formation mechanisms of iron sulfide in the given production system. In this work, we combined laboratory tests, thermodynamic modeling, and field monitoring to understand the source of iron, and the mechanisms of iron sulfide deposition in sour gas wells during acidizing treatment and the production stage.

The study results indicate that iron sulfide deposition in sour gas wells is a corrosion-induced scaling problem. During acidizing treatment, a high concentration of iron is released from the tubular due to acid attack, despite a corrosion inhibitor being used in the stimulation fluid package. Large amounts of iron sulfide can precipitate when spent acid mixes and reacts with hydrogen sulfide (H_2S) in the reservoir, and potentially causes severe formation damage. During the production stage, the iron released from the tubular due to corrosion in the produced water under HPHT, is the major contribution of iron sulfide deposited at the surface of the tubing. These iron sulfide deposits, although appearing as a porous layer, can protect the downhole completion from the highly corrosive fluids, which leads to the unexpected long service lives of the mild carbon steel tubulars in many wells. Accelerated corrosion can occur when the protective iron sulfide film or deposit is disturbed, or if there is only a partial coverage.

This article presents a fundamental study to understand the root cause of iron sulfide deposition in sour gas wells. The study results demonstrate that effective corrosion inhibition is key to mitigate the iron sulfide deposition problem in the sour gas wells.

INTRODUCTION

Iron sulfide deposition is an exotic scale deposited during oil and gas production, especially for deep sour gas wells producing from high-pressure, high temperature (HPHT) reservoirs. It can cause flow assurance problems, such as restriction of downhole surveillance and intervention.

Over the past few decades, great efforts have been made to understand the conventional oil field scale formation and inhibition, such as calcium carbonate, barium sulfate, and calcium sulfate. Compared to these conventional mineral scale deposits, iron sulfide as an exotic scale has received less attention for a few reasons. First, some iron sulfide crystals often form a softer scale than calcium carbonate. This scale may not always block tubing to the same degree that other mineral scales do. Therefore, it may be seen as less of a problem than other mineral scales[1]. The second problem associated with iron sulfide is that it is much more difficult to study in the laboratory than other common mineral scales — keeping the system oxygen-free — and the reproducibility of the iron sulfide tests are two major challenges[2]. Third, iron sulfide is present in several crystalline forms that have different sulfur to iron ratios, which makes the research complex[3]. These challenges have limited the progress of research on iron sulfide scale formation and inhibition in the past.

Compared to the conventional carbonate and sulfate scale, the mitigation of iron sulfide deposition is notoriously difficult. Both chemical and mechanical methods have been used to remove downhole iron sulfide scale[4-6]. Hydrochloric (HCl) acid based scale dissolvers were applied to chemically remove the deposits. Heavy corrosion to the production string, the casing, and the generation of hydrogen sulfide (H_2S) during descaling jobs are major concerns and barriers to the application of this type of scale dissolver in these sour gas wells. Mechanical descaling can remove iron sulfide deposited in the tubings, but it is costly and time-consuming. In addition, mechanical descaling cannot approach and remove the scale deposited in the near wellbore region[7].

In recent years, extensive efforts have been devoted to understanding the iron sulfide scale formation mechanisms and to identify effective scale management strategies for the high temperature sour gas wells. Our previous study concluded that tubing corrosion is one of the major sources of iron for iron sulfide surface deposition in downhole tubulars during production[8].

This article presents a fundamental study to further understand the mechanisms of iron sulfide surface deposition in

sour gas wells during both the production stage and acidizing treatment by combining scale modeling and laboratory tests. Such efforts will contribute to understanding the mechanisms of iron sulfide formation and developing a suitable strategy to manage the iron sulfide deposition in the downhole tubulars and near the wellbore matrix.

EXPERIMENTAL PROCEDURE

Iron Sulfide Deposition during Acid Stimulation

The iron sulfide scale prediction during acid stimulation in this study is based on a bullhead matrix acidizing treatment conducted in a sour gas well. There were three major stages of fluid injection during the acidizing treatment, including injection of organic solvent, HCl acid, and treated water. This study focuses on acid injection to prevent potential iron sulfide scale deposits. In this treatment, 972 bbl of inhibited HCl acid — 26 wt% — was injected in the reservoir through a 4½" diameter 1,300 ft long tubing made of API T-95 carbon steel. The pumping rate of HCl acid was six barrels per minute (bpm) to 16 bpm, and the contact time for the tubing and acid was 16 to 43 minutes.

Corrosion coupon tests were conducted to collect data of the corrosion rate and iron released from the tubing during the acid injection stage of the acidizing treatment. T-95 test coupons with an area of 38.96 cm^2 were polished and preweighed prior to soaking in 30 ml of corrosion inhibited 26 wt% HCl acid. The tests were performed at 125 °C. After half an hour, the coupons were pulled out and washed, and then dried for final weighing. The iron released from the tubing during acid injection was calculated.

The ScaleSoftPitzer prediction model[9] was used to simulate the iron sulfide deposition in the sour gas wells during acid stimulation. The model is designed to calculate thermodynamic equilibrium states for 11 different minerals, including iron sulfide, and is based upon the Pitzer theory of electrolytes.

The scale prediction calculations provide values for the saturation ratio (SR) or saturation index (SI), where SI = $\log_{10}$SR, parameters indicating the thermodynamic driving force for the formation of each scale type and the possible mass of scale precipitate. The software — and other similar scale prediction codes — calculate the supersaturation ratio using either the ion pairing or the Pitzer equation. It can be used to provide a guide to the likely nature and extent of the scaling challenge and to investigate the impact of a process change on the likely severity of scaling. It is also the case that different programs may interpret the level of risks slightly different.

The formula for the SR is given in Eqn. 1:

$$SR = (a_1 \times a_2)/K_{(PT)} \quad (1)$$

where $a = \gamma \times C$. Here, a_1 and a_2 are the activity of scaling cation and anion in the solution, respectively. K is normally called the solubility product, which depends on pressure, P, and temperature, T. C is the concentration of the ions in the solution, and γ is the ionic activity coefficient.

SR	Interpretation
< 1	Undersaturated for this scale type. No scale risk.
= 1	Equilibrium condition. Scale formation rate is equal to scale dissolution rate. No scale will form.
> 1	Moderately to highly supersaturated. Scaling is likely.

Table 1. Interpretation of scale prediction results

Scale can occur at any point in the oil and gas production system where supersaturation is generated. A supersaturated solution is the primary cause of scale formation. The degree of supersaturation is the driving force for the precipitation reaction and implies the possibilities for scale precipitation.

In terms of thermodynamics, three possibilities exist in terms of scale formation from the solution, Table 1. (1) SR < 1: The solution is under saturated and scale formation is not thermodynamically feasible. (2) SR = 1: The solution is saturated. The scale formation and dissolution rate in the solution is the same and no scale is formed in the solution. (3) SR > 1: The solution is supersaturated and scale formation is thermodynamically possible[10].

In this study, the thermodynamic scale prediction model was carried out with the input of acid, spent acid and a typical formation water chemistry, reservoir conditions, and production rates of a sour gas well. Table 2 lists the typical formation water chemistries, gas analysis (%), gas-water production rates, and the reservoir pressure and temperature.

Formation Water Chemistry (mg/L)	
Na^+	62,700
K^+	4,000
Ca^{2+}	22,000
Mg^{2+}	1,180
Cl^-	139,000
SO_4^{2-}	25
HCO_3^-	1,512
Gas Analysis (%)	
CO_2	4.0
H_2S	5.0
Production Rate	
Gas	20 MMscf/d
Water	60 bbl/d
Reservoir Conditions	
Temperature (°C)	125
Pressure (psi)	4,600

Table 2. The typical formation water chemistries, gas analysis (%), gas-water production rates, and the reservoir pressure and temperature applied in scale prediction

Iron Sulfide Deposition during Production

A newly developed downhole corrosion and scale monitoring (DCSM) tool has been designed and developed for measuring corrosion and scale formation in oil and gas wells[11]. This monitoring system represents significant improvements over the current industrial technology by directly measuring corrosion and scale deposition in real downhole conditions using coupons of identical metallurgy as the production tubing, which the commercial tools failed to achieve. The concept of the development has been approved from the lab design, and from manufacture to field application. Field application had been carried out in a sour gas well with similar operating conditions previously shown in Table 2. A slick line conveyed through-tubing, retrievable high expansion gauge hanger is used to deploy and anchor the DCSM downhole at the desired depth of 12,320 ft. The test coupon ring is made of T-95 carbon steel, the same material as the downhole tubing, and is retrieved after 3 months for post-analysis.

A series of advanced post-analyses were performed to understand the corrosion and scaling of the applied coupons, including weight changes for mass of scale and corrosion measurement. A scanning electron microscope (SEM) was used for the morphologies of iron sulfide surface deposition, and X-ray diffraction (XRD) was used for the composition of surface deposition.

RESULTS AND DISCUSSION

Iron Sulfide Deposition during Acid Stimulation

This part of the study focused on several stages during acid injection, including iron being released from the tubing due to corrosion byproduct, reservoir carbonate dissolution by acid, and scale formation when spent acid mixes with formation water saturated with sour gases.

Iron Released from Tubing during Acid Injection — Corrosion Coupon Tests

Corrosion coupon tests were carried out to evaluate the corrosion rate of corrosion inhibited 26 wt% HCl acid during the acid injection stage. The reaction of a carbon steel coupon is shown in Eqn. 2.

$$Fe + 2\ HCl \rightarrow FeCl_2 + H_2 \quad (2)$$

The test coupon was immersed in corrosion inhibited 26 wt% HCl acid over half an hour at 125 °C. The surface area of the test coupon is 38.96 cm^2. A coupon weight loss of 1.6645 g was measured after a test duration of half an hour. The calculated corrosion rate is 4.334 mm/y, and the iron released in the 30 ml corrosion inhibited 26 wt% HCl acid due to corrosion was 60,058 mg/l. It should be noted that the corrosion test lasts half an hour in this study; while a longer contact time during acid injection will cause even harsher corrosion and a higher iron concentration in the acid solution.

The matrix acidizing treatment is to pump acid into the formation below the fracturing pressure to stimulate production. Acid stimulation in a carbonate reservoir is to allow the acid to dissolve carbonate and create wormholes or flow channels in the near wellbore region[6].

The reaction of a calcium carbonate reservoir and acid is shown in Eqn. 3.

$$CaCO_3 + 2HCl \rightarrow CaCl_2 + CO_2 + H_2O \quad (3)$$

During the HCl acid injection stage, some of the HCl acid was consumed due to tubing corrosion, as previously shown in Eqn. 2. Approximately 18 wt% of active HCl acid was left when the acid approached the carbonate formation in the near wellbore region. The Ca^{2+} ions released into the spent acid fluid and the pH of the spent acid increased due to the consuming of active HCl acid during carbonate dissolution. The concentration of Ca^{2+} ions released into spent acid fluid had an inverse proportion with the active HCl acid left in the spent acid. The calculated Ca^{2+} ions' concentration was up to 99,567 mg/l when all active HCl acid was spent, where the pH of the spent acid is 3.89 according to scale prediction with the ScaleSoftPitzer model. When the spent acid was saturated with sour gas, the predicted pH decreased to 3.75.

A scenario of scale deposition during acid stimulation is the mixing of spent acid with formation water saturated with sour gases. The spent acid contains a high concentration of iron due to tubing corrosion during acid injection. When it mixes with formation water containing saturated sour gases and bicarbonate ions, iron sulfide could precipitate and may become a serious problem.

Scale prediction modeling was performed to assess the scaling tendency when the spent acid mixes with formation water saturated with sour gases. The spent acid contained 60,058 ppm of iron and 99,567 ppm of calcium. Figure 1 shows the pH of the mixed spent acid and formation water saturated

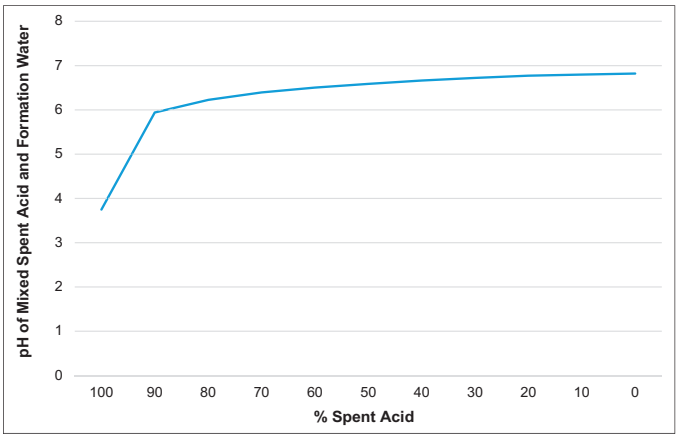

Fig. 1. The pH of mixing spent acid and formation water saturated with sour gases.

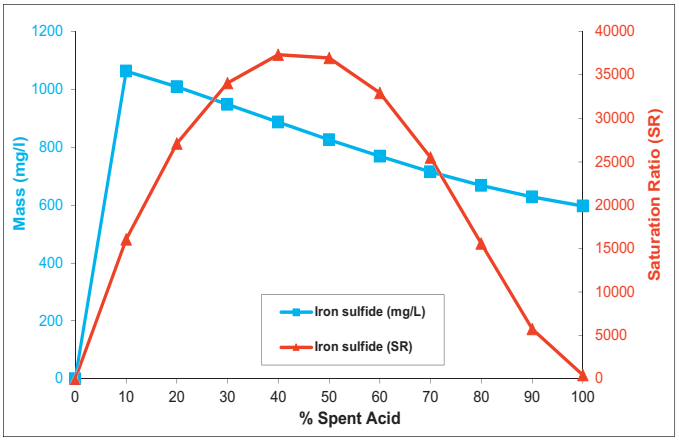

Fig. 2. Iron sulfide scale prediction when spent acid mixes with formation water saturated with sour gases under reservoir conditions.

with sour gases under reservoir conditions.

The pH of 100% spent acid saturated with sour gases is 3.75. When it mixes with formation water saturated with sour gases, the pH increases. At the ratio of 10:90 mixing of spent acid and formation water saturated with sour gases, the pH increases to ~5.94. The pH increases with a further increase in the ratio of formation water until it reaches a pH of 6.82 in 100% formation water. A higher pH favors precipitation of certain scales, e.g., calcium carbonate, iron sulfide, and iron carbonate.

Iron sulfide scale was predicted to form when spent acid mixes with formation water saturated with sour gases under reservoir conditions, Fig. 2.

An extremely high iron sulfide SR was predicted. The worst-case of iron sulfide precipitate was predicted with a SR over 37,000 at a 40:60 mixing ratio of spent acid and formation water. The highest precipitation mass of 1,063 mg/l was estimated in the 10% spent acid and 90% formation water mixture. Iron sulfide scale deposition is certain to occur, and severe iron sulfide scaling is expected with potential formation damage problems and associated scaling problems in the production tubing and equipment.

In a real acidizing treatment, corrosion inhibitor is always added in the acid package to inhibit tubing corrosion. The corrosion inhibitor can reduce the iron release from carbon steel tubing due to corrosion, and mitigate the iron sulfide scale problem, to a certain level. It is still an industrial challenge to develop a corrosion inhibitor to effectively inhibit corrosion of 26 wt% HCl acid on carbon steel at an elevated temperature above 100 °C[12]. Effective iron sulfide scale prevention and mitigation treatments will still be required to inhibit scale deposition and prevent flow restrictions in the near wellbore region and downhole tubular during acidizing treatment in a carbonate reservoir.

Iron Sulfide Deposition during Production

A T-95 test coupon was deployed with DCSM at a desired depth of 12,320 ft in a sour gas well with similar operation conditions previously shown in Table 2. The coupon was retrieved after 3 months for post-analysis.

	Weight Before (g)	Weight After (g)	Weight Change (g)
T-95 Coupon	117.821	117.880	0.049

Table 3. Weight change of the T-95 coupons before and after field application

Table 3 shows the overall weight change of the T-95 coupons before and after field application. The weight change is composed of the weight loss due to corrosion — reducing weight — and the weight gain due to the formation of scale on the coupon surface — increasing weight. A minor weight increase of 0.049 g was measured for the T-95 coupon after field application.

Figure 3a is a photograph of the T-95 carbon steel coupon before field application, and Fig. 3b is a photograph of the same coupon and after being retrieved from 3 months of exposure in the field. Before field application, the coupon surface was mechanically polished without any deposition or corrosion. A thin layer of black deposition was observed on the surface of the test T-95 coupon after field application. Based on visual observation, there was a certain amount of corrosion byproduct or scale deposited on the surface of the coupon during the 3 months of field application.

Figure 4 is the optical image of the surface of the T-95 carbon steel coupon; before field application, Fig. 4a, and retrieved after from 3 months of exposure in the field, Fig. 4b. No

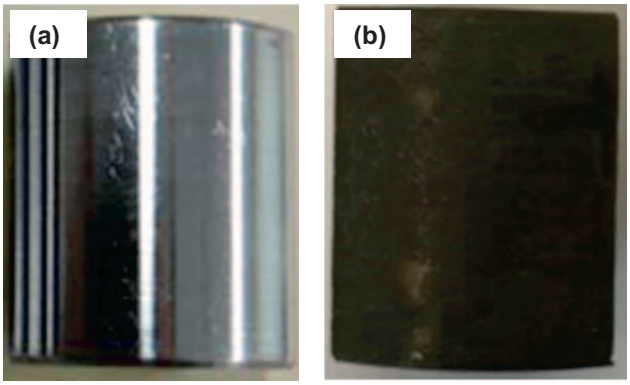

Fig. 3. Photographs of the T-95 coupon: (a) before field application, and (b) retrieved after 3 months from the field.

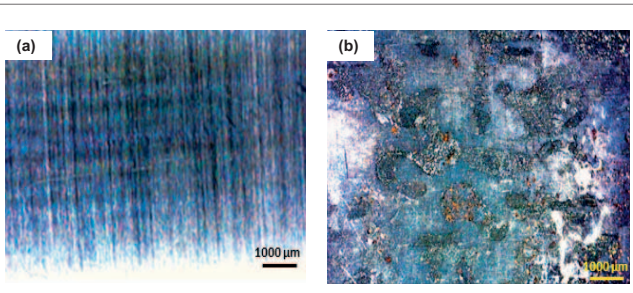

Fig. 4. Optical images of the T-95 coupon: (a) before field application, and (b) retrieved after 3 months from the field.

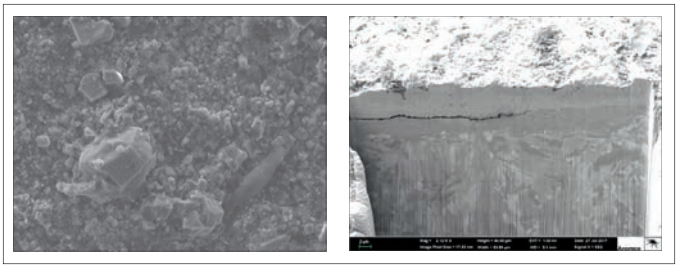

Fig. 5. The SEM morphology of the T-95 coupon after field application.

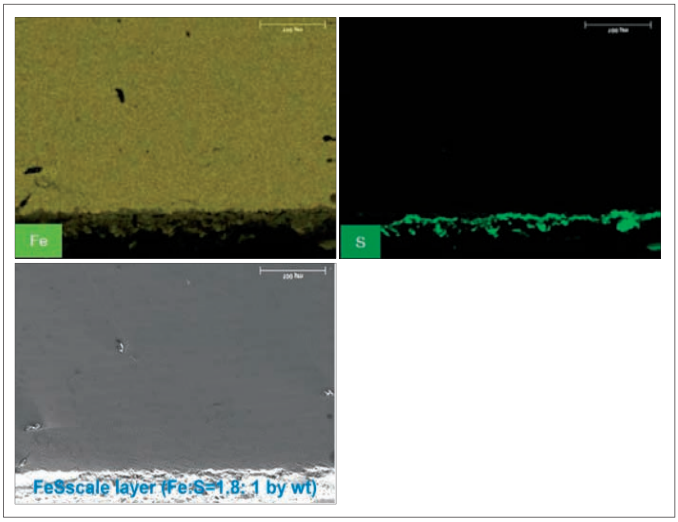

Fig. 6. The EDS cross-section of the T-95 coupon after field application.

obvious features besides the machining lines were observed on the surface before field application, while patched areas with a size of around a few hundred microns were observed from the surface coupon after being retrieved from the field.

High resolution SEM images and energy dispersive X-ray spectrometer (EDS) of the surface deposition and cross-section of the T-95 coupon after field application are shown in Fig. 5 and Fig. 6, respectively. Figure 5 shows a dense layer of deposit formed on the coupon surface after field application. The thickness of the surface deposit is about 3 µm to 4 µm. Figure 6 shows this surface deposit is mainly composed of iron and sulfur, and the ratio is 1.8:1 by weight.

The crystallization of the surface deposition was analyzed by XRD. The result is shown in Fig. 7. The surface deposition is composed of 66% pyrrhotite, 24% pyrite, and 9% marcasite.

The iron released from the tubing reacted with sulfide and formed an iron sulfide surface deposition. This thin black iron sulfide film deposited on the surface of a test coupon and caused a slight weight increase, as previously shown in Table 3. It worked as a protective film and reduced further corrosion on the test coupon. This observation agrees with the findings from other studies, where iron sulfide films formed on carbon steel during sour oil and gas production, and can be very protective against further corrosion for long periods of time[6, 13].

Over the past decade, great efforts have been made to

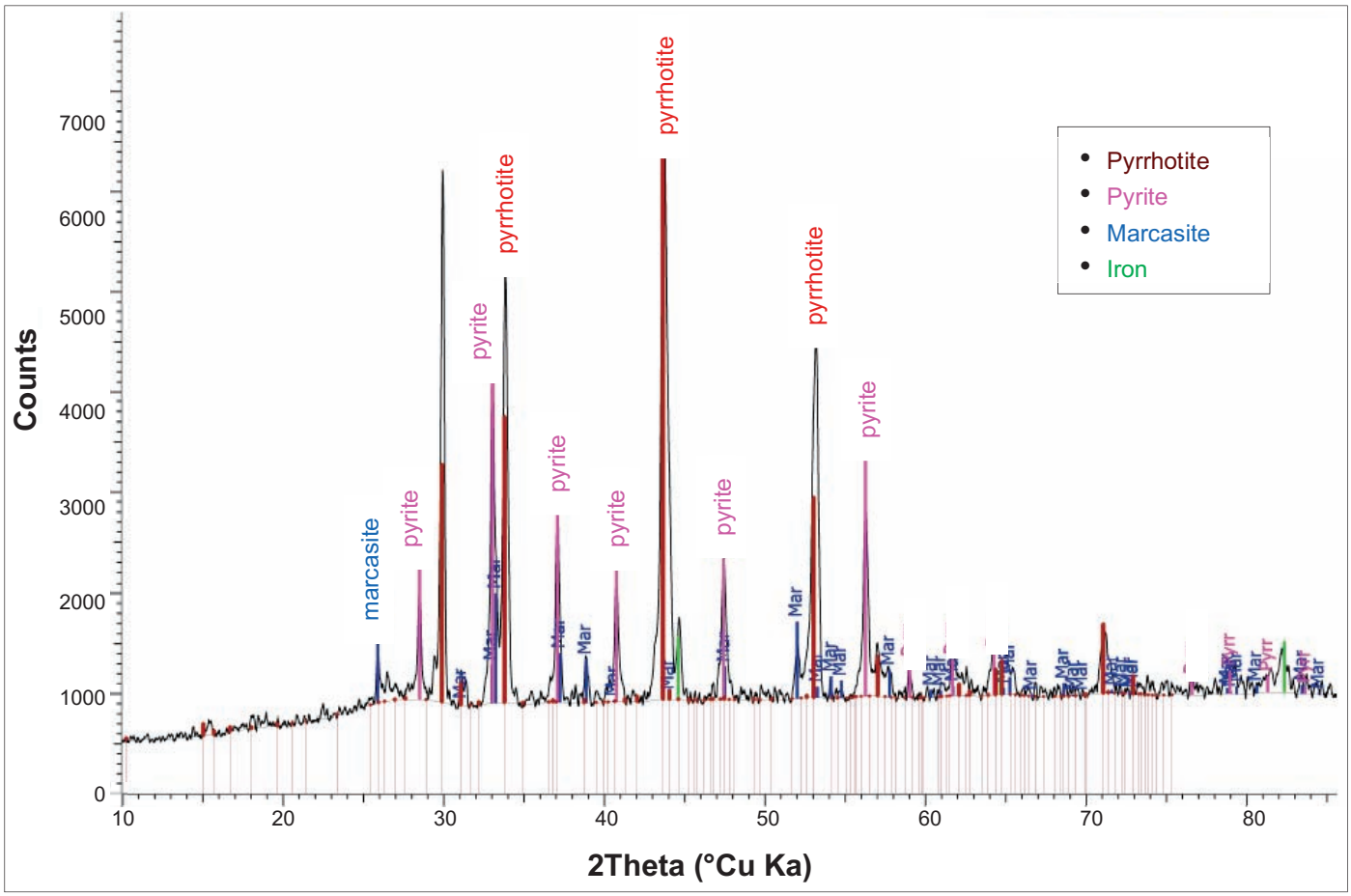

Fig. 7. XRD composition analysis of the T-95 coupon surface deposition after field application.

understand the mechanisms of iron sulfide scale deposited in sour wells. There are a few sources of iron for iron sulfide reported in previous studies. One of the iron sources is tubular corrosion during production[8]. Another source of iron could be from the formation water due to dissolution of iron sulfide from the original mineral species in the formation[8]. In addition, the iron could be introduced during drilling, completion, and stimulation operations, where the leaking of operation fluids containing iron can contaminate the produced water and bring iron into the produced water[14, 15]. This contamination theory does not support iron sulfide deposition over the long term.

In this study, the source of iron for iron sulfide deposited in sour gas wells has been studied during production and acid stimulation.

In combined reservoir scale prediction modeling and lab corrosion tests, the iron released in the acid during acid stimulation could be ~60,000 mg/L under the test conditions in the presence of a corrosion inhibitor. Due to the limited inhibition efficiency of the corrosion inhibitor on 26 wt% HCl acid at high temperatures, a large amount of iron still could be released during acid stimulation, even with a corrosion inhibitor applied. It could cause severe formation damage in the near wellbore region, and scale deposition on the downhole tubing and surface flow lines.

According to the DCSM monitoring under real downhole conditions during production, the iron released from the tubing due to corrosion in produced water is a source of iron sulfide deposition in the downhole tubular. Iron sulfide surface deposition during the production stage is a corrosion-induced scale issue.

CONCLUSIONS

1. In combination with the post-laboratory analysis on retrieved coupons, DCSM can provide corrosion and scale mechanism for specific metallurgy in sour gas wells during production. The iron released from the tubing due to corrosion during the production stage is a source of iron sulfide deposition in the tubular and surface facilities. The iron released from the tubing reacted with sulfide, and formed iron sulfide surface deposition.

   Iron sulfide surface deposition during the production stage is a corrosion-induced scale issue. A thin layer of iron sulfide was deposited on the surface of a DCSM coupon over 3 months of field exposure. The scale deposition worked as a protective layer to reduce the further interactions between the metal coupon and the produced gas-fluid media. In this way, further corrosion of the test T-95 coupon could be reduced. The thickness of the surface deposition is ~3 μm to 4 μm. The rate of iron sulfide deposition is far less than the field observation. Other sources of iron sulfide scale deposition should be further investigated in sour gas wells.

2. Iron sulfide formation during acid stimulation is another source of iron deposition in sour gas wells. The iron sulfide could deposit in both the near wellbore region and downhole tubing during acid stimulation in sour gas wells. It could cause formation damage in the near wellbore region and contribute to downhole tubing blockage.

ACKNOWLEDGMENTS

The authors would like to thank the management of Saudi Aramco for their support and permission to publish this article. The authors would also like to thank Esmael Albelharith for field application support, and Feng Liang for the post-analysis.

This article was presented at the SPE International Oil Field Corrosion Conference and Exhibition, Aberdeen, Scotland, U.K., June 18-19, 2018.

REFERENCES

1. Przybylinski, J.L.: "Ferrous Sulfide Solid Formation and Inhibition at Oxidation Reduction Potentials and Scaling Indices like Those That Occur in the Oil Field," SPE paper 80260, presented at the International Symposium on Oil Field Chemistry, Houston, Texas, February 5-7, 2003.
2. Chen, T., Montgomerie, H., Chen, P., Hagen, T.H., et al.: "Development of Environmental Friendly Iron Sulfide Inhibitors for Field Application," SPE paper 121456, presented at the SPE International Symposium on Oil Field Chemistry, The Woodlands, Texas, April 20-22, 2009.
3. Nasr-El-Din, H.A. and Al-Humaidan, A.Y.: "Iron Sulfide Scale: Formation, Removal and Prevention," SPE paper 68315, presented at the International Symposium on Oil Field Scale, Aberdeen, Scotland, U.K., January 30-31, 2001.
4. Leal Jauregui, J.A., Solares, J.R., Nasr-El-Din, H.A., Franco, C.A., et al.: "A Systematic Approach to Remove Iron Sulfide Scale: A Case History," SPE paper 105607, presented at the SPE Middle East Oil and Gas Show and Conference, Manama, Kingdom of Bahrain, March 11-14, 2007.
5. Leal Jauregui, J.A., Garcia, W.N., Al-Ismail, S.A., Solares, J.R., et al.: "Novel Mechanical Scale Clean-out Approach to Remove Iron Sulfide Scale from Tubulars in Vertical High-Pressure and Temperature Deep Gas Producers: A Case History," SPE paper 121404, presented at the EUROPEC/EAGE Conference and Exhibition, Amsterdam, the Netherlands, June 8-11, 2009.
6. Hamby Jr., T.W.: "Development of High-Pressure Sour Gas Technology," *Journal of Petroleum Technology*, Vol. 33, Issue 5, May 1981, pp. 792-798.
7. Chen, T., Wang, Q., Chang, F.F. and Albelharith, E.: "Multifunctional and Nonacidic Iron Sulfide Scale

Dissolver for Downhole Applications," SPE paper 188924, presented at the Abu Dhabi International Petroleum Exhibition and Conference, Abu Dhabi, UAE, November 13-16, 2017.

8. Chen, T., Wang, Q. and Chang, F.F.: "Understanding the Mechanisms of Iron Sulfide Formation in Sour Gas Wells," NACE paper 16-8211, presented at the 16th Middle East Corrosion Conference and Exhibition, Manama, Kingdom of Bahrain, February 8-11, 2016.
9. Kan, A.T. and Tomson, M.B.: "Scale Prediction for Oil and Gas Production," SPE paper 132237, presented at the International Oil and Gas Conference and Exhibition, Beijing, China, June 8-10, 2010.
10. Xu, B., Chen, T., Chen, P., Montgomerie, H., et al.: "Influence of Calcium and Bicarbonate Ions on the Kinetics of $CaCO_3$ Formation at High Temperature in the Absence and Presence of Scale Inhibitors," SPE paper 169769, presented at the SPE International Oil Field Scale Conference and Exhibition, Aberdeen, Scotland, U.K., May 14-15, 2014.
11. Chen, T., Chang, F.F., Liang, F. and Mukhles, A.: "Corrosion and Scaling Monitoring under Real Downhole Conditions in Sour Gas Wells," SPE paper 192231, presented at the SPE Kingdom of Saudi Arabia Annual Technical Symposium and Exhibition, Dammam, Saudi Arabia, April 23-26, 2018.
12. Rae, P. and Di Lullo, G.: "Matrix Acid Stimulation — A Review of the State-of-the-Art," SPE paper 82260, presented at the SPE European Formation Damage Conference, The Hague, the Netherlands, May 13-14, 2003.
13. Bich, N.N. and Goerz, K.: "Caroline Pipeline Failure: Findings on Corrosion Mechanisms in Wet Sour Gas Systems Containing Significant CO_2," paper presented at the NACE International/CORROSION 1996 Conference and Exhibition, Denver, Colorado, March 24-29, 1996.
14. Al-Tammar, J.I., Bonis, M., Choi, H.J. and Al-Salim, Y.: "Saudi Aramco Downhole Corrosion/Scaling Operational Experience and Challenges in HP/HT Gas Condensate Producers," SPE paper 169618, presented at the SPE International Oil Field Corrosion Conference and Exhibition, Aberdeen, Scotland, U.K., May 12-13, 2014.
15. Wang, Q., Ajwad, H., Shafai, T. and Lynn, J.D.: "Iron Sulfide Scale Dissolvers: How Effective Are They?" SPE paper 168063, presented at the SPE Saudi Arabia Section Technical Symposium and Exhibition, al-Khobar, Saudi Arabia, May 19-22, 2013.

BIOGRAPHIES

Dr. Tao Chen is a Petroleum Engineering Specialist working with the Production Technology Team of Saudi Aramco's Exploration and Petroleum Engineering Center – Advanced Research Center (EXPEC ARC). His interests are production chemistry and flow assurance in the oil and gas industry, specializing in oil field scale management.

Prior to joining Saudi Aramco in 2014, Tao spent more than 15 years on oil field scale management and worked at Clariant, Champion Technologies, Nalco Champion, and LR Senergy in Aberdeen, U.K.

He has published nearly 70 technical publications about scale management in oil fields.

Tao received both his B.S. and M.S. degrees in Chemical Engineering from Dalian University of Technology, China, and his Ph.D. degree in Chemical Engineering from Heriot-Watt University, Edinburgh, U.K. Tao also received an MBA from Warwick University, Coventry, U.K.

Dr. Qiwei Wang works in Saudi Aramco's Research & Development Center as a Science Specialist in oil field scale mitigation. Since joining Saudi Aramco in 2011, he has played a key role in all major scale mitigation activities and led the completion of over 40 projects. Before joining Saudi Aramco, Qiwei worked for Nalco Champion as a R&D Coordinator on flow management and as a Senior Specialist on scale management. He has over 25 years of R&D and technical support experience in oil field production chemistry, scale management, and water treatment.

Qiwei is an active member of the Society of Petroleum Engineers (SPE) and National Association of Corrosion Engineers (NACE). He has organized workshops, served on technical committees, and has chaired several conferences for both organizations.

He has authored and coauthored over 130 publications and 12 U.S. patent applications.

Qiwei received his B.Eng. degree in Chemical Engineering from Taiyuan University of Science and Technology, Taiyuan, China; an M.Eng. degree in Material Sciences from Harbin Institute of Technology, Harbin, China; an M.S. degree in Chemistry from the University of Ryukyus, Okinawa, Japan; and a Ph.D. degree in Oceanography from Texas A&M University, College Station, TX.

Dr. Fakuen "Frank" F. Chang is the focus area champion for Productivity Enhancement in the Production Technology Team of Saudi Aramco's Exploration and Petroleum Engineering Center – Advanced Research Center (EXPEC ARC).

Prior to joining Saudi Aramco in September 2012, he worked at Schlumberger for 16 years. Before that, Frank was at Stimlab for 4 years. He has developed many products and technologies dealing with sand control, fracturing, acidizing and perforating.

Frank is an inventor and recipient of 23 granted U.S. patents, and he is the author of more than 40 Society of Petroleum Engineers (SPE) technical papers.

Frank received his B.S. degree in Mineral and Petroleum Engineering from the National Cheng Kung University, Tainan City, Taiwan; his M.S. degree in Petroleum Engineering from the University of Louisiana at Lafayette, Lafayette, LA; and his Ph.D. degree in Petroleum Engineering from the University of Oklahoma, Norman, OK.

Amro E. Mukhles is a Petroleum Engineer supervisor in Saudi Aramco's Southern Ghawar Production Engineering Department. He has 12 years of experience in the oil and gas industry in areas like production optimization, well completion, stimulation, well intervention operations as well as scale and corrosion mitigation.

Amro received his B.S. degree in Petroleum Engineering from West Virginia University, Morgantown, WV, and his M.S. degree in Petroleum Engineering from the University of Texas at Austin, Austin, TX.

Lessons Learned from "In-well" Fiber Optic DAS/DTS Deployment

Modiu L. Sanni, Frode Hveding, Dr. Sunil L. Kokal, and Ibrahim M. El-Zefzafy

ABSTRACT

Fiber optic sensing technology has gradually become one of the pervasive tools in the monitoring and surveillance toolkit for reservoir and production engineers. Traditionally, sensing with fiber optic technology in the form of distributed acoustic sensing (DAS) or distributed temperature sensing (DTS), and most recently, distributed strain sensing and distributed chemical sensing, were done with the fiber being permanently clamped either behind the casing or production tubing. Clamping the fiber behind the tubing or casing is sometimes beleaguered with operational challenges that often lead to rendering the fiber partially damaged or inoperable. The emergence of the composite carbon rod system that can be easily deployed in and out of a well, similar to wireline logging, has made it possible to sense any well without prior fiber optic installation.

In this article, we present the lessons learned from the first well where we deployed in-well fiber optic DAS/DTS. The use of DAS/DTS was done in a few vertical oil producer wells and water injector wells without prior fiber optic installation. The key objectives of the tests were to: (1) investigate the well integrity across the entire length of each well, (2) assess the production and injection flow profile across the perforations and behind casing, which to now, was not possible with a conventional production logging tool (PLT), and (3) investigate the possibility of using the combination of a distributed acoustic survey and a distributed temperature survey for quantitative production flow analysis.

This article reviews the complete design and implementation of the in-well fiber optic deployment, field operational issues, analyses, and interpretation of the sensing results. The combination of DAS/DTS data showed no well integrity related issues. The sensing data surprisingly pinpointed a few geological features such as cooling shallow aquifers that until now had not been noticed. The combination of different pulse widths during shut-in and the production and injection cycles helped to refine the resolution of the flow profile from the production and injection zones.

INTRODUCTION

Innovative wellbore monitoring using fiber optic distributed acoustic sensing (DAS) and distributed temperature sensing (DTS) improves the information available for reliable decision making for effective reservoir management. Downhole data acquisition by fiber optic sensing enables the user to obtain information across the entire reservoir simultaneously. Another level of information beyond the traditional wireline conveyed production logging tool (PLT) techniques is captured because of the nature of fiber optic sensing. The user can observe in real-time the dynamic environment across the entire sensing area during production or injection changes and can act accordingly.

There are three main methods for getting fiber optics down into the wellbore, exposed to the variations in temperature and noise, i.e., production or injection[1]. These methods are permanent installations, semi-permanent installations and intervention-based service.

Permanent installation is obtained by strapping a fiber optic line outside the casing and cementing it in place, Fig. 1a. Fiber can then be used to observe the heat being generated during curing and so give indications of the height of cement, and also the potential quality. In addition, since the fiber is directly coupled to the sandface, it will be able to provide good information

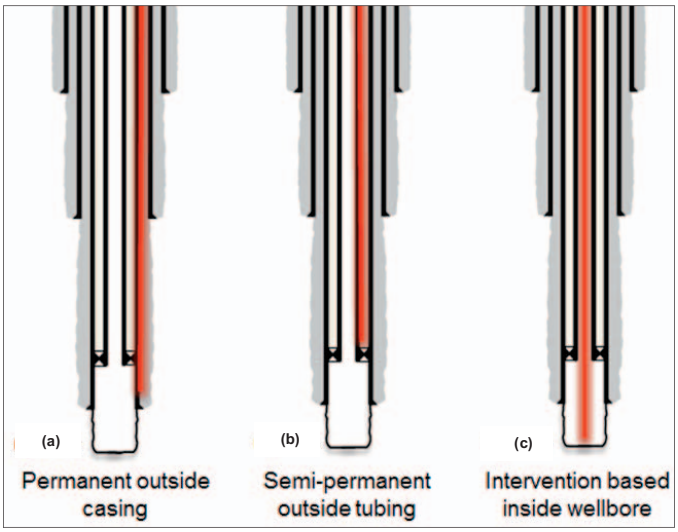

Fig. 1. Different fiber optic installation methods.

about production related effects if it is placed across the reservoir. Other applications like vertical seismic profiling (VSP) and geological subsidence can also be detected with the right combination of a laser box and fiber optic cable.

In a semi-permanent installation, the fiber optic cable is strapped outside a tubing and is exposed to the annulus between the tubing and the casing, Fig. 1b. If the tubing is pulled out, the fiber will also be removed. Normally, this installation limits the fiber optics to be in the upper completion only, above the production packer.

The complexity of also including fiber optics in the lower completion is high and not much utilized, although it is possible. Many applications for the various installations are the same, but this installation can be particularly useful for leak detection between the tubing and annulus. In populated areas, and with groundwater protection in mind, it is very useful to obtain integrity information in real-time without having to open and enter a wellbore.

Both of these described methods require a higher capital cost and lower operational cost. The main advantage with the above methods is that the user is able to acquire instant downhole logging without accessing the wellbore, simply by attaching either a DAS laser box or a DTS laser box, or both, to the fiber optic cable(s) easily available at the surface.

The third method is running fiber optics downhole ("in-well") as an intervention-based service. This method can be very useful in cases where the well does not initially include a fiber optic installation, like an open hole completion for instance, Fig. 1c. The ability to position the fiber optic cable across the entire reservoir increases the value of this method. In addition to the applications enumerated for the permanent and semi-permanent installations, the flexibility enables the user to obtain information like production flow allocation, injection flow allocation, cross-flow determination, flow behind casing, and many more[2, 3]. Having the fiber optic cable inside the fluid flow in the tubing itself captures the fluid dynamics in a very good way. A fiber optic cable can be run into the wellbore in several ways. There are three main intervention-based methods:

1. Fiber optic embedded in a coil tubing (CT). In this case, the fiber optic cable is located inside the CT and can provide information, e.g., injection profiling after a stimulation job.
2. Fiber optic embedded in a wireline or a slick line. Using fiber optic embedded in a wireline or slick line is working well in low angled wellbores (typically < 60° hole angle). If the hole angle is > 60°, a tractor can be connected to pull the fiber across a horizontal section. This can be a very attractive method to ensure the fiber is placed across the zones of interest and is a low cost solution in low angled wellbores.
3. Fiber optic included in a semi-stiff composite carbon rod[4, 5]. The slim design of the carbon rod (0.6" outer diameter) enables easy access to horizontal wellbores where there is, for instance, a downhole electric submersible pump with a Y-tool to access the wellbore. In general, the Y-tool is too narrow for a tractor to pass through, and so the wireline and/or slick line option is no longer valid. The composite carbon rod can be pushed into long horizontal wellbores from the surface, with no tractor needed. Once placed across the zones of interest, all applications mentioned here can be successfully executed. It is also possible to investigate multiple applications during the same run. For instance, the cause of a casing leak or tubing-to-annulus leak can be investigated at the same time as downhole injection profiling.

Figure 2 shows a sample of the 0.6" semi-stiff carbon rod that was tested for the first time in a few vertical oil producer and water injector wells without prior fiber optic installation. The main advantages for the composite rod is that the rod

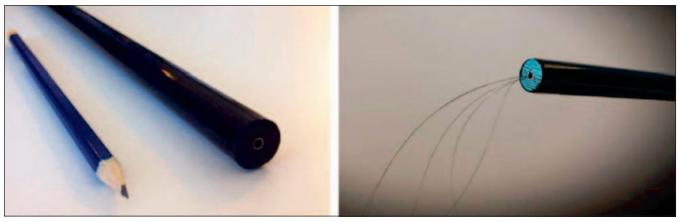

Fig. 2. Semi-stiff carbon rod for "in-well" intervention[2].

Fig. 3. Carbon rod coiled up on a drum.

Fig. 4. Memory gauge BHA attached to the tip of the carbon rod.

itself is more or less inert to the environment, being able to withstand acid and other chemicals without deteriorating.

Also, the carbon rod is very slim, in addition to having no memory of being coiled up on a drum, Fig. 3. In size, it is similar to a CT, but the carbon rod wants to be straight, and therefore does not have the same wear and tear as a steel CT will have. At the moment, the carbon rod does not have the power capability, it only contains fiber optics.

The fiber optic is used for DAS and DTS in addition to pressure and temperature point measurements located in a 3 ft bottom-hole assembly (BHA), Fig. 4. All these measurements are conveyed to the surface in real time for visualization and potentially optimization of various parameters like slug avoidance during production or injection flow rate to cover the entire reservoir. The dynamic information in real-time enables correct decisions to be made in a timely manner.

PROJECT BACKGROUND AND OBJECTIVES

The logging operation in the subject well, Well-X, is part of a multiple well investigative campaign to test the application of a novel in-well fiber optic technology, and the carbon rod, in a few vertical injection and vertical producer wells. The main objectives of the field trial test were to: (1) investigate the well's integrity across the entire length of the well, (2) assess the production and injection flow profile across the perforations and behind the casing (unperforated intervals), which until now was not possible with a conventional PLT, (3) investigate the possibility of using a combination of a distributed acoustic survey and a distributed temperature survey for quantitative production flow analysis, and (4) explore the possibility of utilizing the carbon rod for VSP data acquisition.

Well-X — the first well to be tested — is a vertical oil producer, with a perforated interval of 35 ft, having a very high unrestricted liquid flow without artificial lift. The specific sensing objectives for this well are well integrity evaluation, flow profiling and flow allocation.

Sensing Program

The sensing program for the well consists of a series of production and shutting periods using different pulse width (PW) settings of 20 ns and 50 ns, equivalent to 4 m and 10 m, respectively. The original sensing program, Table 1, was slightly modified to include a stabilization period of 4 hours prior to production-1a (20 ns PW).

Production-1 was divided into two sequences (1a and 1b) to achieve two different spatial resolutions of the DAS. It was anticipated that the PW of 20 ns would provide more zonal details. Typically, a shorter PW is a tradeoff between resolution and energy response. Generally, it could be challenging to obtain a sufficient signal-to-noise ratio with a shorter PW. Since the production rate is very high, the odds were favorable. Given the carbon rod diameter of 15 mm inside a 4½" tubing, the wellbore flow was expected to be unchoked and stable production temperatures can be recorded with negligible intervention interference. Therefore, stable production-1 temperature data can be used as input for the production curve in the interpretation software. Stable shut-in production-1 temperature data is generally used to approximate the geothermal temperature input in the software. The transient production-2 was planned to observe the dynamic start of production and possible zones. Production-3 is more of a repeat of production-2.

Sensing Program											
			Flow Allocation PW 20 ns				Flow Allocation Repeat PW 50 ns				
		Open	Open	Open	Closed	Open	Closed	Open	Open		
Beginning of Sensing	Record DTS on the Spool	RIH while Producing	Production-1a 20 ns PW	Production-1b 50 ns PW	Shut-in 1 20 ns PW	Production-2 20 ns PW	Shut-in 2 50 ns PW	Production-3 50 ns PW	POOH while Producing	Record DTS on the Spool	End of Sensing
	15 min	4 hours	2 + 2 hours		24 hours	2 hours	4 hours	2 hours	4 hours	15 min	
			Total: 44.5 hours								

Table 1. Sensing program for Well-X

FIELD DEPLOYMENT AND OPERATIONAL HIGHLIGHTS

The well, Well-X, is a natural vertical producer with no artificial lift. It was completed as a monobore producer with a 4½" liner and tubing to a depth of x465 ft. The perforated interval spans from x070 ft to x105 ft. The rig-up process involved rigging up the flanged wellhead crossover and blowout preventer (BOP). The modular Quad BOP (top, blind, slip, pipe) was function tested. Then the dual stripper, lubricator, and gooseneck were rigged up on the injector. The carbon rod was then stabbed into the injector and the gooseneck rollers were closed. The injector and stripper were rigged up on the BOP. Thereafter, the BOP rams, the strippers, and the lubricator were pressure tested to 2,500 psi. The run in hole (RIH) process began after a safety meeting was held to review all the details of the sensing operations.

The well was opened fully while the carbon rod was at 610 ft as per the sensing program. A set down weight of -2,000 lb was noticed when the carbon rod was at x192 ft. The weight drop was due to the well's high flow rate. It was then decided to shut-in the well while RIH. Pull tests were performed at every 1,000 ft or when needed to confirm the rod weight, and that nothing was holding the rod, Fig. 5.

After reaching the desired total depth (TD) at x262 ft, it was decided to start the sensing operation as per the program — production-1a. The well was gradually opened from 10%, 25%, 45%, 65%, 75%, to 100% fully open. It was observed that the weight of the carbon rod dropped as the choke was opened more, Fig. 6.

Figure 7 shows the carbon rod weight and well flow vs. time for the rest of the sensing operational sequence (shut-in 1 to production-3 to the end of sensing). At the completion of the sensing program, the carbon rod was pulled out of hole (POOH) while keeping the well flowing to record sensing data during POOH. A crack was later noticed on the carbon rod. A post-job review showed that the crack developed due to helical buckling of the rod, which was a result of a high flow rate that the carbon rod encountered while RIH. A simulation of the well flowing condition and carbon rod showed that severe helical buckling caused compression crumpling of the carbon rod once the flow rate exceeded a maximum safe production flow rate. The flow rate for the well was very high at some point during the operation; this is much higher than the maximum safe production flow rate of 8,750 barrels per day (bpd) calculated for the well conditions.

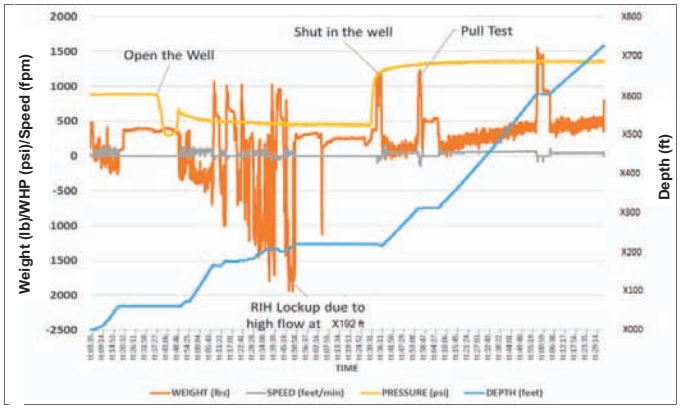

Fig. 5. RIH data — weight and depth vs. time.

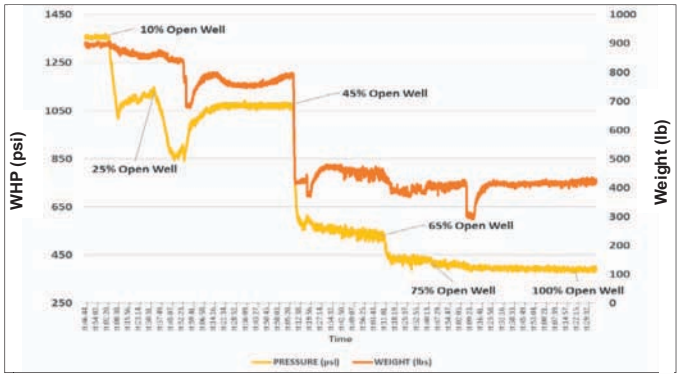

Fig. 6. Carbon rod weight and well flow vs. time for production-1 sequence.

Fig. 7. Carbon rod weight and well flow vs. time for the rest of the sensing sequence.

DATA ANALYSIS AND INTERPRETATION

A memory gauge measuring temperature and pressure data was run in the

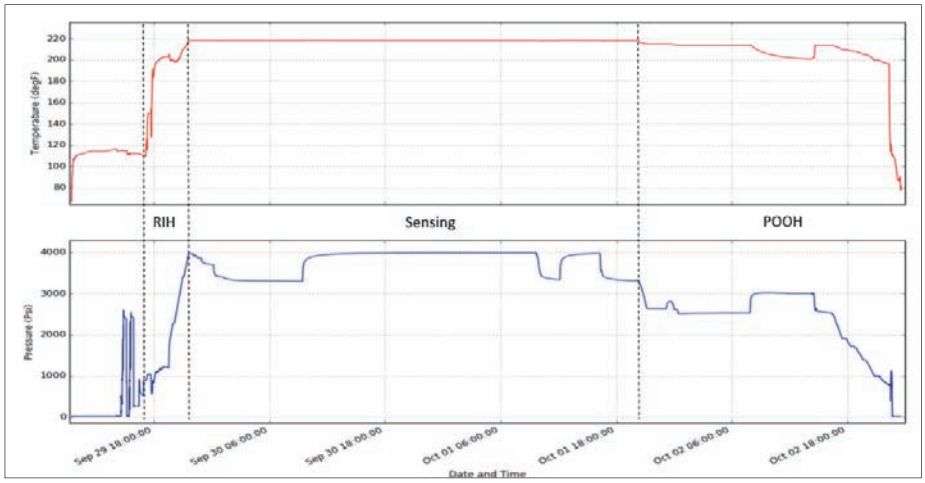

Fig. 8. Memory gauge temperature (red) and pressure (blue) as a function of time from the bullnose sensor.

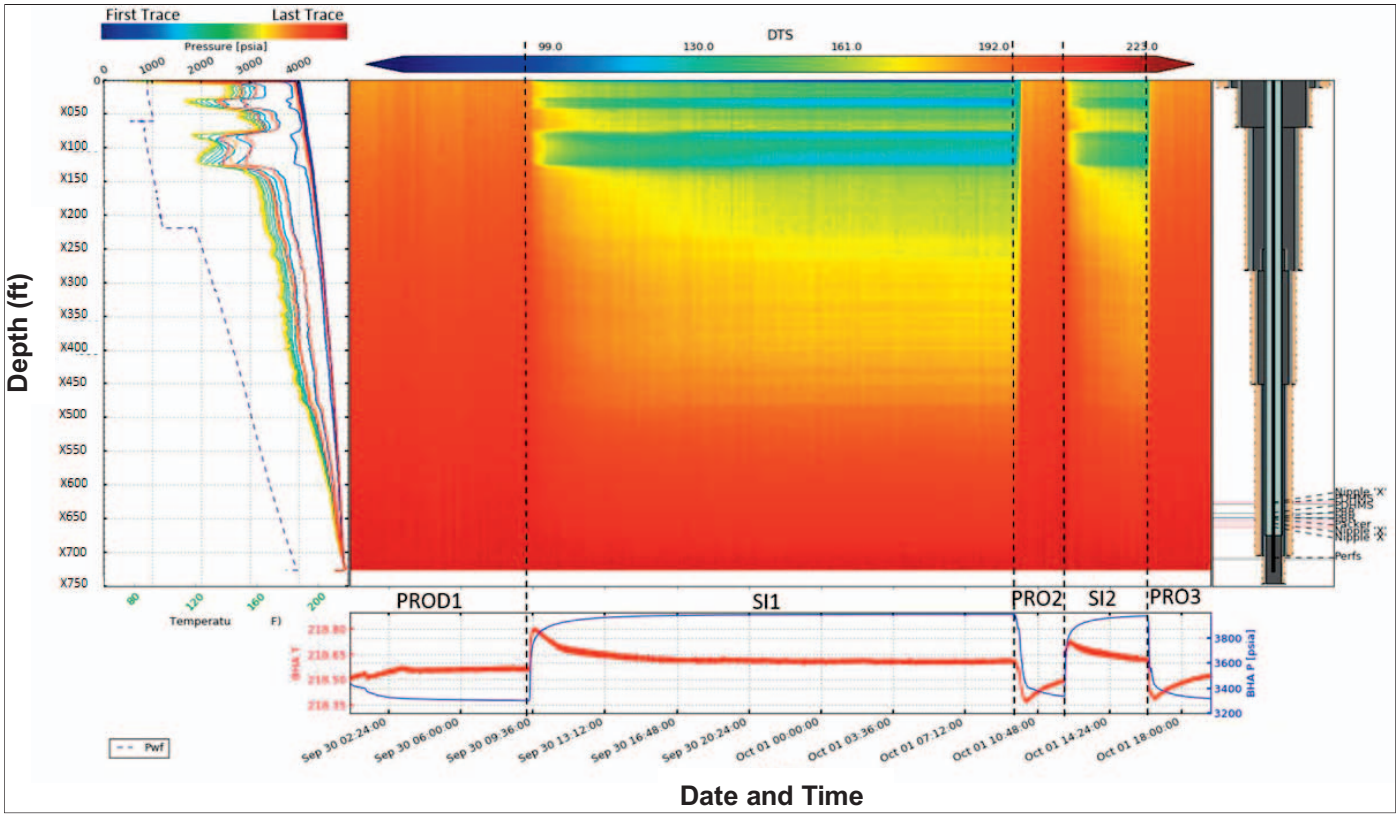

Fig. 9. The DTS overview of the entire bore length of Well-X.

BHA. This serves as a post-job quality control and a downhole DTS calibration point. The DTS data was calibrated using the memory gauge temperature as the bottom-hole reference. The memory data collected in the bullnose sensor was recorded as a function of time. It was merged with the winch depth data to obtain pressure and temperature vs. depth curve. The DTS was matched using the inflection point on the production curve during the stable production-1b as the bottom of the perforation interval. This approach was validated by a forward model showing the production curve departing and warming up quite sharply from the modeled geothermal curve. The DAS was matched assuming the maximum noise during production-1 in medium frequency bands corresponding to the perforation interval. Figure 8 shows the memory gauge temperature and pressure data from the bullnose sensor for Well-X.

The different temperature effects of each sequence can be seen in the waterfall plot, showing the entire sensing sequence from the top to TD, Fig. 9. Some of the features that are apparent on the DTS curves and the waterfall plot are: (1) a cooler shut-in region can reach above x500 ft. This was interpreted as the signature of shallow aquifers; and (2) the sharp contrast between the aquifer temperature and the rest of the wellbore initially prompted the question of potential well integrity issues around that zone.

Careful analyses of the data and comparison with the DAS data showed this is not the case; (1) the bottom-hole temperature variation at the BHA is extremely small (less than 0.5 °F) throughout the sequence of events, which is consistent with the location past and below the bottom of the perforation's interval. The observed temperature response is apparently related to pressure variations in the wellbore fluid column; (2) the end of production-1 is relatively stable as seen on the BHA pressure, which is not the case during productions 2 and 3, and (3) the end of shut-in 1 is stable as seen on the BHA pressure.

A zoom into the reservoir section of the temperature waterfall plot shows a change in temperature during the start of production, Fig. 10. It can be observed that during the shut-in sequence, hotter temperatures are in line with the perforations, which is sensed by the fiber through conductive heating. The production curves are cooling at the perforations compared to the shut-in traces, which indicates a potential gas Joules-Thomson effect, and as such, free gas production toward the top of the perforations.

The DAS overview plot of the entire sensing sequence from the top to the TD is shown in Fig. 11. It is important to highlight that a dark blue response does not necessarily mean there is no energy; it simply means that the energy is lower than that of a red response. The production sequences are recognizable as higher energy while shut-in sequences create a lower energy. In addition, the 20 ns PW intervals are relatively less energetic than the 50 ns ones.

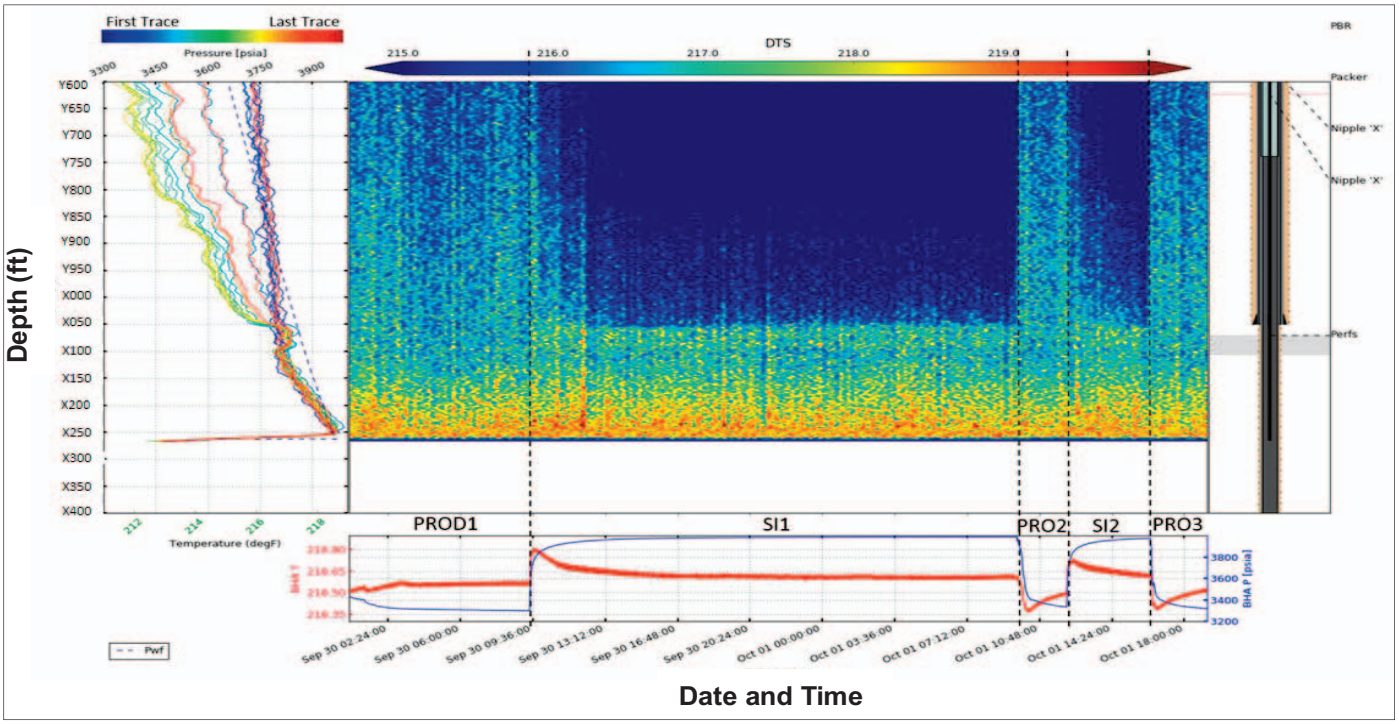

Fig. 10. DTS overview of the reservoir section.

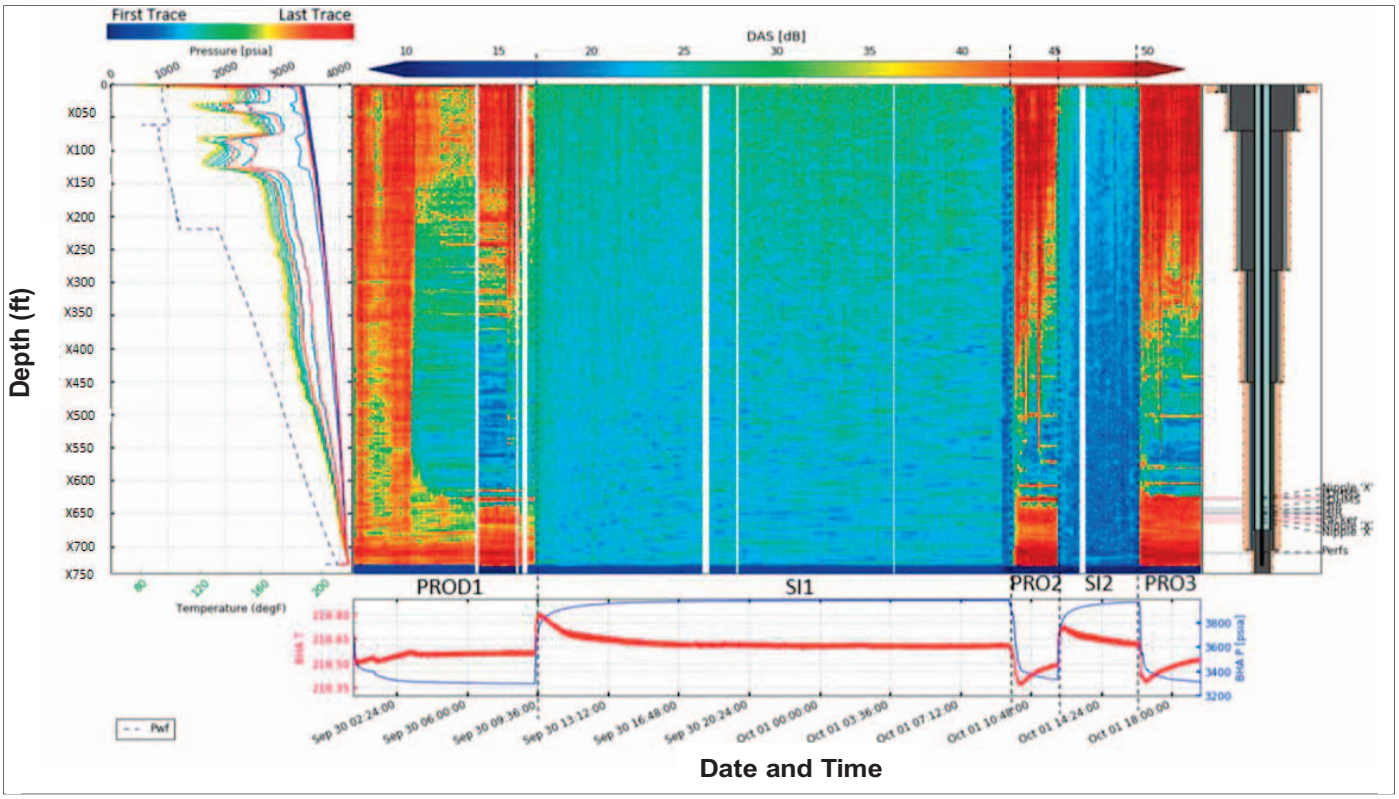

Fig. 11. DAS overview plot of the entire sensing sequence from the top to the TD.

RESULTS AND DISCUSSIONS

From the data analyses, there was no strong evidence of any well integrity issues or leakage at the aquifers. The shut-in temperature peaks previously shown in Figs. 9 and 11, develop parallel to one another vs. depth, with no sign of upward or downward fluid movement other than gravity convection. The DAS and DTS images, Fig. 12, only show evidence of convection inside the wellbore at the aquifers because of the high temperature contrast.

Quantitative analyses of the production flow profile was done using the sensing data from the DAS/DTS survey, pressure, reservoir description and deviation data as inputs into the flow simulation model to quantify the production from

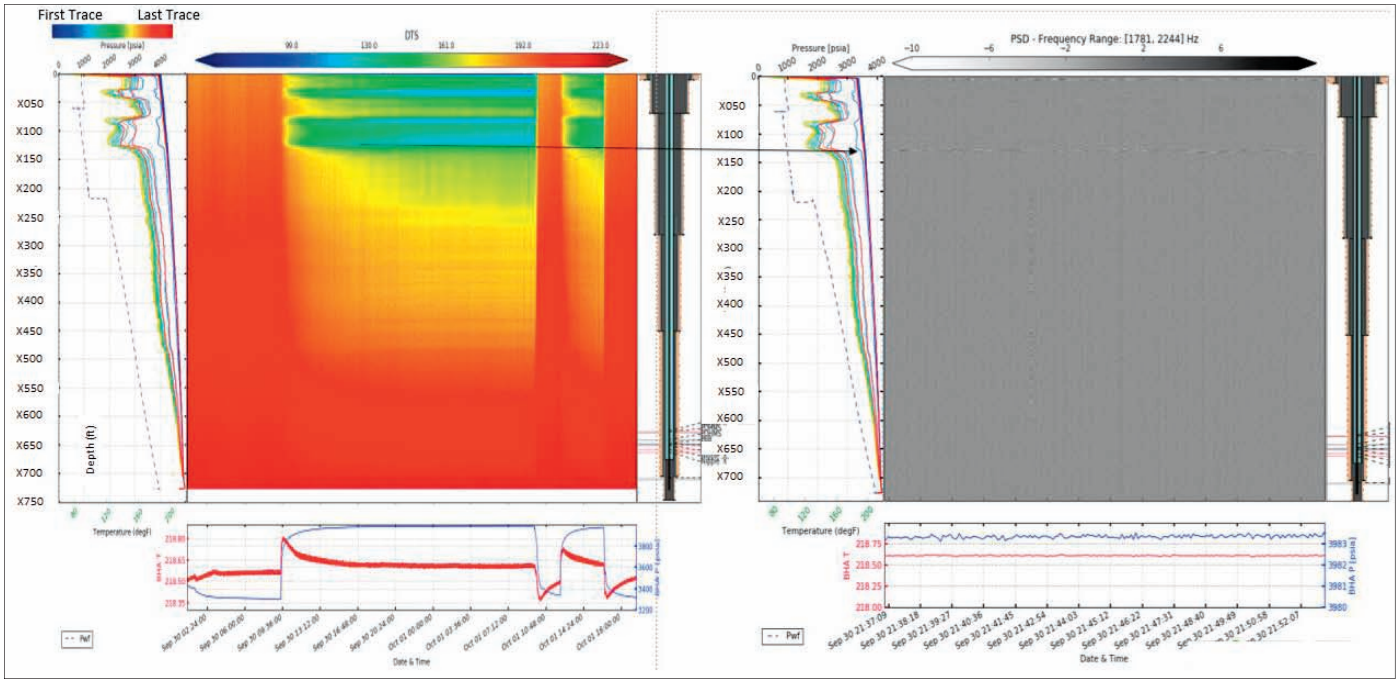

Fig. 12. DTS water fall vs. DAS (derivatives) along the entire wellbore.

the different zones. The data acquired from the different PWs during shut-in and production cycles helped to refine the vertical resolution of the flow profile from the production zones. A shorter PW is generally a tradeoff between resolution and energy response, and it could be challenging to obtain sufficient signal-to-noise ratio with a shorter PW. Since the production rate for the well was very high, the odds were favorable, Fig. 13.

Figure 14 shows the quantitative flow rate and flow profile results from the integration of the independent DAS and DTS data. It is worth noting that using the DTS data alone can generally lead to a non-unique production inflow profile. It is usually a best practice to constrain the model with the DAS data and better vertical resolution with varying PWs. The data showed that the lower zone is the main contributor of the water inflow while the bulk of the gas and oil is apparently coming from the top zones.

KEY LESSONS LEARNED

1. Helical buckling of the carbon rod due to a very high flow rate was not anticipated during the planning stage. Apparently, the carbon rod has never been used in any well with a flow rate exceeding 5,000 bpd. Although the carbon rod is very strong — over 22,000 lb tensile capacity — and quite different from the CT, its compressive strength — less than 2,200 lb — limits its application in very high rate wells without additional weight attached to the BHA.
2. Consequently, a best practice for logging high rate wells is to simulate helical buckling and establish the maximum safe production flow rate for each well's flowing condition prior to logging.
3. Where possible, and if it will not adversely affect the sensing program, consider keeping the well at shut-in during RIH and POOH operations to prevent helical buckling and/or excessive axial force.
4. For technology trials, it is always good to consider a gamut of "what ifs" and anticipate different scenarios that may become a potential show stopper.
5. A post-job detailed examination of the cracked carbon rod

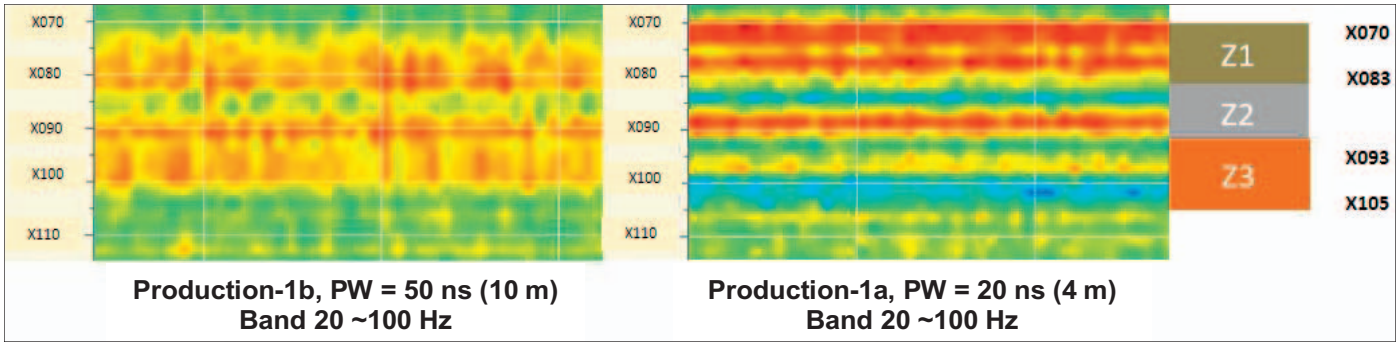

Fig. 13. DAS image PW vs. resolution across the production intervals.

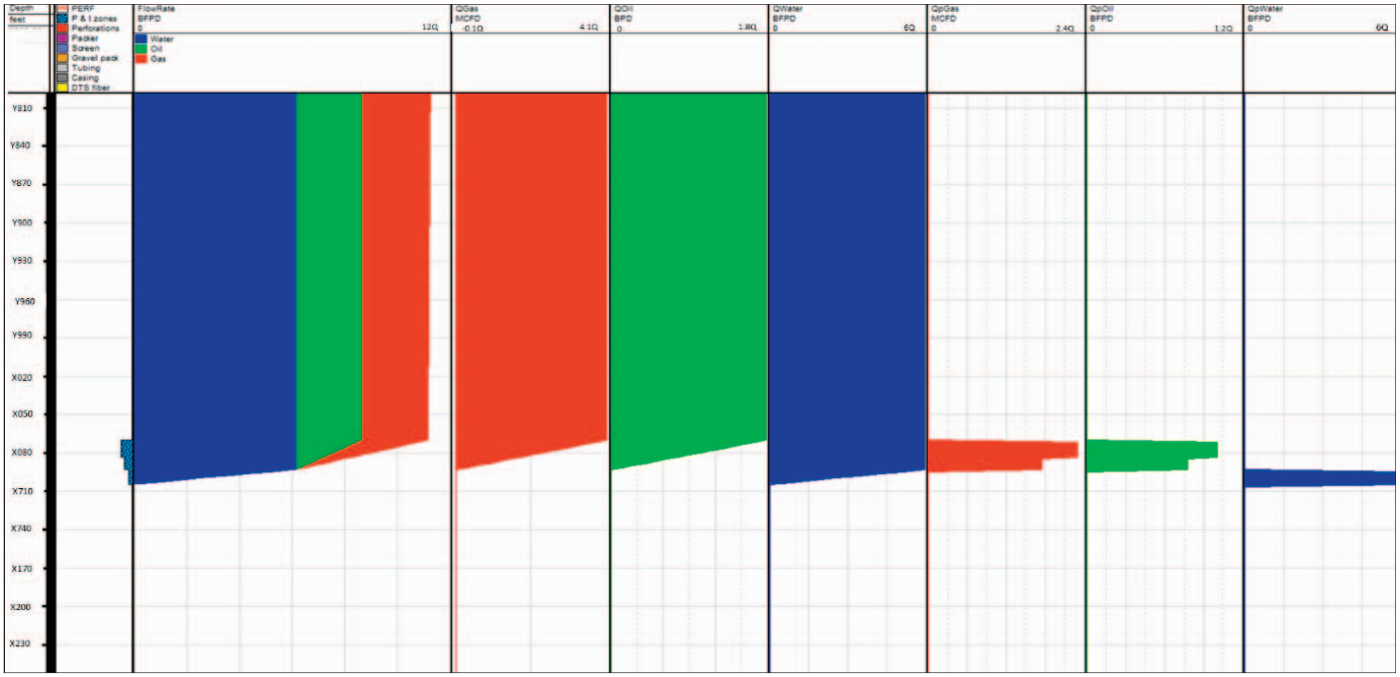

Fig. 14. Quantitative analyses of the flow rate and flow profile results.

showed no evidence of chemical damage or any reduction in physical properties as compared to the reference (original) samples.

CONCLUSIONS

1. The first field trial of the carbon rod in our operations showed it has great potential. The field trial was paused because of the crack on the carbon rod. A post-job review showed that the crack developed due to helical buckling of the rod as a result of a high flow rate that the carbon rod encountered while RIH. A simulation of the well's flowing condition and carbon rod showed that severe helical buckling caused compression crumpling of the carbon rod once the flow rate exceeded a maximum safe production flow rate.
2. The data obtained showed no well integrity issues across the entire length of the well. Using the DTS data alone would have raised a false alarm about well leakage around the shallow aquifers. The combination of the DAS and DTS data only show evidence of convection inside the wellbore at the aquifers because of the high temperature contrast.
3. The sensing data surprisingly revealed the possibility of detecting active shallow aquifers. This is not possible with conventional PLT.
4. The data obtained was used for quantitative analyses of the production flow profile. The data acquired from the different PWs during the shut-in and production cycles helped to refine the vertical resolution of the flow profile from the production zones. The analysis showed that the lower zone is the main contributor of the water inflow, while the bulk of the gas and oil is apparently coming from the top zones.

ACKNOWLEDGMENTS

The authors would like to thank the management of Saudi Aramco for their support and permission to publish this article. This article would not have been possible without the contributions and efforts of many colleagues. In particular we would like to acknowledge and thank Nabil Bulushi, Abdullah Ghamdi (Lafi), Ahmed Alsmaeil, Saad Al-Otaibi, Tariq Buzaid, Alex Crossland, Neil Gardner, and many others for their contributions toward the project.

This article was presented at the SPE Annual Technical Conference and Exhibition, Dallas, Texas, September 24-26, 2018.

REFERENCES

1. Al Shoaibi, S., Kechichian, J., Mjeni, R., Al Rajhi, S., et al.: "Implementing Fiber Optics Distributed Sensing as a Key Surveillance Tool," SPE paper 183535, presented at the Abu Dhabi International Petroleum Exhibition and Conference, Abu Dhabi, UAE, November 7-10, 2016.
2. Danardatu, H., Gregersen, S.H.H., Alterrn, E. and Pellegrini, I.: "Data Acquisition and Processing of Carbon Rod Conveyed DTS and DAS in Very Long Horizontal Wells. First Trial in North Sea Danish Sector," SPE paper 170663, presented at the SPE Annual Technical Conference and Exhibition, Amsterdam, the Netherlands, October 27-29, 2014.

3. Hveding, F. and Porturas, F.: "Integrated Applications of Fiber Optic Distributed Acoustic and Temperature Sensing," SPE paper 177222, presented at the SPE Latin American and Caribbean Petroleum Engineering Conference, Quito, Ecuador, November 18-20, 2015.
4. Gardner, N., Hveding, F. and Sambrook, R.: "Distributed Fiber Optic Technologies Drive New Intervention Applications," *Journal of Petroleum Technology*, January 2015, pp. 36-40.
5. Hansen, H., Wilberg, T.K., Stokkeland, K., Male, P.T., et al.: "Successful Deployments of a New Well Intervention Methodology in Horizontal Wellbores," SPE paper 121459, presented at the SPE/ICoTA Coiled Tubing and Well Intervention Conference and Exhibition, The Woodlands, Texas, March 31-April 1, 2009.

BIOGRAPHIES

Modiu L. Sanni is a retired Petroleum Engineering Specialist, and had worked with the Reservoir Engineering Technology Team at Saudi Aramco's Exploration and Petroleum Engineering Center – Advanced Research Center (EXPEC ARC), before retiring in 2018. Prior to joining Saudi Aramco in 2004, he worked for Shell for about 15 years in Nigeria, the Netherlands, and the Sultanate of Oman. Modiu's experience includes formation evaluation, reservoir characterization and description, integrated multidisciplinary field studies, field development and enhanced oil recovery.

He has authored and coauthored papers published at both the Society of Petroleum Engineers (SPE) and Society of Petrophysicists and Well Log Analysts (SPWLA) conference proceedings.

In 1987, Modiu received his B.S. degree, and in 1990, he received his M.S. degree, both in Mechanical Engineering from the University of Ibadan, Ibadan, Nigeria.

Frode Hveding joined the Production Technology Team of Saudi Aramco's Exploration and Petroleum Engineering Center – Advanced Research Center (EXPEC ARC) in August 2015. His work focuses mainly on flow measurements using lasers and fiber optics.

Frode has 23 years of experience in the oil industry. His main areas of expertise are distributed fiber optics for downhole applications, production logging and formation evaluation, advanced data acquisition from both wireline and logging while drilling, and the active use of real-time information for wellbore placement and geosteering.

Frode received his M.S. degree in Petroleum Technology from the Norwegian University of Science and Technology, Trondheim, Norway.

Dr. Sunil L. Kokal is a Principal Professional and a Focus Area Champion of enhanced oil recovery (EOR) on the Reservoir Engineering Technology team of Saudi Aramco's Exploration and Petroleum Engineering Center – Advanced Research Center (EXPEC ARC). Since joining Saudi Aramco in 1993, he has been involved in applied research projects on EOR/improved oil recovery, reservoir fluids, hydrocarbon phase behavior, crude oil emulsions and production-related challenges. Currently Sunil is leading a group of scientists, engineers and technicians in efforts to develop a program for carbon dioxide EOR and to conduct appropriate studies and field demonstration projects. Prior to joining Saudi Aramco, he worked at the Petroleum Recovery Institute, Calgary, Canada.

Sunil is a member of the Society of Petroleum Engineers (SPE), and he is a Registered Professional Engineer and a member of the Association of Professional Engineers, Geologists and Geophysicists of Alberta, Canada.

He has written over 100 technical papers. Sunil has served as an associate editor for the *Journal of Petroleum Science and Engineering* and for SPE's *Reservoir Evaluation and Engineering Journal*, and he earlier served on the Editorial Review Board of the *Journal of Canadian Petroleum Technology*.

He is the recipient of the prestigious 2016 SPE Honorary Member Award, the 2012 SPE DeGolyer Distinguished Service Medal, the 2011 SPE Distinguished Service Award, the 2010 SPE Regional Technical Award for Reservoir Description & Dynamics, and the 2008 SPE Distinguished Member Award for his services to the society. Sunil also served as a SPE Distinguished Lecturer during 2007-2008. Currently he is the Chair of the SPE Distinguished Lecturer Committee.

In 1982, Sunil received his B.S. degree in Chemical Engineering from the Indian Institute of Technology, New Delhi, India, and in 1987, he received his Ph.D. degree in Chemical Engineering from the University of Calgary, Calgary, Alberta, Canada.

Ibrahim M. El-Zefzafy is a Petroleum Engineering Specialist with Saudi Aramco's South Ghawar Production Engineering Division of the Southern Area Production Engineering Department. He has 24 years of experience in the oil and gas industry in rigless well intervention, oil artificial lift design, well performance and production optimization, well completion and testing, and workover interventions. Ibrahim also has comprehensive well services and production enhancement experience in onshore and offshore operations.

Since joining Saudi Aramco in 2006, he has been involved in a wide variety of technical projects and planning activities as part of oil development and enhanced oil recovery projects. Ibrahim manages a team responsible for the introduction and implementation of new technology applications, including developing engineered solutions to improve productivity, in collaboration with Saudi Aramco's Exploration and Petroleum Engineering Center – Advanced Research Center (EXPEC ARC) and the Research and Development Center (R&DC).

Prior to joining Saudi Aramco, he worked as a District Production Engineer with Gulf of Suez Petroleum Company's joint venture with BP in Egypt.

Ibrahim is a registered member of the Society of Petroleum Engineers (SPE), and he has authored and coauthored numerous SPE papers.

In 1995, Ibrahim received his B.S. degree in Petroleum Engineering from Al-Azhar University, Cairo, Egypt.

Drilling and Acidizing Sandstone Stringers — Sludge Characterization and Acid Interactions with Rock Minerals: Integrated Geochemical and Engineering Techniques

Dr. Bandar I. Ghassal, Dr. Abdullah M. Al Moajil, Dr. Sami Abdelbaqi, and Abdullah A. Al-Rustum

ABSTRACT

Understanding the sludge types and causes is essential to preventing various drilling issues, especially during the drilling of heterogeneous sandstone reservoirs where the permeability is variable. Acidizing these sandstone reservoirs is challenging because of their inconsistent mineralogical types and contents resulting in different reaction behaviors with drilling fluids and acidizing recipes. The current study uses new techniques to assess sludge types.

The sludge characterization revealed two types that are different in appearance and composition. The first type is solid, and is characterized by black to brownish colors, vitreous luster, and conchoidal fractures. This is described as bituminous sediment. The pyrolysis results showed that the sludge samples are composed of a mixture of diesel and solid bitumen or coal fragments. Therefore, the samples were investigated with organic microscopy techniques. The coal particles contain vitrinite, tellovitrinite, resinite, and solid bitumen. Part of the samples were treated with xylene to extract the hydrocarbon portion. The result revealed that the sludge sample is composed of 70 wt% organic matter and the remaining is inorganic. Calcite constitutes 82 wt% of the inorganic components, leaving 18 wt% for silicate minerals. Most of this type 1 sludge was dissolved by xylene. This indicates that they represent solid bitumen, which absorbs oil-based drilling fluids. This results in destabilizing the substrate, which causes the bit to abort drilling. Therefore, water-based drilling is recommended in this case. The type 2 sludge is composed of fine-grained sediments saturated with liquid hydrocarbon — mostly oil. A total of five sludge samples were characterized by high resolution pyrolysis and revealed variable saturates, aromatic, resin, and asphaltene percentages corresponding to different degrees of oil and drilling fluid incompatibilities.

The type 2 sludge sample showed a slight solubility in mutual solvents and xylene at 160 °F, i.e., 5 wt% to 19 wt%. The dissolution of the type 2 sludge sample in formic acid was higher than acetic acid when mixed with either ether-based mutual solvent or microemulsion solvent. The highest solubility values were obtained with mixtures of 5 wt% hydrochloric (HCl) acid mixed with solvents, showing solubilities between 79 wt% to 88 wt%.

Coreflood experiments utilizing HCl acid and formic acid mixtures showed a slight reduction in permeability — i.e., 20% — using highly permeable sandstone core plugs. Injection of HCl acid and formic acid mixtures or 10 wt% formic acid in the presence of 0.4 vol% clay stabilizer showed a reduction in the permeability by 5% to 13%. Although, the coreflood experiments showed a slight reduction in permeability, the computed tomography (CT) scan results obtained showed a significant increase in rock density along the core length for core plug Nos. 2 and 3, indicating the occurrence of chemical reactions with rock minerals that had an insignificant impact on the core permeability.

INTRODUCTION

Marine sandstone formations are among the most prolific oil producing reservoirs in the world. Due to their litho-heterogeneity and extreme capriciousness in their permeability, drilling and acidizing them become very challenging. Their litho-heterogeneity evolve inconsistent interactions between the drilling fluid and the stimulation recipe throughout the reservoir, as they usually have a wide range of mineralogical compositions. Because of frequent and rapid sea level fluctuations upon the deposition time, the reservoir stratigraphy alternates between several lithologies. For example, such reservoirs can be composed of two types of argillaceous sandstones that alternate with argillaceous siltstone. It also encompasses organic-rich layers. The common minerals are quartz, plagioclases, K-feldspars, lithic fragments, mica, siderite, ferroan dolomite, calcite, kaolinite, chlorite, illite, pyrite, and organic matter. The reservoir properties can be affected by siderite or carbonate cement as well as quartz overgrowth. These minerals differ significantly in their sensitivity to acid, which accentuates the importance of studying the controls on the reservoir mineralogy, and the anticipated chemical interactions. Such interactions with acid recipes were summarized by Al Moajil et al. (2018)[1]. Recognizing the lithology will help with optimizing drilling fluid planning.

The permeability variations cause uneven distribution of filter cake and massive losses in high permeable streaks. Losses of drilling fluids and high viscous pills, e.g., hydroxyethyl cellulose, can exceed hundreds of barrels until the well is

controlled. This adds more to well completion challenges along with sludge formation and production, due to downhole fluid incompatibility with oil.

Acidizing to remove drill-in fluid damage becomes more challenging in the presence of sand production problems, especially in horizontal wells extending over 3,000 ft. The removal of filter cake caused by oil-based mud (OBM) is commonly conducted by either a conventional drilling fluid spacer — viscous brine — or a special acidizing recipe[2]. This depends on the type of the drill-in fluid and the amount of the occurring damage. A successful recipe for filter cake removal does not necessarily work well upon injection to the formation due to interactions with the rocks. The interaction can result in formation damage caused by mineral precipitation, clay mineral swelling, sand production or oil incompatibility[1].

The main challenges faced during drilling and remedial operations were a high fluid loss, the formation of sludge materials, pumping high volumes of hydroxyethyl cellulose-based viscous fluids, and both organic and inorganic precipitations because of incompatibilities with the formation rock[1]. Drilling operations are occasionally aborted due to sludge formation that usually results from the incompatibility between drilling fluids and acid treatments, the oil type, and reservoir lithology[3]. The current study identifies a unique sludge type and possible formation causes, and proposes solutions to avoid them. This article attests the formation damage potential and types when injecting commonly used acid formulations.

EXPERIMENTAL STUDY

Materials

Solvents and acids such as hydrochloric (HCl), formic, and acetic acids, and ether-based mutual and sulfonic-based solvents were obtained for solubility testing. Table 1 shows a typical HCl acid and formic acid recipe, which was prepared for coreflood testing. Sandstone core plugs and organic sludge samples commonly found in highly heterogeneous and permeable argillaceous sandstones that alternate with argillaceous were obtained. The sandstone core samples are characterized by medium to coarse grain size and occasional calcite veinlets and stylolites.

Additive	Concentration
Freshwater/NH_4Cl	4 to 6 wt%
Mutual solvent	10 vol%
Surfactant	0.2 to 0.3 vol%
HCl acid	10 wt%
Formic acid	5 wt%
Acetic acid, iron reducing agent	10 gal/1,000 gal
Citric acid, iron chelating agent	50 lb/100 gal
Corrosion inhibitor	5 gal/1,000 gal

Table 1. Typical acid recipe used in compatibility and coreflood testing

The core plugs obtained for the study were highly permeable sandstone stringers. Siderite-rich sandstone and limestone facies were present. The detrital grains are monocrystalline quartz, plagioclases, with a few K-feldspars, lithic fragments, muscovite mica, and organic matter. Authigenic minerals include siderite, ferroan dolomite, calcite, kaolinite, chlorite, illite, pyrite, and quartz. The organic samples were in two types. The first type is a mixture of material that are brittle and black to brownish black in color and show conchoidal fractures and vitreous luster with fine-grained gray sediments. This is described as a bituminous sediment, Fig. 1. The second sludge type is soft and oily material in fine- to medium-grained matrix, Fig. 2.

Solvent Exactions

Bituminous sediments were extracted with a solvent mixture of methanol (15 vol%), acetone (15 vol%), and chloroform (70 vol%) to remove bitumen and diesel. Other fractions of the sludge samples were treated with xylene to remove the remaining organic propositions, and leave the inorganic solids.

X-ray Diffraction

Aliquots of crushed core and residual solids from the xylene treated sludge samples were assessed for their mineralogical composition by using the X-ray diffraction (XRD) technique, Table 2.

Fig. 1. A bituminous sediment sample (sludge type 1) from an organic rich layer in a sandstone reservoir. The samples have a black vitreous luster with conchoidal fractures. They represent the filling of available porosity because of the thermal conversion of kerogen. Their microscopic appearance reflects the shape of the void they fill.

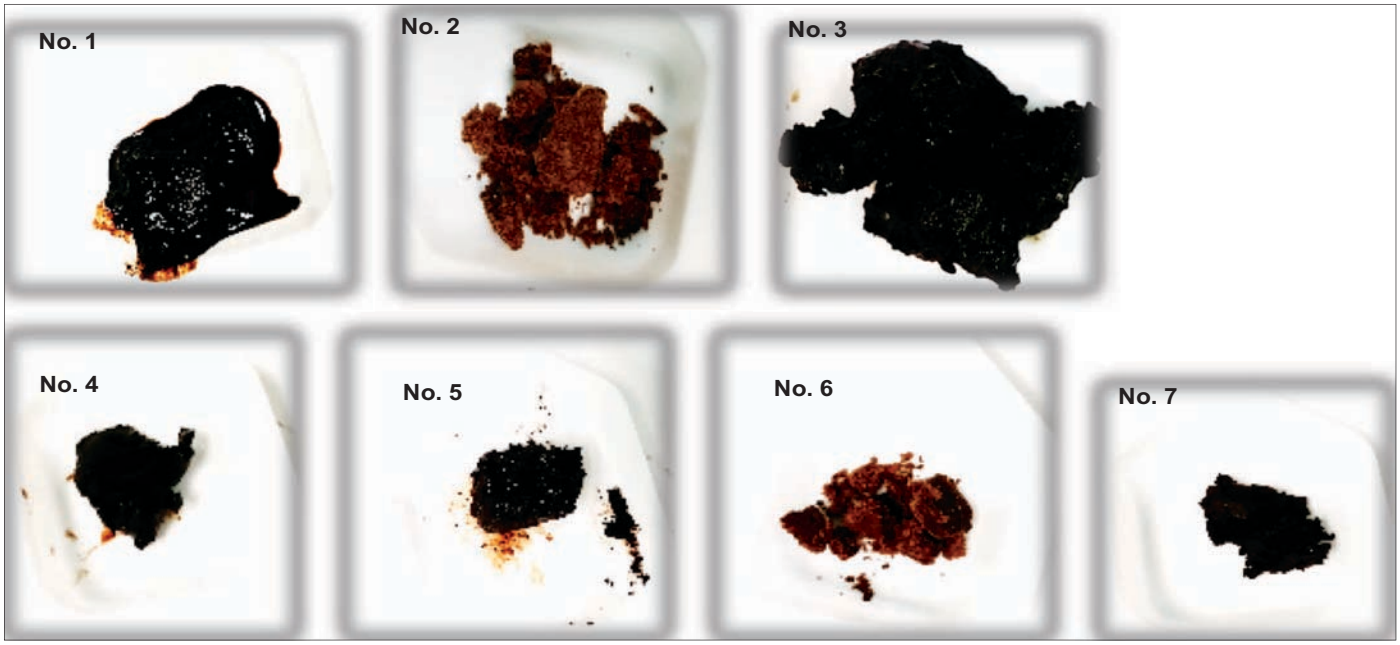

Fig. 2. Type 2 sludge samples, a soft and oily material in fine- to medium-grained matrix.

Mineral	Concentration (wt%)	
Quartz (SiO_2)	73	80
Plagioclase ($CaAl_2Si_2O_8$ or $NaAlSi_3O_8$)	2	1
Orthoclase ($KAlSi_3O_8$)	2	1
Siderite ($FeCO_3$)	9	6
Smectite	4	3
Illite (K, H_3O) (Al, Mg, Fe)$_2$(Si, Al)	3	2
Kaolinite ($Al_2Si_2O_5(OH)_4$)	6	5

Table 2. Generalized mineralogical analysis conducted by XRD of the sandstone samples

Pyrolysis

Selected sludge samples were analyzed using a high resolution pyrolysis method — the HAWK Petroleum Assessment Method (PAM)™ by Wildcat Technologies. An aliquot of 40 mg of powdered rock or oil mixed with clean sand is put in a crucible and then inserted in a pyrolysis oven. In a single run, the oven heats the sample in an inert condition at five isothermals separated by multiple ramps of 25 °C per minute. This generates five peaks in a pyrogram — the pyrolytic response of the sample — assigned to specific hydrocarbon ranges.

Organic Microscopy

Selected bituminous sediment samples were studied using organic petrology. Whole rock plugs were prepared using a cold setting epoxy resin. These were polished and detrital organic matter fragments were identified microscopically in reflected and fluorescent light. The standard technique of coal petrography[4] and the reflectance investigation technique[5] were used. The preparation method of whole rock plugs are best described by Sachse et al. (2012)[6].

Solubility Testing

The solubility of the type 2 sludge samples was examined in various acids and solvents. The samples were soaked in the fluid mixtures at 160 °F for 16 to 20 hours in an oven. The solubility values were calculated based on the sample's dry weight before and after solubility testing. The fluid samples were filtered using 0.45 µm filter paper following the solubility experiments. The sludge samples were dried at 212 °F for 16 to 20 hours prior to the weight measurements.

Coreflood Experiments

The coreflood system was used to measure the pressure drop across the core plugs. Potassium chloride (KCl) brine was injected at the beginning at flow rates of 1.0 cm^3 per minute, 2.0 cm^3 per minute, and 3.0 cm^3 per minute to measure differential pressure and test the quality. The acid recipe was then injected into the core plug, followed by the brine fluid. The experiments were conducted at 160 °F, 1,000 psi pore pressure, and 2,000 psi confining pressure.

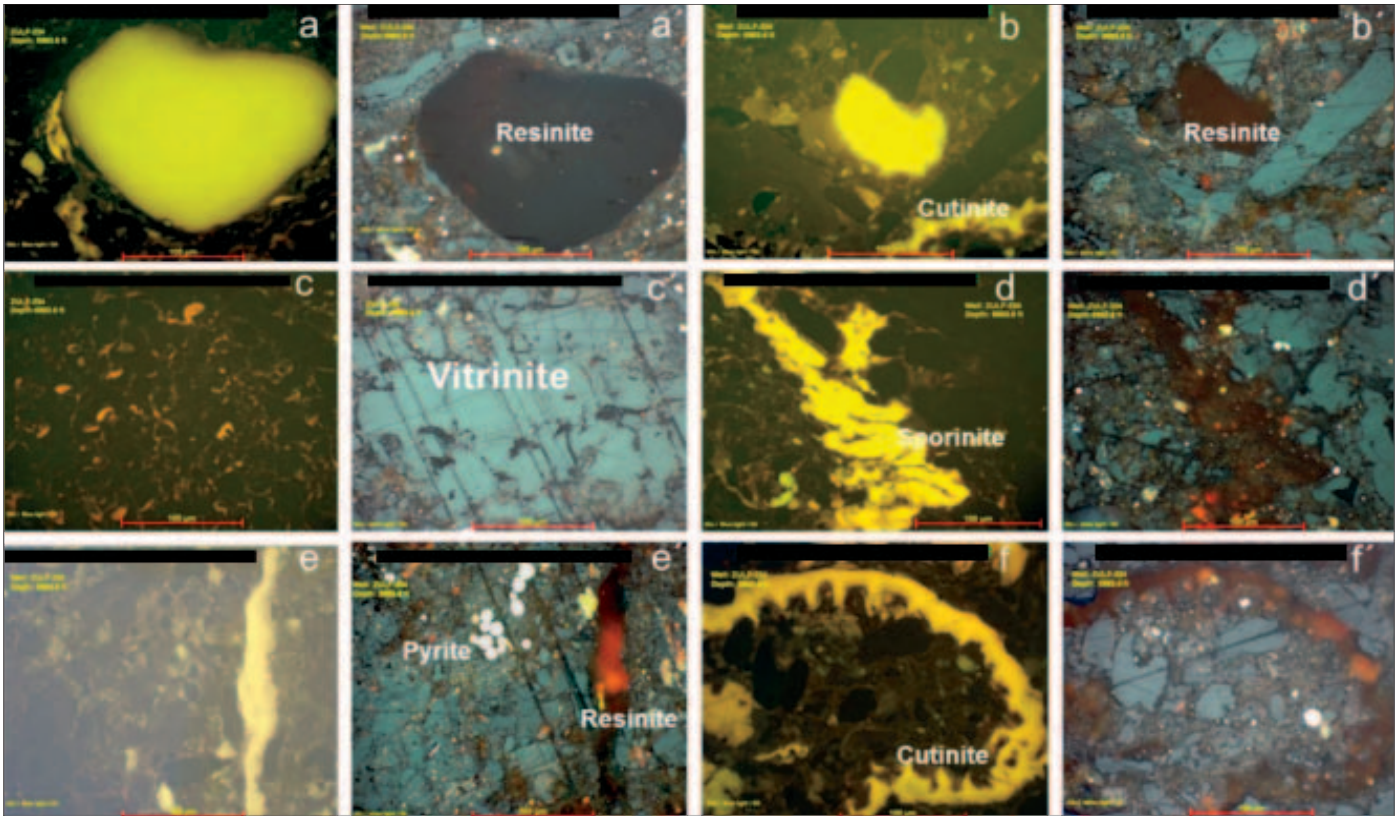

Fig. 3. Bituminous sediment samples include a mixture of coal and kerogen particles. Scale bar = 100 µm.

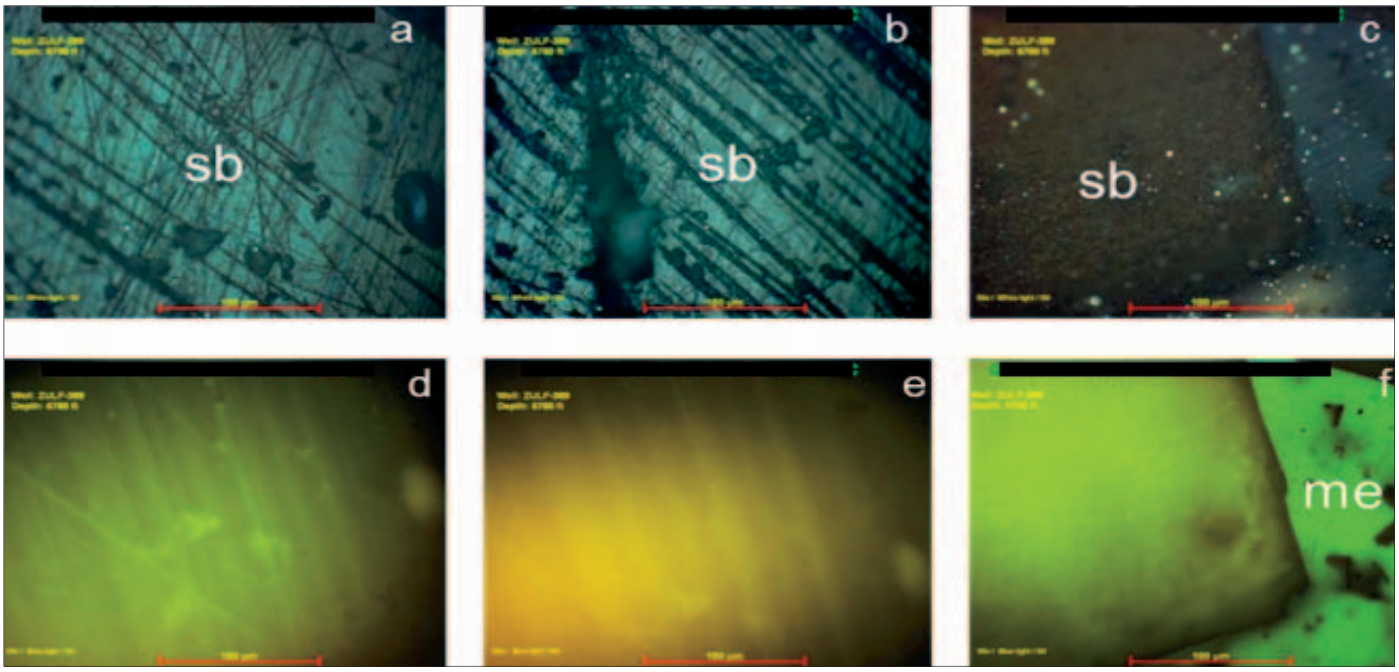

Fig. 4. Two phases of solid bitumen: A dominant phase with moderately strong, orange-brown fluorescence, and a subordinate phase with strong, green-yellow fluorescence. The moderately strong green-yellow fluorescence of mounting epoxy (me) is the result of epoxy acting as an organic solvent and extracting oil out of bitumen (a, b, and c). Reflected white light, oil immersion; (d, e, and f) blue light irradiation, oil immersion. Scale bar = 100 µm.

RESULTS AND DISCUSSION

Sludge Characterization

Bituminous sediments — type 1 sludge — were characterized for their composition with variable organic microscopic and geochemical techniques. Such materials can be found during operations in siliciclastic reservoirs. The bituminous sediment samples are fine-grained and gray, and include relatively big particles of solid bitumen with black color, vitreous luster, and conchoidal fractures. They are also characterized by a strong odor of diesel or synthetic oil. The pyrolysis analysis

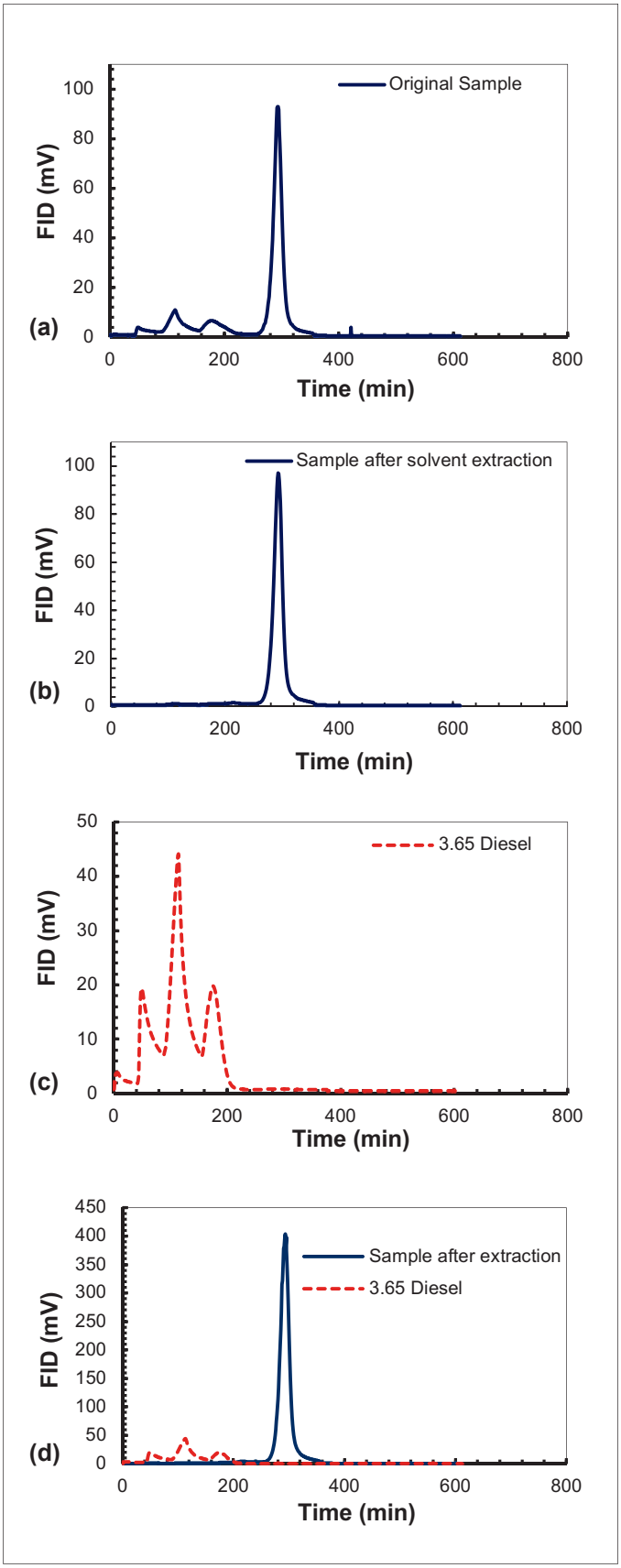

Fig. 5. Pyrolytical results of the bituminous sediment sample using the PAM™: (a) A pyrogram of the original sample illustrating four peaks; (b) a pyrogram of the solvent extracted sample demonstrating only the late peak, indicating kerogen or solid bitumen; (c) a pyrogram of the diesel sample; and (d) the combined diesel and extracted sample showing identical pyrolytical behavior of the original sample, suggesting that the original sample is a mixture of diesel and indigenous organic matter.

suggests that the samples contain solid bitumen contaminated with diesel or synthetic oil. They most probably represent the filling of available porosity because of the thermal conversion of kerogen and or severe biodegradation of the reservoir oil.

The organic microscopic assessment indicates that the samples contain a mixture of coal fragments, and solid bitumen embedded in the mineral groundmass. The coal fragments contain diverse kerogen types, which include vitrinite, cutinite, resinite, sporonite, and exsudatinite, Fig. 3. Occasionally, the vitrinite is surrounding the resinite, which does not appear to be fluorescence. This difference in fluorescence properties is commonly used to distinguish macerales from each other.

The presence of a darker rim around the outside of the maceral, Figs. 3a and 3ā, is also a common feature that is sometimes called a reaction rim caused by weathering of the coal maceral[7]. The samples contain two phases of solid bitumen. The first phase has moderately strong orange-brown fluorescence. The second phase is subordinate with strong green-yellow fluorescence, Fig. 4.

In further investigation of the hydrocarbon type, a sample was analyzed by using the high resolution pyrolysis method — PAM™, Fig. 5. The sample was analyzed before (bulk) and after the methanol, acetone, and chloroform extraction, Figs. 5a and 5b. A 3.6% diesel solution mixed with clean sand was run by the same methods, Fig. 5c. The sample before extraction shows peaks indicating a light, and a very heavy hydrocarbon mixture. The PAM pyrogram of the extracted sample shows only the last peak, indicating a very heavy or solid hydrocarbon. The combination of the diesel and the extracted sample pyrograms are plotted in Fig. 5d. It is clearly shown that Fig. 5d looks identical to the pyrogram of the original sample in Fig. 5a. Therefore, it can be concluded that this sample contains indigenous solid bitumen mixed with diesel or synthetic oil from drilling fluids.

A part of the sample was treated with xylene to remove all types of hydrocarbons, and then these were characterized by XRD analysis for their mineral composition. The solubility test indicates that the 70 wt% of the sample is solid bitumen and 30 wt% is sediment. The XRD analysis revealed that the inorganic component of the sample is composed of calcite (82 wt%), quartz (16 wt%), microcline feldspar (1 wt%), and halite (1 wt%), Table 3. The absence of clay eliminates the potential for swelling, and any pore problems.

The fact that the sample is almost completely dissolved in xylene confirms that this sample is a solid bitumen rather

Compound	Concentration (wt%)
Calcite ($CaCO_3$)	82
Quartz (SiO_2)	16
Microcline ($KAlSi_3O_8$)	1
Halite (NaCl)	1

Table 3. XRD analysis of the residual solids of the xylene treated bituminous sediment sample (type 1)

Compound by XRD	Concentration (wt%)	Element by XRF	Concentration (wt%)
Calcite ($CaCO_3$)	72	Ca	38.24
Dolomite ($CaMg(CO_3)_2$)	16	Ba	7.60
Quartz (SiO_2)	9	Mg	5.14
Halite (NaCl)	2	Si	4.96
Kaolinite ($Al_2Si_2O_5(OH)_4$)	1	Al	3.08
Pyrite (FeS_2)	Trace	Cl	2.54
Microcline ($KAlSi_3O_8$)	Trace	Fe	2.07
		S	1.86

Table 4. Composition of the type 2 sludge sample 7 after XRF and XRD analyses

than bituminous coal. In this case, oil-based drilling will be absorbed by the solid bitumen and make the substrate unstable and cause the bit to abort drilling. Water-based drilling should be utilized to drill such formations.

The second type of sludge is characterized by soft appearances and fine-grained sediments saturated by liquid hydrocarbon — a mixture of oil and diesel from drilling — and varies in color. The samples were assessed for their organic and inorganic composition utilizing pyrolysis, X-ray fluorescence (XRF) and XRD techniques, respectively. Sample number 2, which is brown in color, is rich in saturate and aromatic compounds and have very low asphaltene contents unlike the other samples. Samples 3 and 4, which have similar appearances, have a higher abundance of saturates and aromatic compounds compared to samples 5 and 7. Sample 7 was selected for XRF and XRD analyses and illustrated dominance of carbonate mineralogy, Table 4. The later samples have a high abundance of resin and asphaltene compounds, Table 5.

Sample Number	Saturates and Aromatics (%)	Resins (%)	Asphaltene (%)
2	84.93	11.77	3.31
3	64.19	20.22	15.59
4	54.67	25.40	19.93
5	33.60	40.74	25.66
5	33.57	40.82	25.61
7	28.07	43.35	28.58

Table 5. Saturates, aromatics, resin, and asphaltene data based on the pyrolysis of the type 2 sludge samples

Solubility Testing

The solubility of type 2 sludge samples — 1 to 7 — was measured at 160 °F using various organic or inorganic acids and aliphatic or aromatic solvents, including sulfonic-based microemulsifying surfactants. Mutual solvents and xylene showed slight solubility values, i.e., 5 wt% to 19 wt%, with the examined sludge samples. The solubility values were slightly higher using mixtures of acetic and mutual solvents, i.e., 17 wt% to 35 wt%, in samples 1 to 6, indicating the presence of acid soluble inorganic compounds, Fig. 6.

The dissolving power of formic acid is higher than acetic acid. Therefore, the solubility values for samples 1 to 6

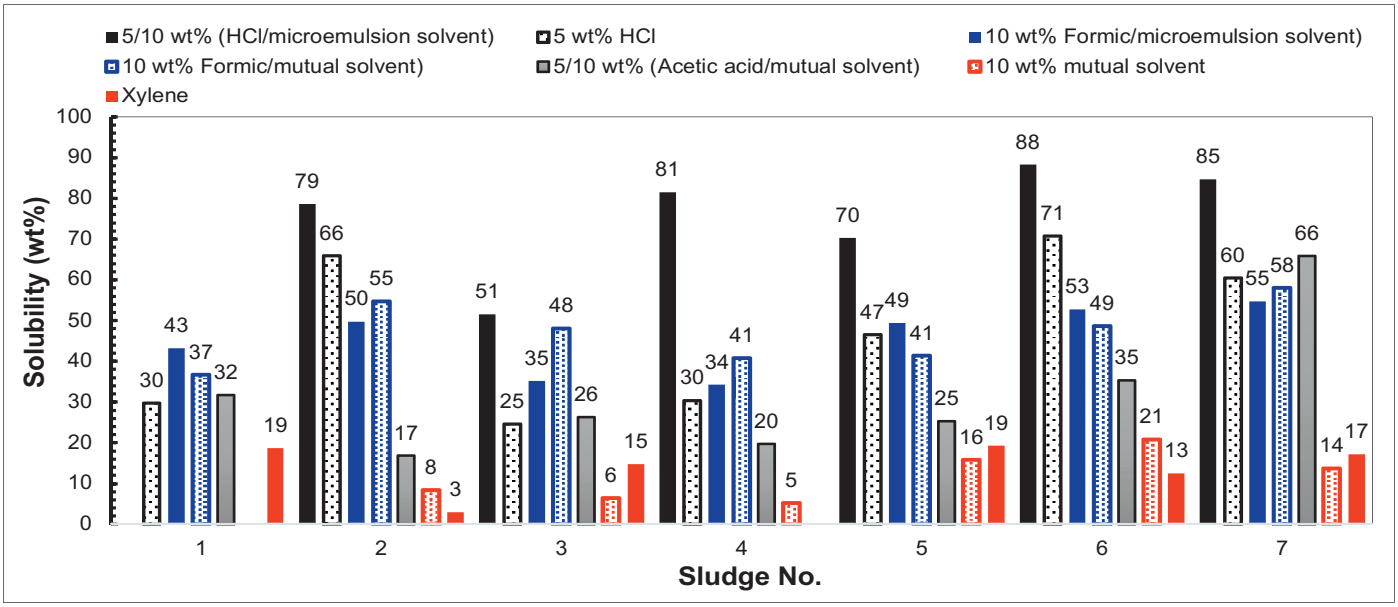

Fig. 6. Solubility of the type 2 sludge samples in acids and solvents at 160 °F.

were higher using a mixture of formic acid with either an ether-based mutual solvent or microemulsion solvent, i.e., 34 wt% to 55 wt%, Fig. 6. The microemulsifying surfactant showed no advantage over the mutual solvent when mixed with formic acids. Therefore, utilizing a mutual solvent in field treatment would be sufficient and cost-effective. The highest solubility values were obtained with mixtures of 5 wt% HCl acid and solvents, showing solubilities between 79 wt% to 88 wt% in sludge samples 2 to 6, Fig. 6. The solubility of sludge samples 1 to 6 in 5 wt% HCl acid showed inconsistent results, i.e., 25 wt% to 71 wt%.

Indicating the presence of a mutual solvent in the acid mixture is essential to maximize the dissolutions of sludge samples. Sludge sample 7 differs significantly in its solubility values compared to samples 1 to 6. All acid mixtures showed high solubility values between 55 wt% to 66 wt%. The highest solubility was obtained with a mixture of 5 wt% HCl acid and 10 wt% solvent, i.e., 85 wt%.

Coreflood Testing and CT Scan Analysis

Coreflood experiments were conducted using HCl acid and formic acid mixtures previously shown in Table 1, or 10 wt% formic acid. The examined core plugs were subjected to a CT scan before and after coreflood testing. The injection of an HCl acid and formic acid recipe into sandstone core plug 1 at 160 °F showed a slight reduction in permeability by nearly 20%, Fig. 7.

In another experiment, core plug 2 was first flushed by 3 pore volumes (PV) of 6 wt% KCl brine and 0.4 vol% polymeric cationic clay stabilizer followed by a HCl acid and formic acid recipe, with 0.4 vol% clay stabilizer. The coreflood testing results showed no damage occurred to the core plug, Fig. 8.

In a third experiment, a slight damage to core plug 3 was observed, i.e., 11% to 13%, following the injection of 10 wt% formic acid with 0.4 vol% clay stabilizer, Fig. 9. Although the coreflood results showed no or slight damage to the core plugs, a significant change in the CT scan was observed with core

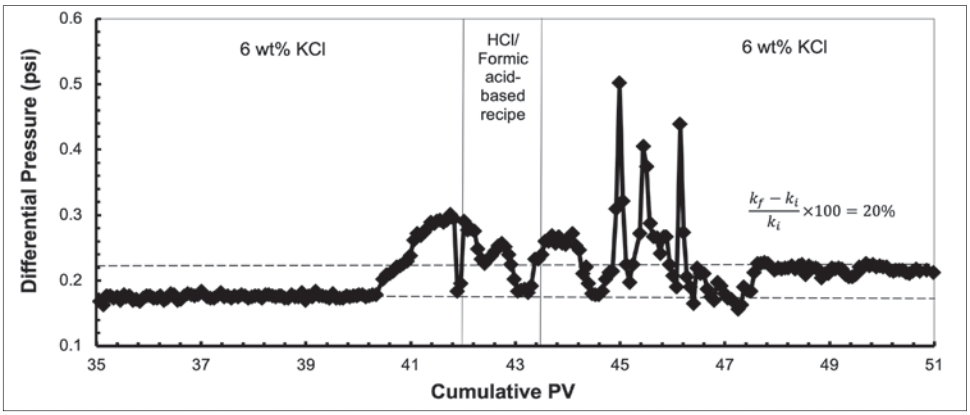

Fig. 7. Injection of a HCl acid and formic acid-based recipe into sandstone core plug 1 at 160 °F. The pore pressure was 1,000 psi and the confining pressure was 2,000 psi.

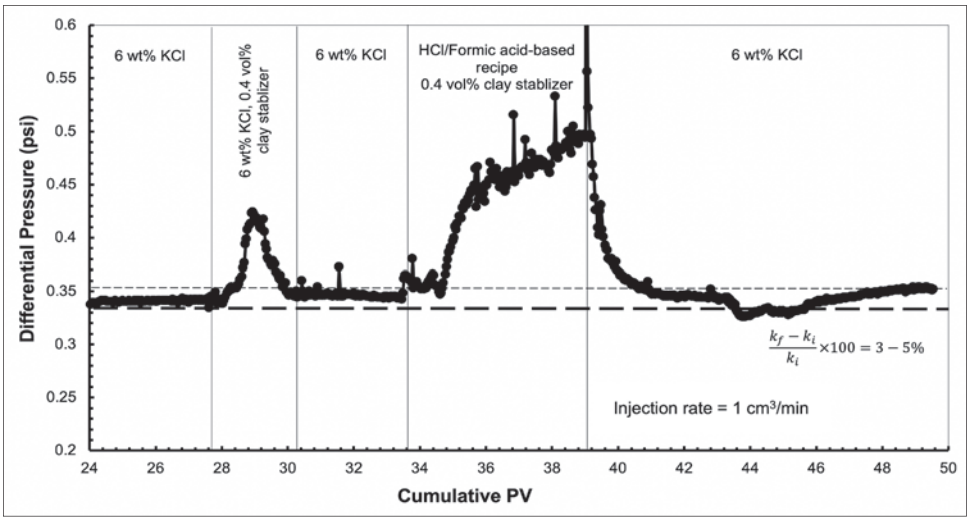

Fig. 8. Injection of HCl acid and formic acid-based recipe with 0.4 vol% clay stabilizer sandstone core plug 2 at 160 °F. The pore pressure was 1,000 psi and the confining pressure was 2,000 psi.

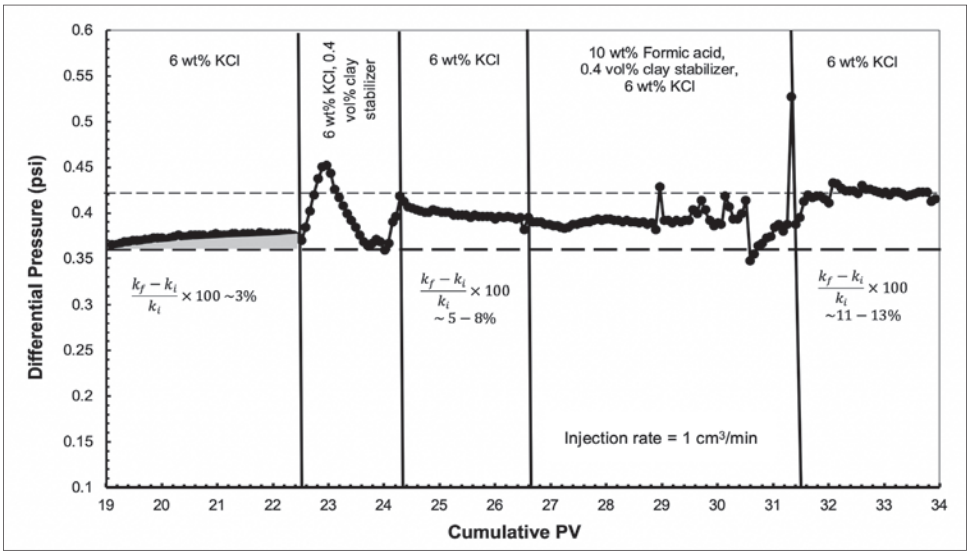

Fig. 9. Injection of a 10 wt% formic acid-based recipe with 0.4 vol% clay stabilizer into sandstone core plug 3 at 160 °F. The pore pressure was 1,000 psi and the confining pressure was 2,000 psi.

plugs 2 and 3, Figs. 10 and 11, respectively. In both experiments, the CT scan numbers — density — increased along the core length, especially at the core's inlet. This suggested a significant chemical interaction between the acid recipes and the core minerals, indicating the presence of acid sensitive minerals. In contrast, there was no significant change in the density profile observed in core plug 1, Fig. 12, which indicated the examined core plugs were heterogeneous with major variations in mineralogical composition.

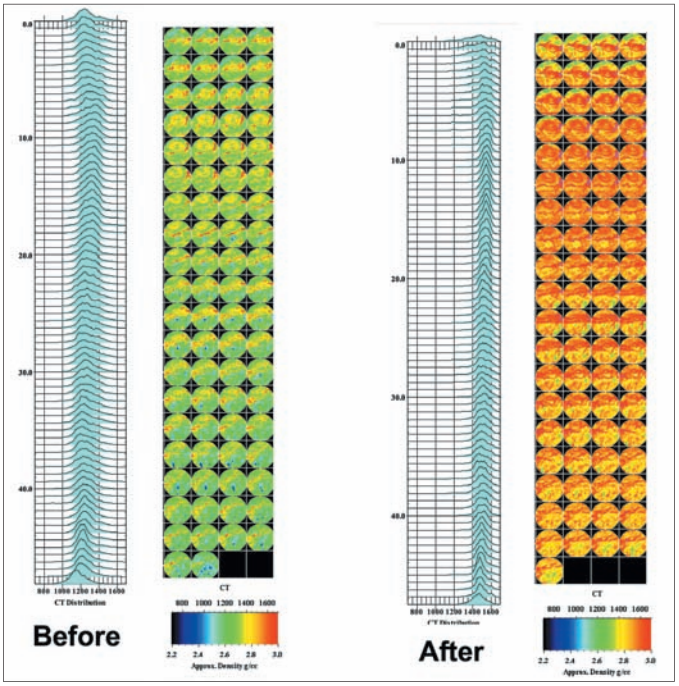

Fig. 10. CT scan of core plug 2 before (left), and after (right) coreflood testing.

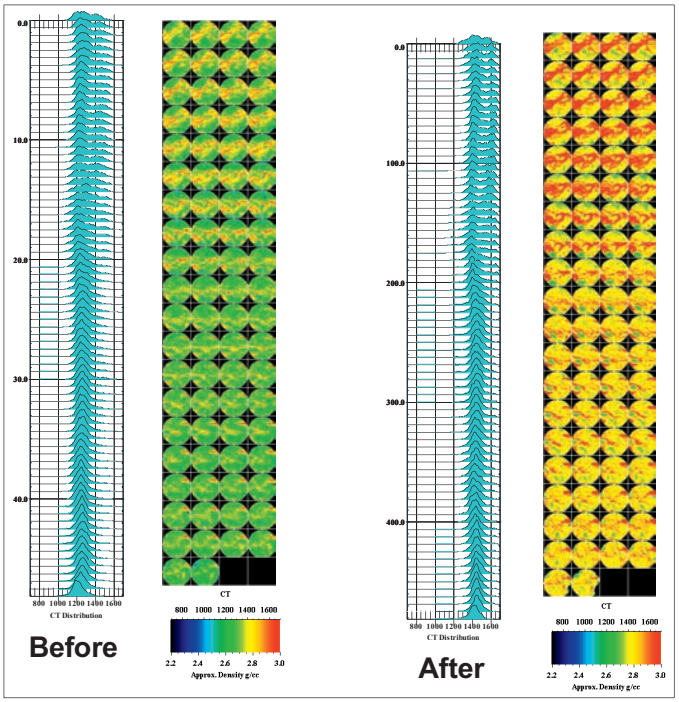

Fig. 11. CT scan of core plug 3 before (left), and after (right) coreflood testing.

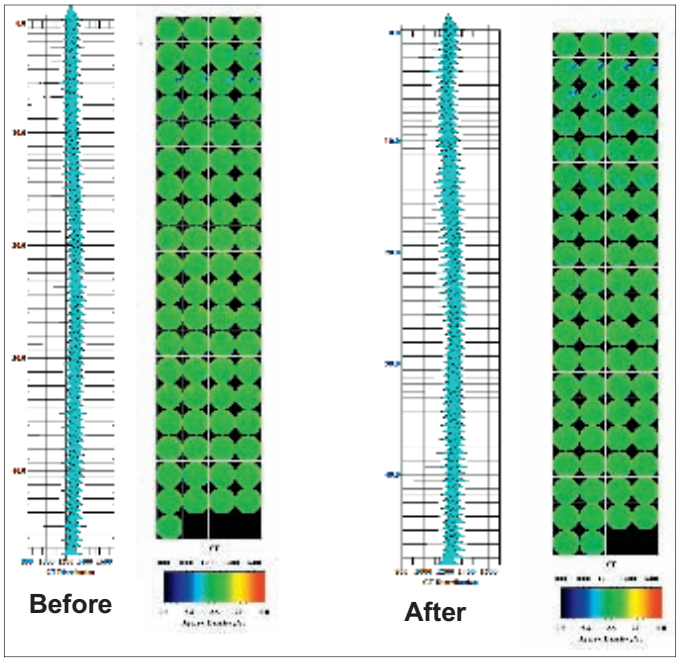

Fig. 12. CT scan of core plug 1 before (left), and after (right) coreflood testing.

CONCLUSIONS

Characterization of two types of sludges that contain both inorganic and organic components were investigated using various techniques. The solubility of the type 2 sludge was assessed using acid and mutual solvents. The acid-rock interactions were assessed using coreflooding and CT scan testing, using core plugs representing highly permeable and heterogeneous sandstone stringers. Based on the experimental studies, the following conclusions can be made:

- Two types of sludge were determined using high resolution pyrolysis methods, XRD, and organic petrology.
- The first sludge type is characterized by a black color, vitreous luster, and conchoidal fractures. It contains solid bitumen and coal fragments as well as carbonate and silicate minerals. The solid bitumen absorbs the OBM, leading the bit to abort drilling. Therefore, water-based mud is highly recommended.
- The second sludge type is saturated sediments with relatively heavy oil at variable asphaltene contents. This corresponds to different degrees of incompatibility between the reservoir oil and the OBM.
- The type 2 sludge samples showed slight solubility in both mutual solvents and xylene at 160 °F, i.e., 5 wt% to 19 wt%, indicating the presence of a large amount of inorganic compounds.
- The dissolution of the type 2 sludge samples in formic acid was higher than acetic acid at 10 wt% and 160 °F, i.e., 34 wt% to 55 wt%. Both acids were mixed with either an ether-based mutual solvent or microemulsion solvent at 10 vol%.

- The microemulsifying surfactant showed no advantage in dissolving the type 2 sludge samples over the mutual solvent when mixed with formic acids. Therefore, utilizing a mutual solvent in field treatment would be sufficient and cost-effective.
- The highest solubility values were obtained with mixtures of 5 wt% HCl acid and solvents, showing solubilities between 79 wt% to 88 wt%.
- The solubility of the type 2 sludge samples — 1 to 6 — in only 5 wt% HCl acid showed inconsistent results, i.e., 25 wt% to 71 wt%, indicating that the presence of a mutual solvent in the acid mixture is essential to maximize the dissolutions of these sludge samples.
- The coreflood experiments utilizing HCl acid and formic acid mixtures showed a slight reduction in permeability — 20%.
- The permeability of the core plugs were reduced slightly following injection of 3 PV of the 0.4 vol% cationic polymeric clay stabilizer, indicating the clay stabilizer coated minerals in the core plug.
- Injection of HCl acid and formic acid mixtures or 10 wt% formic acid in the presence of the 0.4 vol% clay stabilizer showed a slight reduction in permeability by 5% to 13%.
- Although the coreflood experiments showed a slight reduction in permeability, the CT scan results obtained showed a significant increase in rock density along the core length for core plugs 2 and 3, indicating the occurrence of chemical reactions with rock minerals that had an insignificant impact in the core's permeability.

ACKNOWLEDGMENTS

The authors would like to thank the management of Saudi Aramco for their support and permission to publish this article. The authors would also like to acknowledge Sinan Caliskan, Shouwen Shen, Sajjad Al-Darweesh, and Mohammed Al-Ghamdi for conducting some of the experiments discussed in this article.

This article was presented at the IADC/SPE Asia Pacific Drilling Technology Conference, Bangkok, Thailand, August 27-29, 2018.

REFERENCES

1. Al Moajil, A.M., Al-Khaldi, M., Hazzazi, H. and Caliskan, S.: "Acidizing Highly Permeable Sandstone Stringers: Drill-in Fluid Damage and Compatibility with Rock Minerals," SPE paper 191172, presented at the SPE Trinidad and Tobago Section Energy Resources Conference, Port of Spain, Trinidad and Tobago, June 25-27, 2018.
2. Fink, J.K.: "Chapter 9, Filter Cake Removal," in *Petroleum Engineer's Guide to Oil Field Chemicals and Fluids*, pp. 295-309, Boston: Gulf Professional Publishing, 2012, 808 p.
3. Jacobs, I.C.: "Chemical Systems for the Control of Asphaltene Sludge during Oil Well Acidizing Treatments," SPE paper 18475, presented at the SPE International Symposium on Oil Field Chemistry, Houston, Texas, February 8-10, 1989.
4. Bustin, R.M.: *Coal Petrology: Its Principles, Methods, and Applications*, 2nd edition, Victoria, Canada: Geological Association of Canada, 1985, 230 p.
5. Taylor, G.H. and Glick, D.C.: *Organic Petrology: A New Handbook Incorporating Some Revised Parts of Stach's Textbook of Coal Petrology*, 4th edition, Berlin: Gebrüder Borntraeger, 1998, 704 p.
6. Sachse, V.F., Littke, R., Jabour, H., Schumann, T., et al.: "Late Cretaceous (Late Turonian, Coniacian and Santonian) Petroleum Source Rocks as Part of an OAE, Tarfaya Basin, Morocco," *Marine and Petroleum Geology*, Vol. 29, Issue 1, January 2012, pp. 35-49.
7. Crelling, J.C. and Rimmer, S.M.: *Crelling's Petrographic Atlas of Coals and Carbons*, Southern Illinois University Carbondale Department of Geology, 2015, *https://coaland-carbonatlas.siu.edu*.

BIOGRAPHIES

Dr. Bandar I. Ghassal is currently the Supervisor of the Geochemistry Unit of Saudi Aramco's Exploration and Petroleum Engineering Center – Advanced Research Center (EXPEC ARC). He has more than 12 years of experience in the field of petroleum geochemistry in Saudi Aramco.

Bandar has published several papers and conference abstracts on petroleum geochemistry, and the playnology of various North African and Arabian basins.

He received his M.S. degree in Geology from the University of Utah, Salt Lake City, UT, and his Ph.D. degree in Petroleum Geochemistry from the RWTH Aachen University, Aachen, Germany.

Dr. Abdullah M. Al Moajil is a Research Scientist working in the Formation Damage and Stimulation Division of Saudi Aramco's Exploration and Petroleum Engineering Center – Advanced Research Center (EXPEC ARC). Since joining Saudi Aramco in 2006, he has contributed to the design of over 100 successful acidizing and damage removal treatments.

Abdullah's research interests include formation damage, filter cake characterization and removal, carbonate/sandstone acidizing, fracturing fluids and proppants, retarded acid systems, dispersants and surfactants in drilling and production operations, sludge characterization and remediation in oil wells, completion fluids, solvents for asphaltene, surface and interfacial properties, fluid rheology, and chemical interactions with swelling elastomers.

He has published over 38 publications, including proceeding papers, journal articles, and patents. Abdullah has presented over 45 technical papers in international conferences.

He received his B.S. degree in Chemical Engineering from the King Fahd University of Petroleum and Minerals (KFUPM), Dhahran, Saudi Arabia. Abdullah received both his M.S. and Ph.D. degrees in Petroleum Engineering from Texas A&M University, College Station, TX. His M.S. and Ph.D. research focused on manganese tetroxide's water and oil-based fluid's characterization, dissolution, retardation, and the particle dispersion and aggregation processes.

Dr. Sami Abdelbagi is a retired Saudi Aramco Senior Consultant Geochemist who had worked in the Exploration and Petroleum Engineering Center – Advanced Research Center (EXPEC ARC). During his time with Saudi Aramco, Sami provided critical leadership in the application of advanced source rock and reservoir geochemical techniques to exploration, development and production problems. Prior to joining Saudi Aramco, he held positions with Texaco, and the General Petroleum Corporation of Sudan.

Sami received his B.S. degree from the University of Khartoum, Khartoum, Sudan, his M.S. degree from the University of Pittsburgh, Pittsburgh, PA, and his Ph.D. degree from Southern Illinois University, Carbondale, IL.

Abdullah A. Al-Rustum is a Laboratory Technician with the Formation Damage and Stimulation Unit of Saudi Aramco's Exploration and Petroleum Engineering Center – Advanced Research Center (EXPEC ARC).

He is the coauthor of more than 10 published papers in various oil and gas journals.

Abdullah joined Saudi Aramco in 2009 and graduated from the Industrial Training Center in 2011. He received his B.S. degree in Information Technology from the Saudi Electronic University, Riyadh, Saudi Arabia.

Experimental Verification of a New Approach to Long-Range EM Imaging

Dr. Howard K. Schmidt, Jesus M. Felix Servin, and Dr. Erika S. Ellis

ABSTRACT

Proximity sensing was recently proposed as a way to simultaneously increase both range and resolution in cross-well electromagnetic (EM) tomography. The approach is applicable to reservoirs with resistive seals. Earlier reports were based on finite element models of layered structures, with dielectric and conductivity contrasts matching those of known reservoirs.

Experimental work, now reported, is consistent with expectations based on finite element model simulations. Synthetic layered structures have been investigated using a 1.3 GHz ground penetrating radar (GPR) system. A scaled reservoir model was constructed in a 1 m tank comprising sand filled with fluids of variable dielectric constant and conductivity. In this system, dry sand, brine saturated sand, and a polymer foam, provide a useful mimic for the electrical properties expected for a carbonate reservoir sealed by anhydrite. Data was recorded in the time domain using EM transients. Observed trends in velocities and amplitude shifts were consistent with finite element models. Interestingly, polarization dependent signal transport first indicated by finite element modeling was supported by these experimental results.

Results to date indicate that greatly increased EM propagation can be achieved through resistive geologic layers, rather than directly through relatively conductive reservoir media. We confirm that these layers act as planar transmission lines and not as waveguides — meaning that there is no hard lower cutoff frequency, and longer wavelengths can be used to sense and characterize reservoir fluids proximal to the dielectric channel. The results also confirm that variations in bounding layers modulate the amplitude and velocity of the signal in the dielectric channel, and thereby demonstrate the concept of proximity sensing.

These results support a new technical direction for EM characterization of reservoirs, especially in conjunction with magnetic contrast agents, enabling efficient localization of bypassed oil, and mapping the remaining oil columns in mature reservoirs.

INTRODUCTION

Long-term petroleum reservoir management ideally optimizes production of oil while avoiding brine production, and minimizing well count and complexity. Given imperfect knowledge of reservoir structures, significant inhomogeneity, and dynamic multiphase fluid saturation, this is a difficult and long-standing problem that would greatly reward improved methods for observing the state and structure of the reservoir in near real-time. This is particularly true in the case of mature fields in secondary production on waterflood. Modern reservoir models derived from 3D seismic, well logs, and history matching are certainly a vital tool for reservoir management.

Our lack of knowledge about large-scale inhomogeneity, including facture corridors, prevent anticipation of early water breakthrough and bypass of significant volumes of oil. As such, there is a great need for imaging tools that can locate flood fronts, detect bodies of bypassed oil, and map the remaining oil column thickness across the entire reservoir with sufficient resolution to guide key management decisions. Naturally, reservoir management would be easy if we had imaging modalities with petrophysical scale resolution, e.g., well logs ~0.1 m, over the available geophysical survey scales, e.g., seismic ~kilometers (km). Imaging resolution requirements that can yield valuable and actionable information is probably much less challenging than that, and depends on the direction and scale of the particular field under consideration.

For the purposes of this article, we will assert that for giant and super-giant fields (> 1 billion bbl), imaging modalities with resolution on the order of 1 m vertically, and up to several hundred meters laterally, could respectively determine the remaining oil column and flooded/bypassed volumes with sufficient accuracy to greatly improve reservoir management practice and development planning. Historic approaches for generating this kind of actionable information include direct full volume imaging using acoustic and low frequency electromagnetic (EM) probes. A new approach based on indirect EM imaging via proximity sensing will be experimentally described here.

BACKGROUND

The main reservoir imaging approaches currently in use include seismic and EM means. 4D seismic has been gainfully employed to monitor waterfloods in clastic fields worldwide[1-4], although results have been unsatisfactory in carbonate reservoirs, due to the low acoustic impedance contrast between light petroleum and brine filled carbonate matrices[5]. EM approaches have recently appeared effective for monitoring carbonate reservoirs. Specific EM methods gainfully applied to "giant" class carbonate reservoirs include borehole to surface-induced polarization[6-8], surface to borehole EM[9], and cross-well EM[10]. The frequencies used are around 1 Hz, 10 Hz, and 100 Hz, respectively, resulting in probes with wavelengths on the order of 10^6 m.

Such low frequencies have been considered *de rigueur* for the diffusive regimen, in lossy media like deep sedimentary strata to enable penetration up to the km scale — a typical reservoir depth and interwell spacing in giant fields. As expected, the natural imaging power of such long wavelengths is poor. Even so, predecessor EM technologies like magnetotellurics[11] and controlled source EM[12] surveys that operate at still lower frequencies (< 1 Hz) yield actionable information detecting large-scale structures in exploration.

Useful reservoir images, along lateral dimensions at least, are obtained by tomographic means employing closely spaced observation points along the surface and boreholes. Similar to spreading resistance measurements[13] and gravity surveys[14], imaging resolution depends on the spacing of sampling points and decreases with depth into the material. The detectable feature size scales linearly with the distance from the survey locus while the maximum resolution equals the spatial sampling spacing in the vicinity of the survey locus. Effective resolution in cross-well EM with km borehole spacing is therefore on the order of a few hundred meters — and only in the plane of the survey. Apparent resolution with 3D features has been achieved recently by joint inversion methods constrained by geologic models derived from a combination of seismic, well log, and production history matching[15]. All of these methods employ fairly low power continuous wave EM sources and are generally slow and expensive, especially for horizontal wells where coiled tubing conveyance is required.

Plainly, some alternative EM approaches with a higher intrinsic resolution would be desirable. Indeed, an obscure technology, radio imaging (RIM)[16], has been used in mining applications since the 1970s. RIM uses much higher frequencies — around 1 MHz. The technique is gainfully used for mapping obstructions in coal mines and locating metal sulfide ore bodies in hard rock mines. In both cases, the detection challenge is mapping conductive targets in relatively resistive matrices of 10^3 ohm-meters or higher. RIM has proven successful in situations where the resistive matrix was bounded by relatively conductive strata, and the authors found that the matrix channeled radio frequency as a waveguide when the wavelength, λ, was around twice the layer thickness.

As part of our magnetic nanomappers program[17], we recently proposed a similar detection scheme, proximity sensing, with potential application in certain reservoirs fortuitously sealed by highly resistive materials, e.g., anhydrite. The method may also apply to other evaporites — halite and gypsum — and certain resistive carbonates, e.g., chalk and dolomite. Our method exploits the observation that the lower bounding layer — the petroleum filled porous reservoir — is only somewhat conductive, and is an imperfect bounding layer that will allow a traveling wave to "sample" the reservoir to present, in combination with the resistive channel, an effective medium that modulates the transport properties of the channel, i.e., velocity, amplitude and dispersion, in a way that depends on the fluid saturations in the reservoir.

The concept was successfully simulated numerically with 2D[18] and 3D[19] models. The present work describes a physical demonstration using a 1 m scale model reservoir probed in transmission mode using a 1.3 GHz ground penetrating radar (GPR) system.

EXPERIMENTAL

The reservoir model, Fig. 1, was fabricated from a polyethylene intermediate bulk container tote tank measuring 1.15 m × 0.95 m × 1.0 m in width, length, and height, respectively. The main matrix consisted of washed medium sand — 10 mesh to 40 mesh. To mimic a brine saturated reservoir, sand was saturated with sodium chloride at 50 g/l (50 kppm) dissolved in water; some 35 vol% of brine was required to saturate the sand matrix. In some experiments, dry sand was used to mimic a hydrocarbon reservoir matrix. A number (two to five) of 5 cm thick slabs of closed cell polystyrene foam were

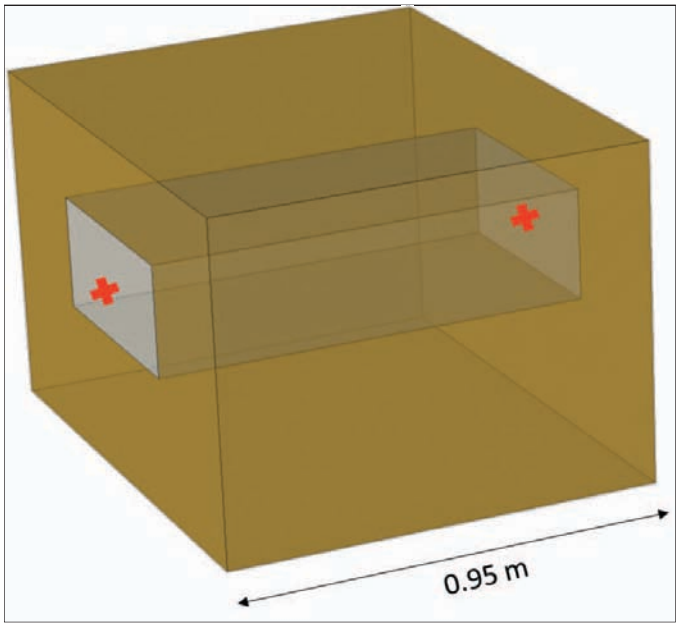

Fig. 1. Initial model built for lab testing. It includes a channel of polystyrene surrounded by wet sand. The location of the transmitter and receiver is marked by a red cross.

Material	ϵ_r	μ_r	σ S/m
Wet Sand	14	1	~1
Dry Sand	~4	1	> 10^{-4}
Foam	1.2	1	> 10^{-4}

Table 1. EM properties of materials comprising the reservoir model

used to mimic anhydrite as the EM channel with various thicknesses — 10 cm to 25 cm. The EM channel was 60 cm wide in all experiments and extended the full length of the reservoir tank — 95 cm. EM transients were recorded with a MALA ProEx GPR system using a pair (transmitter (Tx) and receiver (Rx)) of shielded separable microwave antennas. Each antenna includes a Wu-King Bow-Tie dipole antenna that yields an overdamped two-cycle transient with a fundamental frequency of 1.3 GHz — wavelength ~23 cm in free space.

The emitted frequency is polarized and propagates as transverse EM radiation. Transients were recorded at 10 Hz using a 20 GHz sampling frequency and 64 stacks; 10 seconds of data were recorded at each station, and the ensemble was averaged to optimize the signal-to-noise ratio before picking arrival times. In this model system, the signal will propagate faster through the foam than the surrounding sand, due to the EM properties of each material, Table 1.

Two main experiments were performed, and different data sets for each were obtained with the electric field oriented perpendicular or parallel to the plane of the EM channel. The first experiment varied the channel thickness, *t*, to study the effect of the *t*/λ ratio. In the second, 2D tomograms (9 cm × 9 cm on 10 cm centers) were obtained across the channel with left and right halves of the channel bounded by brine saturated sand, and dry sand, respectively, to directly observe the proximity sensing effect, if any, and demonstrate the mapping of the EM properties of the medium adjacent to the EM channel. Three different channel thicknesses were used: 10 cm, 15 cm, and 20 cm. Tomograms were inverted from 81 individual transients using bh_tomo[20]. In all experiments, arrival times for each transient were picked by hand.

RESULTS AND DISCUSSION

Effect of Channel Thickness

In the first experiment, the channel thickness was varied from 5 cm to 25 cm in 5 cm steps, to investigate the effect on signal amplitude, and the speed of propagation. The (Tx) and (Rx) were located at the center of the channel on either side of the model, as previously shown in Fig. 1. Figures 2 and 3 show the traveltime through the channel for vertical and horizontal polarization, respectively. Since the channel has a dielectric constant of 1.2, the 1.3 GHz probe has a wavelength of ~21 cm, and should have a velocity of ~3.3 nS/m. This indeed is just the observed velocity in channels comparable to that

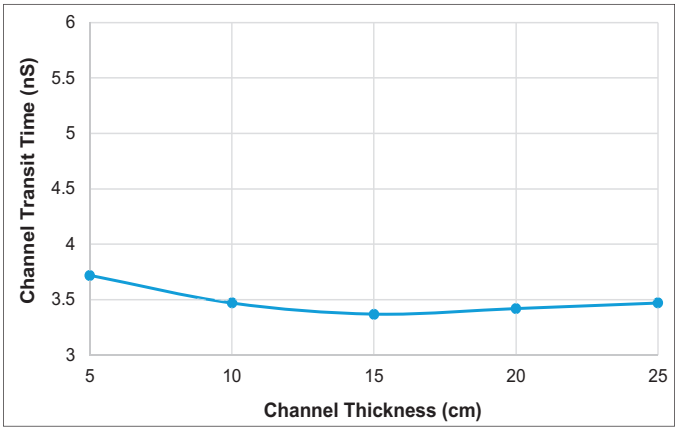

Fig. 2. Traveltime as a function of channel thickness with the E-field oriented vertically.

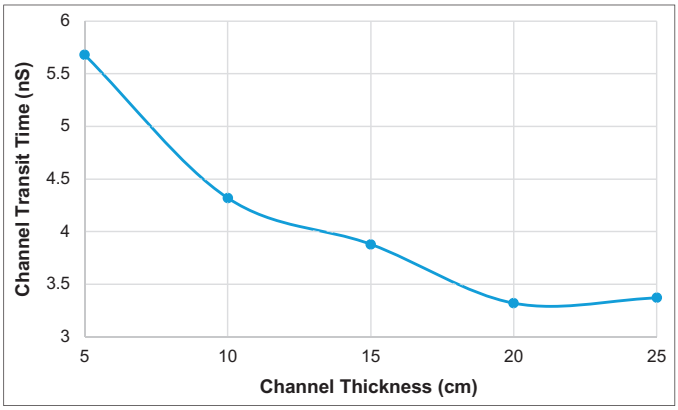

Fig. 3. Traveltime as a function of channel thickness with the E-field oriented horizontally.

wavelength or greater, regardless of the polarization. Interestingly, the transit time increases — velocity decreases — when the channel thickness is less than the wavelength for both polarizations. In the vertical case, the signal is slowed by about 10% when the channel is less than about λ/2 (10 cm). At λ/2, the channel is equivalent to a waveguide with nodes at each wall, but at λ/4 (5 cm), the wave is "forced" to sample the bounding medium.

Consistent with our original hypothesis, the leaky boundary with a higher dielectric constant retards the wave and increases transit time. The modest effect could indicate that the electric field does not readily penetrate the relatively conductive bounding medium, the brine filled sand. The retardation is profound for the horizontally polarized signal — around a 60% increase in transit time with a λ/4 channel thickness. When the electric field is horizontal, the perpendicular magnetic component of the transverse EM wave is forced, and indeed able, to enter and penetrate the conducive bounding medium. This fascinating and unexpected result is reminiscent of birefringence of light in calcite crystals, which is due to a varying velocity, depending on the polarization alignment with key crystal axes.

According to our hypothesis, by using a waveguide to propagate EM signals with the λ comparable to channel thickness, the energy will be contained within the channel

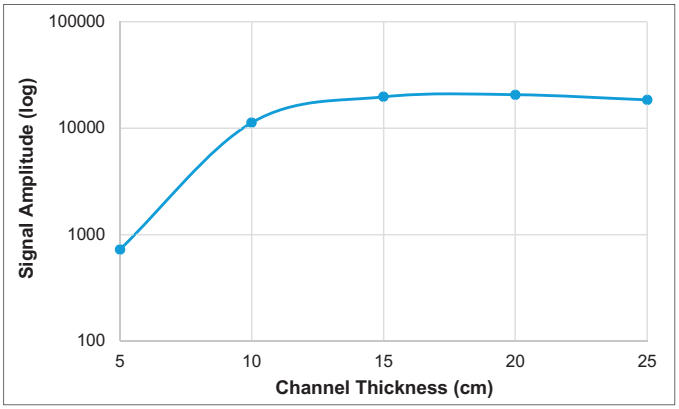

Fig. 4. Peak-to-peak amplitude as a function of channel thickness with the E-field oriented vertically.

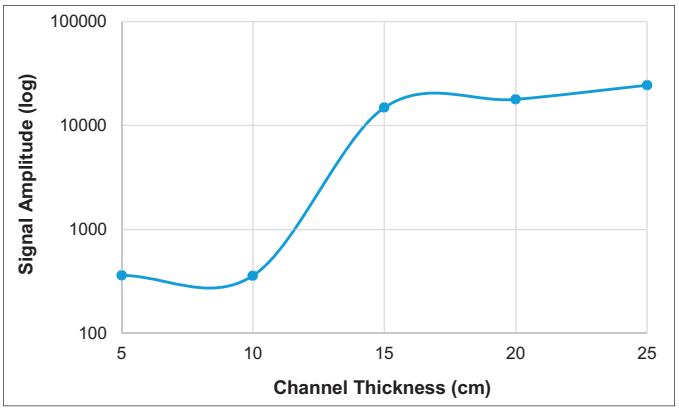

Fig. 5. Peak-to-peak amplitude as a function of channel thickness with the E-field oriented horizontally.

and attenuation will be lower than when forced to sample the higher conductivity reservoir by thinner channels. To test this claim, the maximum peak-to-peak amplitude of the signal was measured for each of the channel thicknesses (5 cm, 10 cm, 15 cm, 20 cm, and 25 cm); the results for vertical and horizontal polarization are shown in Figs. 4 and 5, respectively.

In the vertical case, the signal amplitude is essentially constant for a channel thickness of λ/2 (10 cm) or greater — similar to the velocity previously mentioned — and consistent with waveguide behavior. At λ/4 (5 cm), the signal amplitude drops by roughly a factor of 20. Plainly, when the channel has to function as a leaky planar transmission line, the conductive bounding layer attenuates the probe signal. It is worthwhile to note that had the thin channel functioned solely as a waveguide at λ/4 — half the cutoff frequency — expected attenuation would have been hundreds of orders of magnitude[21]. The effect is also true for the horizontal polarization, although the observed attenuation is roughly a factor of 5 for the λ/4 case, and significant losses are incurred for any channel thickness less than the λ. Our original hypotheses of transmission line behavior and proximity sensing is confirmed by these simple observations.

These results suggest that there is a significant practical tradeoff between sensitivity and attenuation — as a function of the ratio of channel thickness to probe wavelength. Frequencies that result in wavelengths larger than the channel thickness will provide more information about the surrounding signals, but at the cost of higher attenuation and reduced range. This implies that a practical system should have a tunable frequency, and hopefully controllable polarization to optimize the range while controlling sensitivity, and perhaps the depth of investigation into the reservoir.

Tomography via Proximity Sensing

Our hypothesis also claims that changes in fluid saturation and their specific EM properties in the reservoirs adjacent to the channel will modulate the transported signal in either traveltime or amplitude, or both. To test this claim, the initial lab model was modified such that half of the channel was covered with a layer of dry sand, Fig. 6. As before, multiple layers of foam were used to vary the height of the channel to include 10 cm, 15 cm, and 20 cm. If our approach is sensitive to saturation changes in adjacent layers, we should see a difference in traveltime through the channel between wet sand and dry sand. For each channel thickness, 81 waveforms were recorded by placing the Tx and the Rx in nine different positions each, in a tomographic manner, Fig. 7.

Arrival times were picked manually and inversion was done using the least squares approach in bh_tomo for each different channel thickness. The output is a 2D velocity map

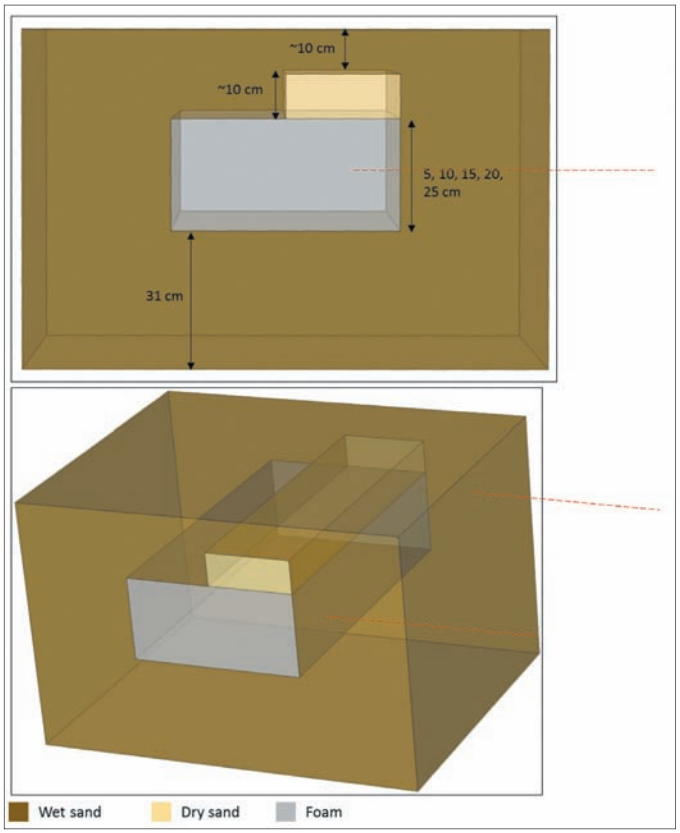

Fig. 6. Cross-section along the depth of the lab scale model (top), showing that half of the channel is covered with a layer of dry sand. The bottom image is a 3D perspective. The red lines represent the line along which the Rx and Tx were moved.

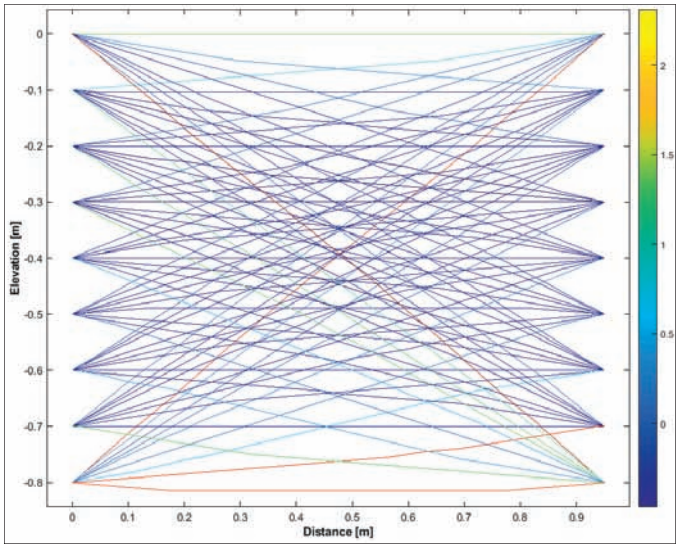

Fig. 7. Ray coverage from the 81 recorded waveforms. The left edge corresponds to the Rx side, and the signal propagates right to left.

of the plane formed by the Rx and the Tx acquisition lines. The inverted data presented corresponds to the region around the foam channel. Figures 8, 9, and 10, respectively, show the resulting velocity tomograms for channel thicknesses of 10 cm, 15 cm, and 20 cm, using horizontal polarization. Each image clearly shows an upper high velocity region (red), and a lower low velocity region (blue).

Overall, velocities increase with increasing channel thickness, where the signal can primarily propagate through the low loss, and low dielectric constant foam. Interestingly, the upper region, corresponding to a 10 cm slab of dry sand is faster than the narrower channel bounded by lossy high dielectric constant brine filled sand. We also observe that the slow region appears to be consistently smaller in size than the upper half bounded by dry sand. This is perhaps an artifact of the simple (and fast) ray tracing algorithm used by bh_tomo to invert the arrival time data. From above, the signal through the 10 cm channel may be significantly attenuated compared to the signal through the region bounded by dry sand. Signal competition along with "short cut" paths through the faster region could mask part of the slow region. This could be refined with a full wave inversion algorithm, albeit with significantly greater computational effort.

Tomographic results were similar for vertically polarized probes, and a bit faster, as expected from the simple channel measurements. Clearly, these tomographic results show that the EM properties of the medium bounding of a low loss channel modulate the primary probe signal, and can be exploited to map those properties. In practice, this appears to allow the development of a scheme to detect and map fluid saturations over substantial areas in reservoirs sealed by low loss materials, i.e., anhydrite.

As noted in the simple transport measurements in the first experiment, the proximity effect of brine filled matrix (slow and lossy) on velocity is profoundly different for vertical and

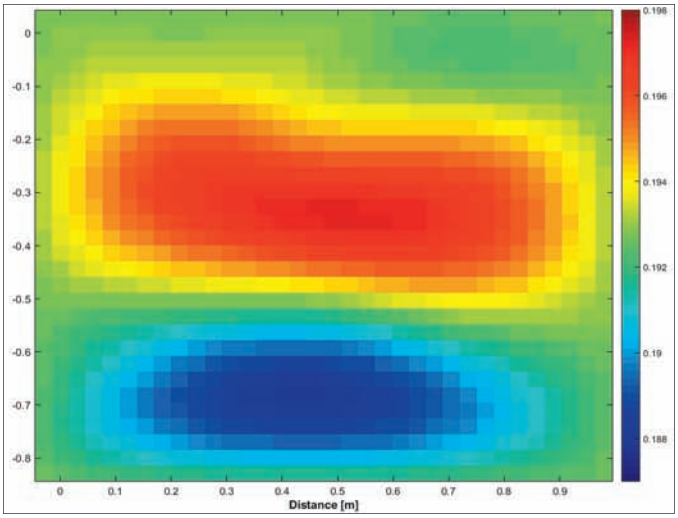

Fig. 8. The 10 cm channel inverted data. The left edge of the inversion corresponds to the Rx face of the model. The two contrasting regions correspond to wet sand (high velocity red region) and dry sand (low velocity blue region) above the channel.

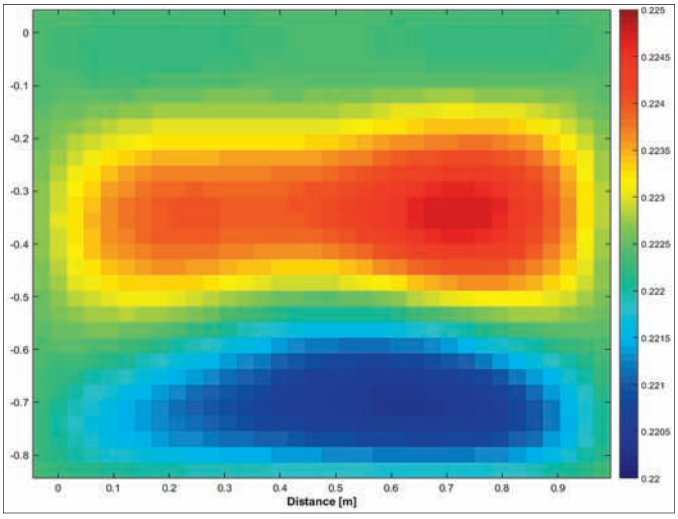

Fig. 9. The 15 cm channel inverted data. The left edge of the inversion corresponds to the Rx face of the model. The two contrasting regions correspond to wet sand (high velocity red region) and dry sand (low velocity blue region) above the channel.

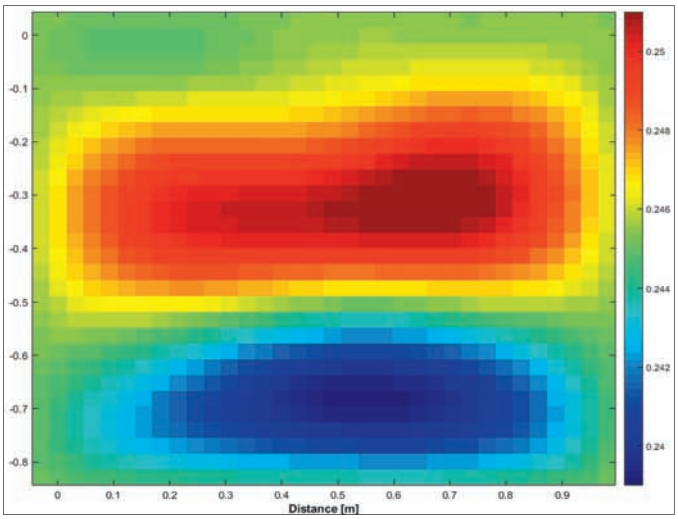

Fig. 10. The 20 cm channel inverted data. The left edge of the inversion corresponds to the Rx face of the model. The two contrasting regions correspond to wet sand (high velocity red region) and dry sand (low velocity blue region) above the channel.

horizontal polarized signals. This is almost certainly due to the ability of brine to screen the electric field component of transverse EM probes (vertical), while allowing greater penetration of the magnetic component in horizontally polarized probes. Considering our original motivation to develop a scheme for detecting magnetic nanomapper fluids, we can anticipate that such magnetic fluids would screen magnetic fields effectively. This, we think, would provide a means to distinguish and map previously injected nonmagnetic waterflood fluids compared to magnetic nanomapper loaded fluids that might be injected in the future. This could perhaps be performed with exquisite sensitivity and determined directly without the need for before and after imaging surveys. This will be explored experimentally at the laboratory scale in a future work.

Finally, we can consider the potential range and resolutions that might be achievable in reservoir management using this new proximity sensing technique. From the current experimental results, we can see that the channel efficiently transports signals with a wavelength approximately equal to its thickness. Doubling the wavelength, relative to the channel thickness, forces the probe signal to sample the material proximal to the channel — modulating the speed by a factor of two, and amplitude by a factor of 10.

Assuming we can easily measure speed and amplitude in a cross-well imaging survey with an accuracy of 5%, it seems reasonable to expect that we can determine changes in key EM properties of the bounding layer, e.g., σ, ε, and μ, with similar accuracy and perhaps thickness to within $\lambda/20$. A petroleum reservoir sealed with a 30 m layer of anhydrite could therefore potentially be mapped with a resolution of 30 m in the horizontal plane, and about 1.5 m vertically. This is sufficient for our original target requirement for actionable information to guide reservoir management and development planning. The question of range will have to await field tests for a definitive answer.

In the meantime, we can perhaps extrapolate from the RIM experience in coal mines. Fortuitously, the analogy is well founded, since the EM properties of anthracite are almost identical to that of anhydrite ($\varepsilon_r \approx 4$ and $\sigma \approx 10^{-4}$ Ωm). A key RIM paper[16] reported a range of 300 m through a 2 m thick coal seam using a resonant mode probe at ≈ 1 MHz. Since wavelength will scale with channel thickness and attenuation scales inversely with wavelength, we could potentially achieve ranges 10× greater, around 3 km, through a 30 m thick channel. Giant and super-giant carbonate petroleum reservoirs with anhydrite seals matching these specifications are well-known.

CONCLUSIONS

A meter scale reservoir model was constructed and probed with a GPR system to experimentally confirm earlier simulations of the proximity sensing concept. The experimental results were consistent with the trends observed in previous numerical simulations. The results clearly demonstrate that the method is sensitive to changes in fluid saturation — wet sand vs. dry sand. We expect that this approach will be sensitive enough to distinguish oil saturated regions from brine saturated regions in petroleum reservoirs. The measurements also proved that there is a tradeoff between attenuation and sensitivity.

Generally speaking, lower frequencies will result in greater sensitivity, but increased attenuation, which is counter to what is normally observed when propagating through the reservoir rather than a waveguide. Therefore, frequency will be a key design parameter for future field testing and should be chosen such that the wavelength is comparable to the thickness of the channel being used to propagate the signal. Simple ray tracing tomographic inversion based on arrival times suffice for imaging variations in EM properties of bounding layers. Full wave inversion methods are likely to improve imaging accuracy while providing additional structural details within slower regions.

Proximity sensing is a new approach to address the challenge of long-range EM propagation in the reservoir, in the presence of conductive media. The proposed method relies on the use of naturally occurring waveguides in the form of a thick layer of sealing evaporate — anhydrite — bounded porous petroleum reservoirs. When deployed at a field scale, this approach could provide improved inter-well reservoir saturation information with unprecedented range and resolution. Future experimental work will include quantitative measurements of proximity modulation due to the variation in thickness, conductivity, dielectric constant, and magnetic permeability of the bounding layers.

ACKNOWLEDGMENTS

The authors would like to thank the management of Saudi Aramco for their support and permission to publish this article.

This article was presented at the SPE Kingdom of Saudi Arabia Annual Technical Symposium and Exhibition, Dammam, Saudi Arabia, April 23-26, 2018.

REFERENCES

1. Pathak, R.K. and Bakar, R.: "Estimating Saturation Changes from 4D Seismic: A Case Study from Malay Basin," IPTC abstract 16910, presented at the International Petroleum Technology Conference, Beijing, China, March 26-28, 2013.
2. Tolstukhin, E., Lyngnes, B. and Sudan, H.H.: "Ekofisk 4D Seismic — Seismic History Matching Workflow," SPE paper 154347, presented at the SPE EUROPEC/EAGE Annual Conference, Copenhagen, Denmark, June 4-7, 2012.

3. Kelamis, P.G., Uden, R.C. and Dunderdale, I.: "4D Seismic Aspects of Reservoir Management," OTC paper 8293, presented at the Offshore Technology Conference, Houston, Texas, May 5-8, 1997.
4. Denney, D.: "Saturation Mapping from 4D Seismic Data in the Statfjord Field," *Journal of Petroleum Technology*, Vol. 52, Issue 11, November 2000, pp. 38-40.
5. Marvillet, C., Al-Mehairi, Y.S., Shuaib, M., Al-Shaikh, A., et al.: "Seismic Monitoring Feasibility on Bu-Hasa Field," IPTC paper 11640, presented at the International Petroleum Technology Conference, Dubai, UAE, December 4-6, 2007.
6. Aziz, A.A., Strack, K. and Hanstein, T.: "Surface-to-Borehole TEM for Reservoir Monitoring," paper presented at the SEG Annual Meeting, San Antonio, Texas, September 18-23, 2011.
7. Marsala, A.F., Buali, M., Al-Ali, Z.A., Shouxiang, M.M., et al.: "First Borehole to Surface Electromagnetic Survey in KSA: Reservoir Mapping and Monitoring at a New Scale," SPE paper 146348, presented at the SPE Annual Technical Conference and Exhibition, Denver, Colorado, October 30-November 2, 2011.
8. Marsala, A.F., Lyngra, S., Widjaja, D.R., Laota, A.S., et al.: "Fluid Distribution Inter-Well Mapping in Multiple Reservoirs by Innovative Borehole to Surface Electromagnetic: Survey Design and Field Acquisition," IPTC paper 17045, presented at the International Petroleum Technology Conference, Beijing, China, March 26-28, 2013.
9. Colombo, D., McNeice, G. and Kramer, G.: "Sensitivity Analysis of 3D Surface-Borehole CSEM for a Saudi Arabian Carbonate Reservoir," *SEG Technical Program Expanded Abstracts 2012*, November 2012, pp. 1-5.
10. Marsala, A.F., Al-Ruwaili, S.B., Sanni, M.L., Shouxiang, M.M., et al.: "Crosswell Electromagnetic Tomography in Haradh Field: Modeling to Measurements," SPE paper 110528, presented at the SPE Annual Technical Conference and Exhibition, Anaheim, California, November 11-14, 2007.
11. Nichols, E.A., Morrison, H.F. and Clarke, J.: "Signals and Noise in Magnetotellurics," SEG paper 1985-0259, presented at the Society of Exploration Geophysicists Annual Meeting, Washington, D.C., October 6-10, 1985.
12. Constable, S. and Srnka, L.J.: "An Introduction to Marine Controlled-Source Electromagnetic Methods for Hydrocarbon Exploration," *Geophysics*, Vol. 72, Issue 2, March-April 2007, pp. WA3-WA12.
13. Gramse, G., Kölker, A., Lim, T., Stock, T.J.Z., et al.: "Nondestructive Imaging of Atomically Thin Nanostructures Buried in Silicon," *Science Advances*, Vol. 3, Issue 6, June 2017.
14. Styles, P., McGrath, R., Thomas, E. and Cassidy, N.J.: "The Use of Microgravity for Cavity Characterization in Karstic Terrains," *Quarterly Journal of Engineering Geology and Hydrogeology*, Vol. 38, Issue 2, May 2005, pp. 155-169.
15. Marsala, A.F., Lyngra, S., Safdar, M., Zhang, P., et al.: "Crosswell Electromagnetic Induction between Two Widely Spaced Horizontal Wells: Coiled Tubing Conveyed Data Collection and 3D Inversion from a Carbonate Reservoir in Saudi Arabia," *SEG Technical Program Expanded Abstracts 2015*, October 2015, pp. 2848-2852.
16. Emslie, A.G. and Lagace, R.L.: "Propagation of Low and Medium Frequency Radio Waves in a Coal Seam," *Radio Science*, Vol. 11, Issue 4, April 1976, pp. 253-261.
17. Al-Shehri, A.A., Ellis, E.S., Felix Servin, J.M., Kosynkin, D.V., et al.: "Illuminating the Reservoir: Magnetic NanoMappers," SPE paper 164461, presented at the SPE Middle East Oil and Gas Show and Conference, Manama, Kingdom of Bahrain, March 10-13, 2013.
18. Felix Servin, J.M., Schmidt, H.K. and Ellis, E.S.: "Improved Saturation Mapping Using Planar Transmission Lines and Magnetic Agents," SPE paper 181343, presented at the SPE Annual Technical Conference and Exhibition, Dubai, UAE, September 26-28, 2016.
19. Felix Servin, J.M., Ellis, E.S. and Schmidt, H.K.: "Proximity Sensing: A Novel Approach to Reservoir Saturation Monitoring Using High Frequency Electromagnetic Pulses," SPE 187282, presented at the SPE Annual Technical Conference and Exhibition, San Antonio, Texas, October 9-11, 2017.
20. Giroux, B., Gloaguen, E. and Chouteau, M.: "bh_tomo — a MatLab Borehole Georadar 2D Tomography Package," *Computers & Geosciences*, Vol. 33, Issue 1, January 2007, pp. 126-137.
21. Yeap, K.H., Tham, C.Y., Yassin, G. and Yeong, K.C.: "Propagation in Lossy Rectangular Waveguides," Chapter 10 in *Electromagnetic Waves Propagation in Complex Matter,* Ahmed Kishk (ed), July 2011, pp. 255-273.

BIOGRAPHIES

Dr. Howard K. Schmidt is a retired Petroleum Engineering Consultant, who had worked with the Reservoir Engineering Technology Team of the Exploration and Petroleum Engineering Center — Advanced Research Center (EXPEC ARC) before retiring in 2018. He led the Magnetic NanoMappers project within the In-Situ Sensing and Intervention (ISSI) focus area. Prior to joining Saudi Aramco, Howard was at Rice University where he served as Senior Research Fellow in the Chemical and Biomolecular Engineering Department and Executive Director of the Carbon Nanotechnology Laboratory. While there, Howard also served as the founding Senior Nanotechnology Adviser to the Advanced Energy Consortium (AEC).

He received his B.S. degree in Electrical Engineering in 1980, and his Ph.D. degree in Chemistry in 1986, both from Rice University, Houston, TX.

Howard has 50 peer-reviewed publications and a dozen issued patents.

Jesus M. Felix Servin joined the Reservoir Engineering Technology Division of Saudi Aramco's Exploration and Petroleum Engineering Center – Advanced Research Center (EXPEC ARC) in February 2012. His focus is on the development of electromagnetic methods and nanoparticle-based contrast agents for reservoir characterization and monitoring. Jesus's role has been instrumental in the development and deployment of the Magnetic Nano-Mappers project, including hardware design and in-house fabrication, instrumentation, computer programming, and data processing.

Jesus' interests include the development of nanoscale strategies for reservoir illumination and electromagnetic methods for reservoir description and monitoring.

He received his B.S. degree in Engineering Physics from Instituto Tecnologico y de Estudios Superiores de Monterrey, Monterrey, Mexico, and an M.S. degree in Chemical and Biological Engineering from King Abdullah University of Science and Technology, Thuwal, Saudi Arabia.

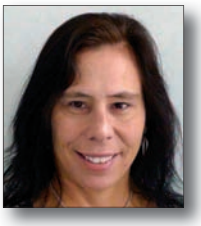

Dr. Erika S. Ellis was a Petroleum Engineer working in Saudi Aramco's Reservoir Engineering Group researching nano and micro electro-mechanical systems (NEMS/MEMS) to help illuminate oil reservoirs. Erika left the company in 2018. Prior to joining the company in 2013, she spent 9 years at the Argonne National Laboratory in Chicago, IL, developing thick-film gas micro-sensors for a variety of applications. Erika spent the last 14 years in R&D in Dallas, TX, developing and characterizing new materials and process integration schemes for MEMS applications for Fortune 500 semiconductor companies.

She received her B.S. degree in Applied Physics from Lewis University, Romeoville, IL, and her M.S. degree in Applied Physics from Northern Illinois University, Dekalb, IL. Erika then received her Ph.D. degree in Materials Science and Engineering from the University of Texas at Arlington, TX.

Wettability Evaluation by Fast Field Cycling NMR Relaxometry

Jun Gao, Dr. Hyung T. Kwak, and Dr. Ahmad M. Al-Harbi

ABSTRACT

Wettability is an essential concept to understand oil trapping due to adhesion and capillary forces, and it depends on the fluid/rock molecular interactions within the thin liquid layer on the pore surface. The conventional methods for wettability determination exploit its macroscopic averaging effects during various displacement processes. These methods are sufficient for general categorization; however, they are not easily used in the wettability alteration study, which is one of the most important oil mobilization mechanisms for a carbonate reservoir. The direct characterization of the microdynamics of liquid molecules on the pore surface would provide not only the measurement of wettability but also the understanding of how added materials affect fluid molecular dynamics and alter the wettability for oil mobilization. This study is to extend the application of the newly developed nuclear magnetic resonance (NMR) technique and fast field cycling (FFC) NMR relaxometry to more fluids and rock samples as the first stage for the above objectives.

Creating an NMR dispersion profile by FFC NMR is a low field magnetic resonance technique, which measures the longitudinal spin relaxation over a wide range of Larmor frequencies determined by magnetic field strength. The dependency of the spin-lattice relaxation rate on the Larmor frequency allows geoscientists to identify the liquid molecular dynamic patterns on the pore surface and determine the respective correlation times. The NMR dispersion affinity or wettability index was obtained from the time scales of the molecular translation and chemical exchange based on the dipolar interactions in the proximity of the paramagnetic spins. Only limited NMR dispersion results of fluid/rock systems and saturation states have been reported. This work utilizes a wide bore FFC NMR relaxometer to obtain NMR dispersion on more fluids and rock samples of different mineralogy, and analyzes their NMR dispersion features with spin relaxation models.

The current study obtains the NMR dispersion curves and qualitative affinity/wettability estimation for different fluid/rock systems, including brine, mineral oil, crude oil, sandstone, limestone, and carbonate reservoir rocks. The dynamic patterns of liquid molecules are evaluated through NMR dispersion features for their adhesive degree on the pore surface. The comparison with the supposed wettability property indicates that they correlate well, and the wettability states are better understood through their molecular dynamics.

The NMR dispersion measurement and interpretation of various fluid/rock systems extend its application; the determination of microdynamic patterns and parameters explains different wettability states from the molecular level. This study set the foundation for its application extended to fluid/rock systems at various saturation states, and wettability alteration monitoring and optimizing during different oil mobilization processes.

INTRODUCTION

Wettability is defined as "the tendency of one fluid to spread on or adhere to a solid surface in the presence of other immiscible fluids"[1]. It determines the spatial distribution of different fluids in the pore space, which affects virtually all rock/fluid properties and processes essential to hydrocarbon mobilization, especially for carbonate reservoirs. The wettability of most carbonate reservoirs is slightly oil-wet, intermediate wet to slightly water-wet[2] and the usual methods such as Amott and USBM methods are not very sensitive to the intermediate wet range. Furthermore, wettability alteration is one of the primary drive mechanisms of chemically enhanced oil mobilization from the matrix in naturally fractured carbonate reservoirs. It is also an essential mechanism in low salinity and SmartWater flooding. The wettability alteration is often measured by contact angle, which does not provide insights on underlying chemical or physical processes. It is desirable to reveal the microscopic interactions to optimize different oil mobilization processes further.

The rock/fluid interfacial phenomenon and wettability alteration of the oil mobilization processes are often understood from the molecular interactions within the thin layers of the rock/fluids' interface. The observation of the rock surfaces and fluids on the surfaces at a microscopic scale provides direct evidence for any hypothesis. Various microscopic imaging techniques have been employed to investigate the rock/fluid interactions and wettability alteration for oil mobilization mechanisms by chemicals, and other agents such as SmartWater. Atomic force microscopy was employed by Kumar et

al. (2008)[3] to study the wettability alteration by surfactants. Schmatz et al. (2017)[4] observed the mineral/oil/brine contacts down to the nanometer scale using the Cryo-BIB-SEM method and planned to study the low salinity effects. Nuclear magnetic resonance (NMR) dispersion curves measured by fast field cycling (FFC) can be used to infer wettability or affinity of liquids on the surfaces by quantifying the molecular dynamics on the surface without direct imaging.

NMR dispersion refers the frequency dependency expressed as the inverse of longitudinal relaxation time ($1/T_1(\omega)$). Korb et al. (1997)[5] and Korb et al. (1999)[6] are among the first to study the liquid micro-dynamic properties by NMR dispersion. They studied the relaxation rate as the function of frequency on protic fluids, e.g., water, and aprotic fluids, e.g., acetone and acetonitrile, in chromatographic microporous glass beads with paramagnetic contaminants. Two models were proposed to explain the logarithmic and power different behaviors, and the surface diffusion coefficient was derived. The logarithmic dispersion was considered, due to the intermolecular dipolar relaxation of diffusing molecules in the vicinity of paramagnetic ions on the pore surface, where relaxation is modulated by 2D translational diffusion.

The subsequent studies[7, 8] extended to water and oil (dodecane) in macroporous materials such as silica carbide packing and Lavoux limestone, and applied the relaxation models to NMR dispersion introducing a microscopic surface affinity index. The index is defined as the ratio of surface residence time (τ_s) and 2D translational surface correlation time (τ_m) based on the theoretical relaxation model. Intuitively, larger indices indicate more re-encounters during the molecule surface residence time, and a greater affinity of the fluid onto the rock's surface. The method[9, 10] was employed to study the bimodal carbonate rock revealing pore size dependency of wettability. Other researchers apply the NMR dispersion technique to study the fluid/solid surface interactions in other porous media such as oil shale[11], porous ceramic[12], and catalyst[13]. The similar relaxation model[14] is also employed to fit the NMR dispersion curves of crude oil containing asphaltene to derive the shapes and size of the asphaltene aggregates. Recently, Singer et al. (2017)[15] proposed a new NMR relaxation model based on ^{1}H-^{1}H dipole-dipole interactions instead of surface paramagnetism.

The details of the FFC NMR are presented later. This study is to obtain NMR dispersion curves of more rock and fluid types, and to analyze them for the molecular dynamics and wettability characterization.

EXPERIMENTAL MATERIALS AND METHODOLOGIES

Materials

Core samples. Samples of different mineralogy and pore systems were collected and selected for this study. They include two types of sandstones; Berea sandstones, and one reservoir sandstone was selected for their water wetness. Different types of limestones included Indiana limestone, low permeability limestone, and multiple modality carbonates. The carbonates are selected based on their multiple pore systems. Sister plug samples with similar T_2 distributions for each type are used to compare NMR dispersions at different saturation states.

Fluids. Deionized (DI) water was used to saturate the rock samples to evaluate the property of water only, which would be used as a baseline for any probable effects from salinity or particular ions. Mineral oil and light crude oil are used as the oil phases. The S3 mineral oil is a certified viscosity reference standard (3.5 cP at 25 °C). It is known that the asphaltene present in crude oil affects the NMR dispersion. The comparison of mineral oil and crude oil NMR dispersions in rock facilitates the separation of the effects from asphaltene and the rock surface.

FFC NMR Technique

The NMR dispersion is performed on a FFC Spinmaster 2000 relaxometer from Stelar s.r.l., Italy. It has two magnets; 1T for liquids, and a wide bore for 1" diameter cores. The magnetic field strength (B) range of the 1T magnet expressed by Larmor frequencies ($\omega = -\gamma B$) is from 0.01 MHz to 42.65 MHz, and the range of the wide bore magnet is from 0.01 MHz to 18 MHz. The sample temperature of 25 °C is maintained by blowing heated air through the sample bore. Kimmich and Anoardo (2004)[16] provide a comprehensive review. Steele et al. (2015)[17] gave an excellent review of the recent developments of FFC NMR relaxometry. The following introduction focuses on the data acquisition for better quality and data format for subsequent analysis.

The NMR dispersion curve is composed of T_1 measurements obtained with NMR sequences at different magnetic field strengths. Unlike the permanent magnet NMR, where the constant magnetic field is always present, the magnetic field of FFC NMR is generated by a large electrical current for short time periods. NMR sequences different from common inversion and saturation sequences for T_1 were devised. Figure 1a illustrates the nonpolarized sequence, and Fig. 1c illustrates the pre-polarized sequence. Figures 1b and 1d show their free induction decay (FID) measured at one relaxation time (τ) field, respectively.

The nonpolarized sequence is very similar to the saturation sequence of the permanent magnet's NMR during which the magnetic moment increases or recovers from zero to a maximum value under one stable relaxation field, and it is measured by varying τ. The FID shown in Figs. 1b and 1d is measured from a longer τ to a shorter τ. Compared to the nonpolarized sequence, the polarized sequence applies the polarized magnetic field (B_{POL}) for a duration larger than 5 times of T_{1max} first, so that the relaxation measurement at a low and very low relaxation magnetic field becomes practical with the consistent sensitivity — high signal-to-noise ratio

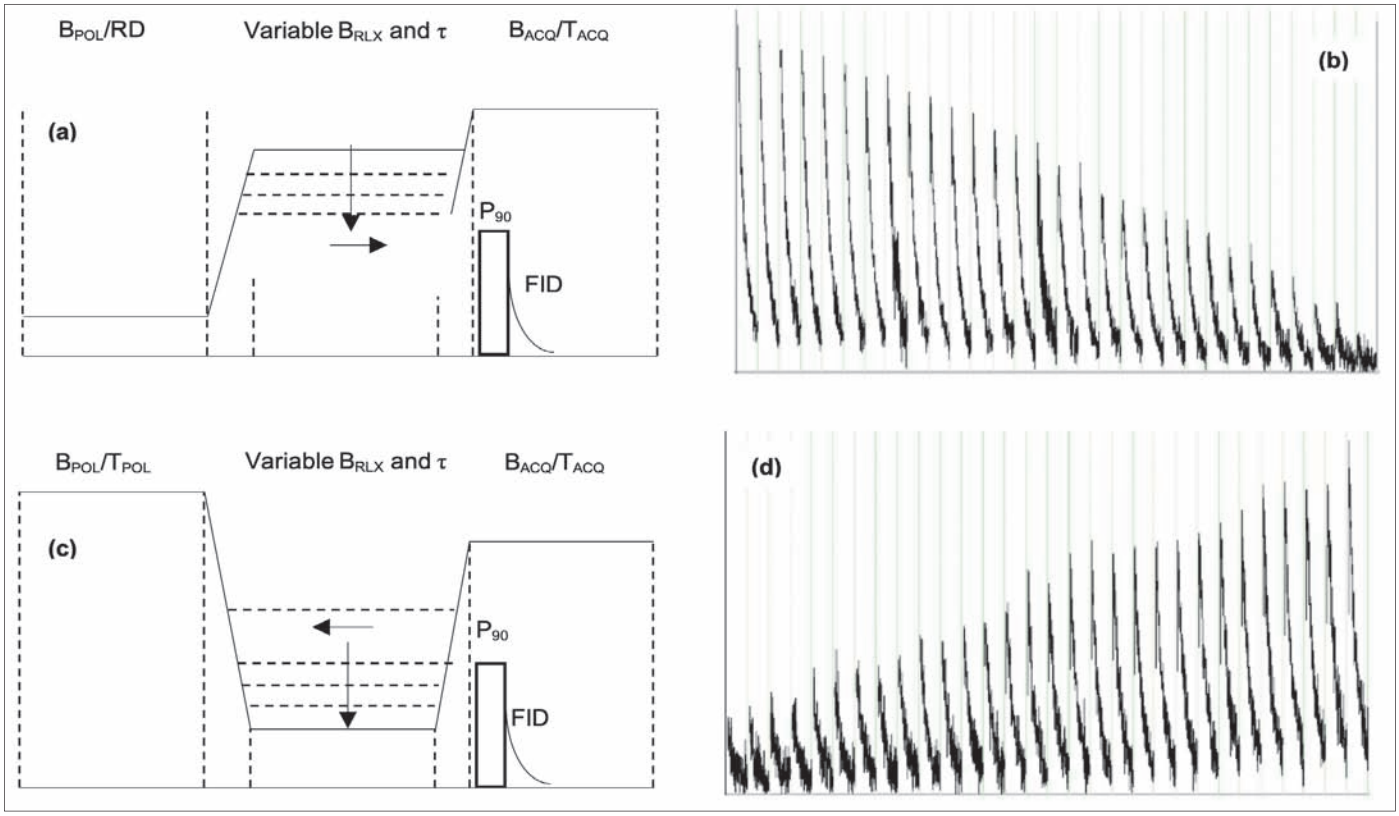

Fig. 1. The nonpolarized sequence (a), and the pre-polarized sequence (c). Each FID output measured at one relaxation field, (b) and (d), respectively.

— of a higher field since the signal-to-noise ratio is proportional to the square root of the Larmor frequency. The signal decays to a lower value corresponding to the relaxation field instead of zero when there is no magnetic field. The FID of both sequences is acquired at one constant acquisition field.

As can be seen from Figs. 1b and 1d, the FID at each relaxation time was measured. The time to complete a whole NMR dispersion curve can be very lengthy, and range from 10 to 20 hours, depending on the T_{1max}. The τ can be equally spaced in logarithmic and linear scales, respectively, while the logarithm concentrates on the short τ, and the linear on the longer τ. Estimated from the initial measurement, the τ can be customized to concentrate on the range of interest, which saves time and improves efficiency. For samples with the short T_1, a logarithmic scale was used while for samples of medium and long T_1, a customized list focusing on the τ of interest was used. There were either 30 equally spaced τ values for logarithmic scale, or 28 τ values for the customized list, to cover the whole gain or decay curves where the maximum τ equals $4*T_{1amx}$ as default. Here, 25 or 30 frequencies were all equally spaced in a logarithmic scale from 0.01 MHz to 18 MHz.

Experimental Procedure

A simple experimental work flow is shown in Fig. 2. The dry and clean core samples were first saturated with DI water after being in a vacuum for more than 8 hours. The T_2 distributions of the 100% water saturated (Sw) samples were obtained using a 12.8 MHz Maran Ultra spectrometer from Oxford Instruments for the pore size distributions and verification. The NMR dispersion curves were obtained on all Sw samples. Then the core samples were divided into two groups based on their mineralogy and pore size distributions with each group containing one of the sister samples.

Five pore volumes of mineral oil were injected through the Group 1 samples to reach irreducible water (D_2O) saturation, and D_2O saturation with mineral oil and crude oil. The samples of Group 2 were dried in the oven again at 110 °C overnight and saturated with mineral oil directly after being in a vacuum. Then they were flooded with five pore volumes of crude oil. NMR dispersion curves were obtained at 100% mineral and crude oil saturation.

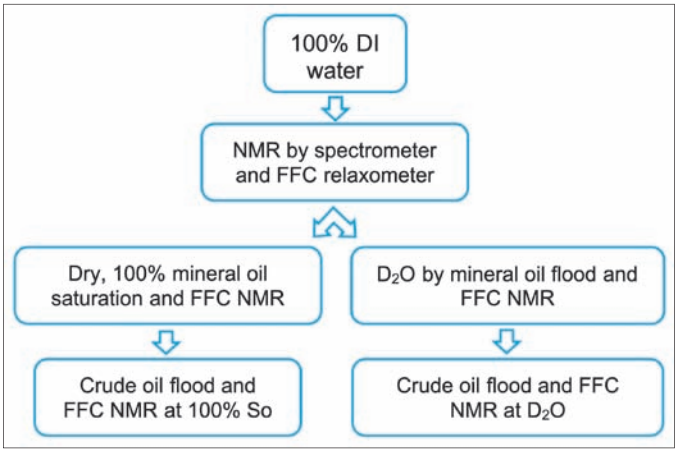

Fig. 2. Experimental procedure.

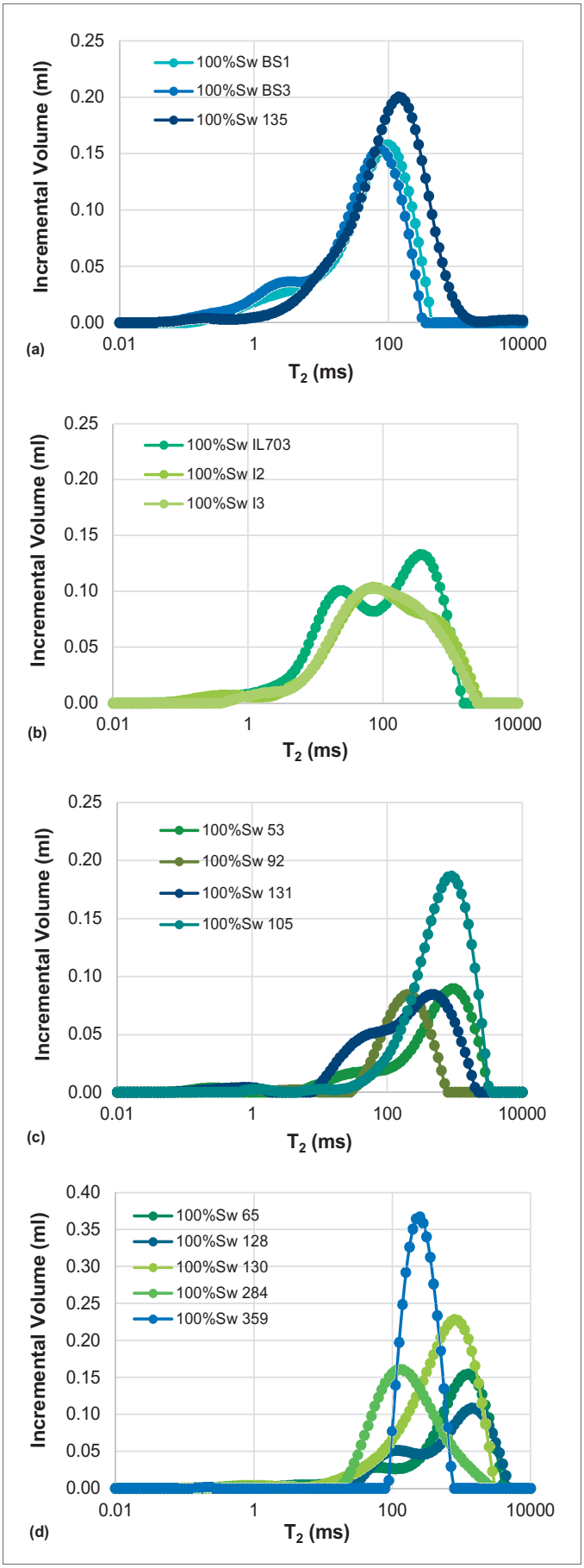

Fig. 3. T_2 distributions of core samples: (a) sandstones, (b) limestones, (c) single fluid carbonates, and (d) two fluid carbonates.

Data Analysis

The software calculates the FID amplitudes by averaging the initial points selected, which is used for T_1 by single exponential fitting on the gain or decay curves. The NMR dispersion curve is obtained by combining all single T_1 at different relaxation frequencies. It works well with samples with a narrow T_1 distribution, or the interest is only on the average T_1. If the T_1 distribution of a sample has multiple peaks and the interest is on the NMR dispersion on individual peaks, multiple exponential fitting needs to be conducted. It is performed by using WinDXP from Oxford Instruments after manually reversing the decay curves from the polarized sequences before obtaining a specialized processing program. The gain curves can be analyzed directly by WinDXP. The analysis of the NMR dispersion of different pore systems is beyond the scope of this study.

As discussed in the introduction, Korb et al. (1997)[5] and Korb et al. (1999)[6] proposed the relaxation models and obtained the correlation times by fitting the NMR dispersion curves for the affinity index. The equations and derivation are referred to in their studies[5-7, 9, 10]. Only a qualitative assessment was performed due to the lack of necessary parameters.

RESULTS AND DISCUSSION

Core Sample Pore Structure by T_2 Distributions

The T_2 distributions of the 100% DI Sw sample are illustrated in Fig. 3. They were divided into two groups, a single fluid, which was always 100% saturated with one fluid, and two fluids, which was a D_2O saturation after 100% Sw measurement, so as to compare the NMR dispersion of the same flood at different saturations. Berea sandstone — BS1 and BS2 — are sister samples in Fig. 3a. Indiana limestone — I2 and I3 — are sister samples in Fig. 3b. They mainly have very similar pore structures. Similarly, carbonates were paired according to the multiple modalities[18]. Samples 105 and 130, 131 and 128, 53 and 65, 92 and 284, were selected as sister samples based on the pore structure shown in Figs. 3c and 3d, with similar distributions. Sample 135 is a sandstone; Indiana limestone IL703 is typically bimodal, which can be compared to carbonate samples of close pore systems. Sample 359 is a homogeneous limestone of low permeability.

NMR Dispersion of Bulk Fluids

The NMR dispersion curves of water, S3 mineral oil, and crude oil are presented in Fig. 4a. The relaxation rates of DI water and S3 mineral oil are 2.55 seconds and 0.48 seconds, respectively. They do not change with frequency as expected in bulk liquids. The relaxation rate uniformity of DI water and S3 mineral oil reflects the consistency and accuracy of measurements over the frequency range with nonpolarized and polarized sequences. For example, the T_1 values of DI

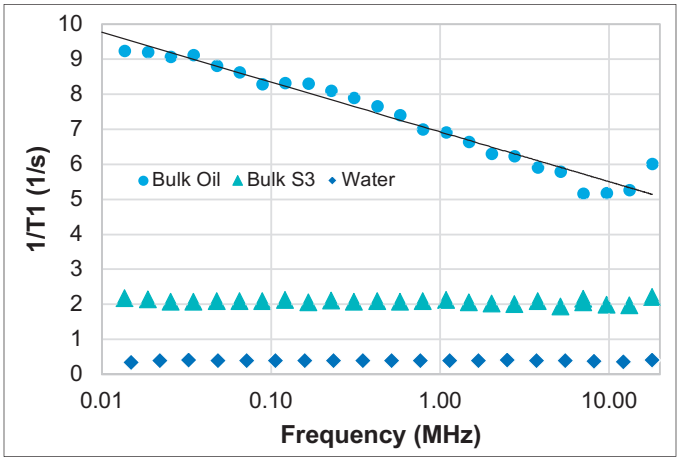

Fig. 4a. The NMR dispersion curves of bulk oil, S3 mineral oil, and water.

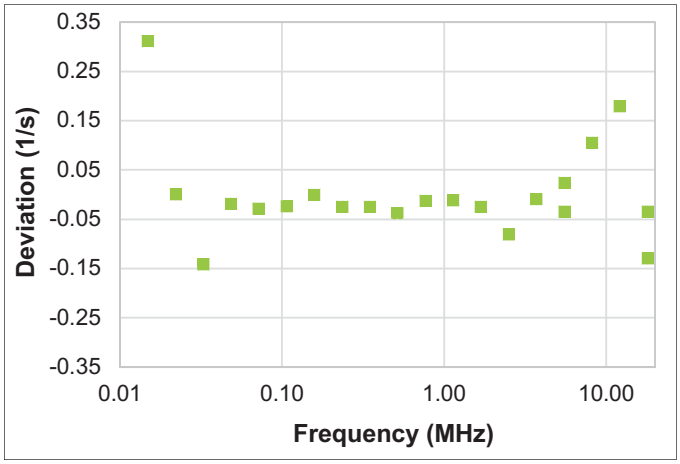

Fig. 4b. The deviation values of DI water.

water mostly fall into the range of 2.55 ± 0.05 seconds, indicated in Fig. 4b. The T_1 log mean of the S3 mineral oil is 0.50 seconds by saturation sequence, and 0.53 seconds by inversion sequence using 12.8 MHz spectrometers.

As shown from the oil NMR dispersion trend line, the NMR dispersion of crude oil has a logarithmic frequency dependency indicating a small amount of asphaltene present in this crude[14]. Korb et al. (2013)[14] obtained the residence and 2D translational τ_m using the equation derived from asphaltene aggregates surface relaxation model similar to the rock surface. The asphaltene effect will be present for NMR dispersion of the crude oil in the cores. It needs to be considered when analyzing the NMR dispersion of core samples to obtain the net rock surface effect.

100% Saturated with a Single Phase Fluid

The NMR dispersion of 15 core samples at 100% Sw and bulk water are illustrated in Fig. 5a. The NMR dispersion of five core samples at 100% S3 mineral oil saturation, and five samples at 100% crude oil saturation are illustrated in Fig. 5b, along with bulk S3 mineral and crude oil.

In Fig. 5a, most samples — Samples BS1, BS3, I2, I3, 92, 105, 128, 130, 131, 284, and 359 — appear to be bi-logarithmic frequency dependent while others — Samples IL703, 135, 53, and 65, with trend lines — are mono-logarithmic frequency dependent. Godfroy et al. (2001)[7] and Korb et al. (2003)[8] observed both NMR dispersion mono-logarithmic and bi-logarithmic dependency of water in silica carbide packing, outcrop and low permeability reservoir carbonate rocks, and fitted the data with respective equations. They attributed the difference to be caused by "the ligand field between the proton molecular species and paramagnetic impurities on the pore surface." The affinity index, the ratio of residence τ_s and 2D translational diffusion τ_m, is obtained from the fitting using the equations. Other parameters such as surface density of paramagnetic impurities are needed for the fitting, which are not currently available for all core samples to obtain the affinity index. The affinity index can be still assessed qualitatively from the NMR dispersion since the large slope indicates a large affinity index or water wetness for the same types of samples in these studies.

In Fig. 5b, the NMR dispersion of all samples are mono-logarithmic frequency dependent with the exception of Sample 92. The slopes of four 100% S3 mineral oil saturated samples — Samples BS3, I2, 53, and 105 — are smaller than the 100% water and crude oil saturated samples, especially

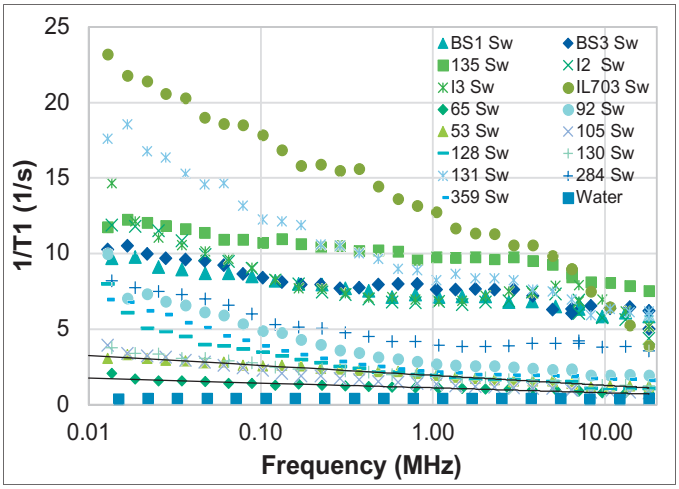

Fig. 5a. The NMR dispersion of 15 core samples at 100% Sw.

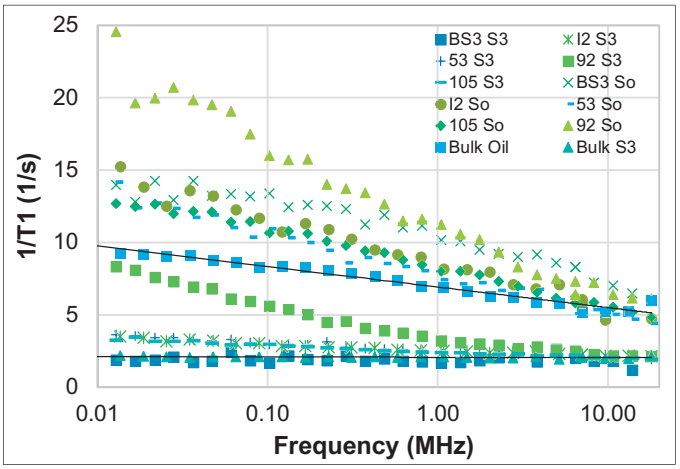

Fig. 5b. The NMR dispersion of samples at 100% saturation with a single fluid.

Sample BS3, whose NMR dispersion is the same as the bulk S3 mineral oil with a trend line. The low slopes may be associated with the molecular structure and size of this mineral oil affecting the interaction between paramagnetic ions and protons. Slopes of Sample 92 at 100% Sw and S3 mineral/crude oil saturations are the largest among the carbonate samples, and all samples. It might contain a higher percentage of paramagnetic impurities. The NMR dispersion slopes of the 100% crude oil saturated carbonate samples are comparable to the ones of 100% Sw, considering the NMR dispersion of crude oil with a trend line in the graph. For sister samples, the Berea sandstones — BS1 and BS3 — and Indiana limestones — Sample I2 and I3 — their slopes of 100% Sw and crude oil saturation are similar.

It is interesting to compare the NMR dispersion of 100% Sw and crude oil saturation among sample groups and sister samples for understanding wettability, which indicates the rock surface preference to different fluids. For example, the Berea sandstones are known to be typically water-wet, and Indiana limestones are intermediate wet or weakly water-wet. The water affinity of Indiana limestone — Samples I2 and I3 — is even slightly larger than the Berea sandstones — Samples BS1 and BS3 — from 100% Sw. What may render the Berea sandstones more water-wet than Indiana limestone is their small oil affinity indicated by Sample BS3 at 100% S3 mineral oil saturation and Sample BS1 at 100% crude oil saturation. Another example is the comparison between two carbonate samples — Samples 53 and 105 — which have NMR dispersion of all three fluids at 100% saturation. Their NMR dispersion at 100% S3 mineral oil and crude oil saturation are very close, and a larger slope of Sample 105 at 100% Sw indicates its more water-wet than Sample 53. The quantitative comparison can be performed from the affinity index calculation in a future study.

D_2O Saturation

Figure 6a shows the NMR dispersion for the Berea and Indian sandstone samples at D_2O saturation. Figure 6b shows the NMR dispersion of the carbonate samples saturated with bulk mineral and crude oil; trend lines are shown for comparison. They were obtained after oil flood without an extended aging period. The NMR dispersion was from mineral oil and crude oil, as D_2O was used as a water phase. The study will continue monitoring any changes with time, and water may be introduced for the NMR dispersion of a water phase at the end.

Since the mineral oil was injected into 100% D_2O saturated samples, it does not contact all rock surfaces in the presence of water despite the wettability. It is expected that the NMR dispersion of both mineral and crude oil fall between bulk oil without the effect of a rock surface, and 100% oil saturation with the full effect of a rock surface. The results do not fully verify this assumption. It is not obvious for the S3 mineral oil samples due to the small slopes; however, they are comparable

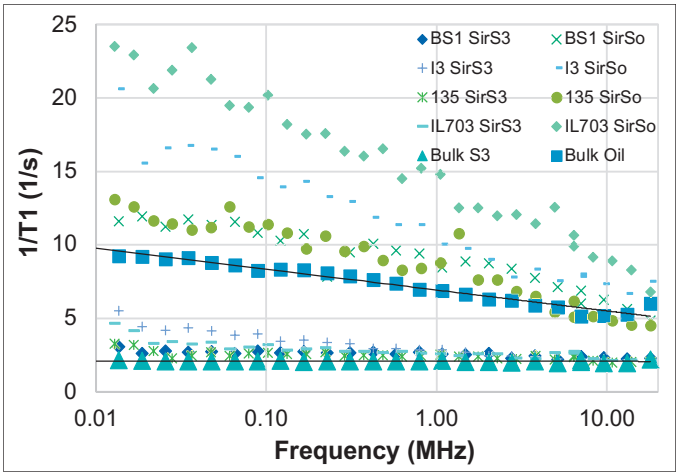

Fig. 6a. The NMR dispersion for the Berea and Indiana sandstone samples at D_2O saturation.

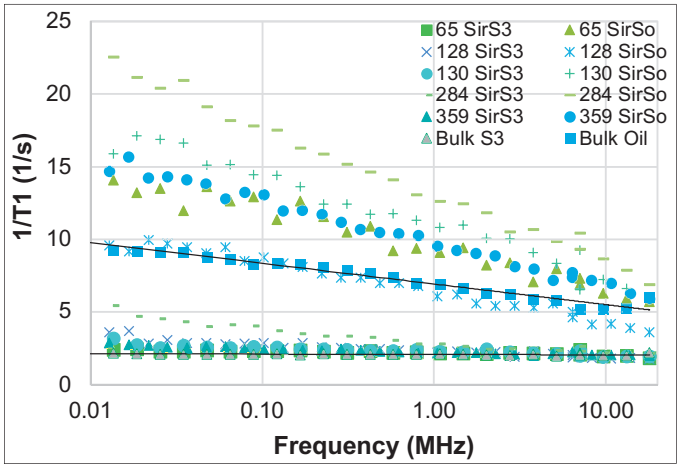

Fig. 6b. The NMR dispersion of the carbonate samples saturated with bulk mineral and crude oil.

to the ones in Fig. 5b.

For crude oil samples, some samples agree with the above assumption, such as Samples 284, BS1, 135, and 284, which indicates a smaller oil affinity index. Some samples, such as Samples 65, 130, and 359 have comparable slopes, and others such as Samples I3 and 284 have larger slopes approaching 100% crude oil, and are larger than the average of four carbonates previously seen in Fig. 5b. The slopes of IL703 at 100% Sw and D_2O with crude oil are close, and they are the largest among all samples. It appears that paramagnetic impurities somehow tend to interact with protons relaxation rather effectively despite D_2O.

CONCLUSIONS

NMR dispersion was obtained from core samples of different mineralogy and pore types at various saturation states. The wettability of common types of cores selected was analyzed based on their affinity to water and oil from the assessment of their NMR dispersion at various saturation states. The following conclusions can be drawn from the current study on the core sample selected:

1. The affinity of both water and oil to the surface of most core samples is significant. The wettability is determined by their relative strength.
2. The water affinity of sandstones is not the largest of all core samples, and their low oil affinity indicated at 100% oil saturation and D_2O saturation contribute to a water-wet property.
3. Both water and oil affinity of carbonate samples are small to moderate. The water affinity can be small while the oil affinity is above a specific value, which makes the carbonate sample intermediate wet.
4. The water and oil affinity of the limestone samples may vary considerably, and they can be relatively strong water-wet or oil-wet.
5. The oil has access to the rock surface of most samples at D_2O saturation, especially the carbonate samples, due to their relatively strong oil affinity.

ACKNOWLEDGMENTS

The authors would like to thank the management of Saudi Aramco for their support and permission to publish this article. The authors would also like to thank Marwa Sinan for reading the manuscript and Mustafa Satrawi for the assistance with the experiments.

This article was presented at the SPE Kingdom of Saudi Arabia Annual Technical Symposium and Exhibition, Dammam, Saudi Arabia, April 23-26, 2018.

REFERENCES

1. Craig Jr., F.F.: *The Reservoir Engineering Aspects of Waterflooding*, New York, U.S.A., H.L. Doherty Memorial Fund of AIME, 1971, 134 p.
2. Okasha, T.M., Funk, J.J. and Rashidi, H.N.: "Fifty Years of Wettability Measurements in the Arab-D Carbonate Reservoir," SPE paper 105114, presented at the SPE Middle East Oil and Gas Show and Conference, Manama, Kingdom of Bahrain, March 11-14, 2007.
3. Kumar, K., Dao, E.K. and Mohanty, K.K.: "Atomic Force Microscopy Study of Wettability Alteration by Surfactants," *SPE Journal*, Vol. 13, Issue 2, June 2008, pp. 137-145.
4. Schmatz, J., Klaver, J., Jiang, M. and Urai, J.L.: "Nanoscale Morphology of Brine/Oil/Mineral Contacts in Connected Pores of Carbonate Reservoirs: Insights on Wettability from Cryo-BIB-SEM," *SPE Journal*, Vol. 22, Issue 5, October 2017, pp. 1374-1384.
5. Korb, J-P., Whaley-Hodges, M. and Bryant, R.G.: "Translational Diffusion of Liquids at Surfaces of Microporous Materials: Theoretical Analysis of Field-Cycling Magnetic Relaxation Measurements," *Physical Review E*, Vol. 56, Issue 2, August 1997, pp. 1934-1937.
6. Korb, J-P., Hodges, M.W., Gobron, T. and Bryant, R.G.: "Anomalous Surface Diffusion of Water Compared to Aprotic Liquids in Nanopores," *Physical Review E*, Vol. 60, Issue 3, September 1999, pp. 3097-3106.
7. Godefroy, S., Korb, J.P., Fleury, M. and Bryant, R.G.: "Surface Nuclear Magnetic Relaxation and Dynamics of Water and Oil in Macroporous Media," *Physical Review E*, Vol. 64, Issue 2, July 2001, pp. 021605-021618.
8. Korb, J-P., Godefroy, S. and Fleury, M.: "Surface Nuclear Magnetic Relaxation and Dynamics of Water and Oil in Granular Packings and Rocks," *Magnetic Resonance Imaging*, Vol. 21, Issues 3-4, April-May 2003, pp. 193-199.
9. Korb, J-P., Freiman, G., Nicot, B. and Ligneul, P.: "Dynamical Surface Affinity of Diphasic Liquids as a Probe of Wettability of Multimodal Porous Media," *Physical Review E*, Vol. 80, Issue 6, December 2009, p. 061601.
10. Korb, J-P., Nicot, B. and Ligneul, P.: "Probing Wettability in Carbonate Rocks by Multi-Frequency NMR Relaxation," *AIP Conference Proceedings*, Vol. 1330, Issue 1, 2011, pp. 81-84.
11. Faux, D.A. and McDonald, P.J.: "Explicit Calculation of Nuclear Magnetic Resonance Relaxation Rates in Small Pores to Elucidate Molecular-Scale Fluid Dynamics," *Physical Review E*, Vol. 95, Issue 3, March 2017, pp. 033117-033120.
12. Muncaci, S., Mattea, C., Stapf, S. and Ardelean, I.: "Frequency-Dependent NMR Relaxation of Liquids Confined Inside Porous Media Containing an Increased Amount of Magnetic Impurities," *Magnetic Resonance in Chemistry*, Vol. 51, Issue 2, January 2013, pp. 123-128.
13. Mitchell, J., Broche, L.M., Chandrasekera, T.C., Lurie, D.J., et al.: "Exploring Surface Interactions in Catalysts Using Low-Field Nuclear Magnetic Resonance," *The Journal of Physical Chemistry C*, Vol. 117, Issue 34, 2013, pp. 17699-17706.
14. Korb, J-P., Louis-Joseph, A. and Benamsili, L.: "Probing Structure and Dynamics of Bulk and Confined Crude Oils by Multiscale NMR Spectroscopy, Diffusometry, and Relaxometry," *The Journal of Physical Chemistry B*, Vol. 117, Issue 23, 2013, pp. 7002-7014.
15. Singer, P.M., Chen, Z., Alemany, L.B., Hirasaki, G.J., et al.: "NMR Relaxation of Polymer — Alkane Mixes, a Model System for Crude Oils," paper presented at the SPWLA 58th Annual Logging Symposium, Oklahoma City, Oklahoma, June 17-21, 2017.
16. Kimmich, R. and Anoardo, E.: "Field-Cycling NMR Relaxometry," *Progress in Nuclear Magnetic Resonance Spectroscopy*, Vol. 44, 2004, pp. 257-320.
17. Steele, R.M., Korb, J-P., Ferrante, G. and Bubici, S.: "New Applications and Perspectives of Fast Field Cycling

NMR Relaxometry," *Magnetic Resonance in Chemistry*, Vol. 54, Issue 6, June 2016, pp. 502-509.

18. Clerke, E.A.: "Permeability and Microscopic Displacement Efficiency of M_1 Bimodal Pore Systems in Arab D Limestone," SPE paper 105259, presented at the SPE Middle East Oil and Gas Show and Conference, Manama, Kingdom of Bahrain, March 11-14, 2007.

BIOGRAPHIES

Jun Gao joined Saudi Aramco in October 2015 and is currently working in Saudi Aramco's Exploration and Petroleum Engineering Center – Advanced Research Center (EXPEC ARC) as a Petroleum Scientist with the Reservoir Engineering Technology Division. Prior to joining Saudi Aramco, he worked as a Research Scientist on multiple advanced enhanced oil recovery (EOR) studies for oil companies at Tomographic Imaging and Porous Media Laboratory (TIPM lab) in Perm Inc. and the University of Calgary. Prior to that, Jun worked as a Petroleum Engineer on national chemical EOR research projects at the Geological Scientific Research Institute, Shengli Oil Field Company, and China Petroleum & Chemical Corporation (Sinopec).

He has over 25 years of research experience in special core analysis and EOR, including chemical, thermal, and carbon dioxide techniques, assisted by imaging technologies such as X-ray computer tomography and nuclear magnetic resonance imaging.

Jun received his B.S. degree in Physics from Shandong University, Shandong, China, his B.Eng. degree in Petroleum Engineering from the China University of Petroleum (East China), Qingdao, China, and his M.S. degree in Petroleum Engineering from the University of Calgary, Calgary, Alberta, Canada.

Dr. Hyung T. Kwak joined Saudi Aramco in April 2010 as a Petroleum Engineer with Saudi Aramco's Exploration and Petroleum Engineering Center – Advance Research Center (EXPEC ARC). He had been a member of Pore Scale Physics focus area (2010 to 2012) and SmartWater Flooding focus area (2013 to 2014) of the Reservoir Engineering Technology Division. Currently, Hyung is a focus area champion of the Pore Scale Physics focus area. His main research focus is seeking deeper understanding of fluid-rock interaction in pore scale of the Kingdom's reservoirs.

Since joining Saudi Aramco in 2010, Hyung has been involved with various improved oil recovery and enhanced oil recovery (EOR) research projects, such as SmartWater Flooding, carbon dioxide EOR, and chemical EOR. Prior to joining Saudi Aramco, Hyung was a Research Scientist at Baker Hughes, with a main area of research related to nuclear magnetic resonance (NMR)/magnetic resonance imaging technology.

In 1996, Hyung received a B.S. degree in Chemistry from the University of Pittsburgh, Pittsburgh, PA, and in 2001, he received his Ph.D. degree in Physical Chemistry from Ohio State University, Columbus, Ohio.

Before moving into the oil and gas industry, Hyung was involved — as a postdoctoral fellow for 2 years — in a project developing the world's largest wide bore superconducting magnet NMR spectrometer, 900 MHz, at the National High Magnetic Field Laboratory.

He has 100+ publications, including peer-reviewed articles and patents.

Dr. Ahmad M. Al-Harbi is a Petroleum Engineer in the Pore Scale Physics Group of the Reservoir Engineering Technology Division in Saudi Aramco's Exploration and Petroleum Engineering Center – Advanced Research Center (EXPEC ARC). His current research focus is seeking solutions for ultimate recovery from Saudi Arabian reservoirs by acquiring deeper understandings of fluid dispersion, pore connectivity, and fluid-rock interaction in porous media.

Ahmad has 15 years of experience in the oil industry with Saudi Aramco. He has been involved with various enhanced oil recovery (EOR) research projects, such as chemical EOR.

In 2001, Ahmad received his B.S. degree in Chemical Engineering from King Fahd University of Petroleum and Minerals (KFUPM), Dhahran, Saudi Arabia, and in 2013, he received his Ph.D. degree in Petroleum Engineering from the University of Calgary, Calgary, Alberta, Canada.

Surface to Borehole Electromagnetics for 3D Waterflood Monitoring: Results from First Field Deployment

Dr. Daniele Colombo, Gary W. McNeice, Dr. Nestor H. Cuevas, and Mauro Pezzoli

ABSTRACT

Monitoring the waterflood oil recovery process is a difficult task for seismic-based methods in hard carbonate reservoirs. The changes in velocity/density due to water-oil substitution are too small when compared to the errors involved in repeating the measurements. We detail the development of a novel technique based on surface-to-borehole controlled source electromagnetics (CSEM), which exploits the large contrast in resistivity between injected water and oil to derive 3D resistivity distributions (proportional to saturations) in the reservoir.

Surface-to-borehole CSEM responses using surface electric transmitters and borehole electromagnetic (EM) receivers were modeled using a black oil simulator for a large oil field in the Middle East. Results indicate that the vertical component of the electric field (E_z) can be used to detect waterfront changes in 2- and 5-year time-lapse scenarios. A surface-to-borehole acquisition system was engineered comprising the development of a powerful, custom-made electric transmitter — 2,000 volts (V)/500 amperes (amp) — and borehole electric and magnetic field sensors. The surface-to-borehole 3D CSEM technology was deployed for the first field trial in the same well used for the modeling study.

The field demonstration was carried out in 2017, comprising 144 permanent surface electrodes drilled in a radial configuration around a vertical observation well. The current electrodes were designed in an "L" pattern to form 48 inline (radial) and 48 cross-line (tangential) dipoles at a nominal range of 600 m to 3,500 m from the vertical observation well. A wireline sensor array comprising two vertical E_z and two vertical magnetic field sensors recorded the EM signal transmitted from the surface in regularly spaced positions in the reservoir section. Surface measurements of transient EM, CSEM and magnetotellurics (MT) were recorded together with the borehole acquisition to characterize the overburden and the shallow subsurface.

The acquired data set was processed to increase the signal-to-noise content of the data as well as to correct for casing effects and surface distortions. A marked asymmetry of the EM responses is recorded in the vicinity of the observation well, which translates, after 3D inversion, to resistivity distributions consistent with the saturation/production logs acquired in the nearby wells. The sensitivity of the inversion extends up to 1.8 km away from the observation well. Analysis of the measurement repetition errors compared to predicted EM responses after 2 and 5 years indicates that time-lapse surveys would provide detailed mapping and an independent estimation of saturation variations related to waterflooding.

The encouraging results obtained from the first surface-to-borehole CSEM survey in a producing oil field suggests that the technology may become an important tool for analyzing the waterfront evolution in the interwell space. By doing this, the technology is expected to enhance reservoir management and history matching.

INTRODUCTION

Primary or secondary oil recovery methods rely on waterflooding where water is injected at the periphery of the reservoir to sustain production at the crest of the structure. Monitoring of the injected water movement in the reservoir is of primary importance for optimizing reservoir management. Geophysical technologies need to be developed to assist the detection and the mapping of the waterfront evolution in the reservoir. Seismic-based methods provide limited sensitivity to the water-oil substitution in typical hard carbonate reservoirs. The repeatability of seismic measurements in land conditions is also problematic and subject to large spatial and seasonal variability of the near surface layer[1].

Gravity measurements, considering only borehole sensing[2] at the reservoir level, are estimated to achieve repeatability errors of 10 μGal or larger in the vertical component. In Middle East carbonate reservoirs, modeling of the gravity response after two years of waterflooding is below the noise threshold at 500 m from the waterfront[3]. Electromagnetic (EM) methods provide better opportunities for monitoring since the changes in bulk reservoir resistivity caused by water-oil substitution can be in the range of 1 order of magnitude or more[4]. The rapid decay of the EM signal — skin depth effect — suggests that the expected sensitivity and resolution can be achieved only by measuring the EM fields in proximity to the reservoir[5].

Controlled source electromagnetic (CSEM) techniques for

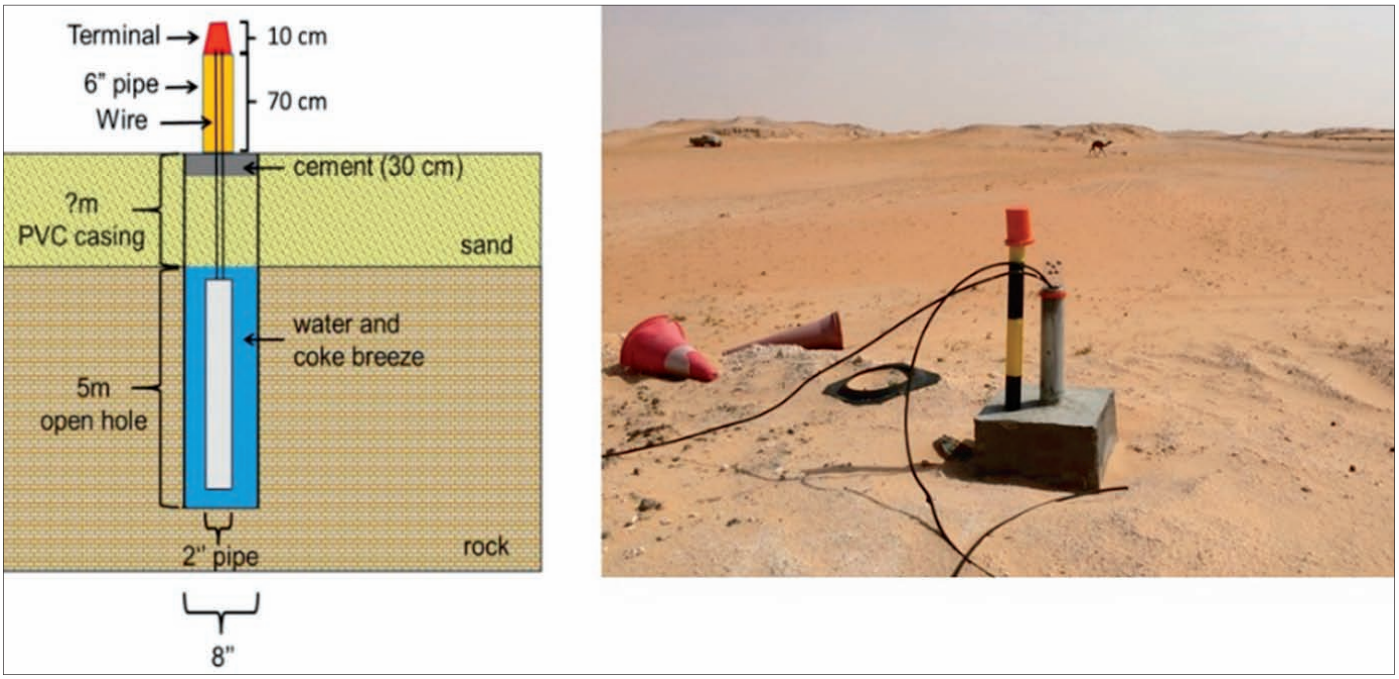

Fig. 1. Schematic (left) and an actual image (right) of the surface electrode installation.

reservoir fluid characterization and monitoring are applied on a commercial basis for cross-well configurations[6, 7]. The method is based on EM induction and as such uses magnetic sources and magnetic receivers. While successfully implemented in many field trials, the method is limited to 2D geometries — relatively short distances between wells — and its sensitivity is biased toward detecting conductors. Modeling has shown that the setup of magnetic sources and magnetic receivers in a 3D surface-to-borehole configuration does not provide a useful signal above the estimated noise floor[4].

For such configurations, an electric source needs to be adopted. Realistic modeling of 3D surface-to-borehole CSEM, using resistivity distributions derived from a black oil reservoir simulator[8], suggested that the vertical component of the electric field (E_z) is the only component of the EM radiation showing a signal above the estimated noise floor for waterfront variation in 2 years. Other results from the study were that the sensitivity to the reservoir conditions for the specific acquisition setup was up to 2 km from the well and that the assumed noise floor in the measurement would have required a source moment of at least 10,000 amps[4]. The results of the study led to modifications of the cross-well EM acquisition system[6, 7] where vertical E_z sensors were added to the existing magnetic field sensors. A powerful custom electric current source was also developed. The source is capable of transmitting (Tx) coded waveforms with up to 2,000 V (peak-to-peak) at 500 amps to the ground[9].

This acquisition system was used to perform the world's first surface-to-borehole CSEM project for detecting and monitoring the evolution of the waterfront around a test well in a large onshore oil field. In this article we detail the results and the work planned for the interpretation of the rich data set acquired.

SURVEY DESIGN

3D surface-to-borehole CSEM data were acquired in a deep (reservoir level) research well drilled near the known waterfront position. Surface current dipoles (Tx antennas) were prepared by drilling shallow boreholes and completing them with a steel pipe coupled to the rock formations using a slurry of carbon backfill — coke breeze — to achieve sufficient electrical contact, Fig. 1. The electrode setup was completed by cementing the top. Electrodes forming the dipole antennas were installed at a 200 m separation, forming a setup of 48

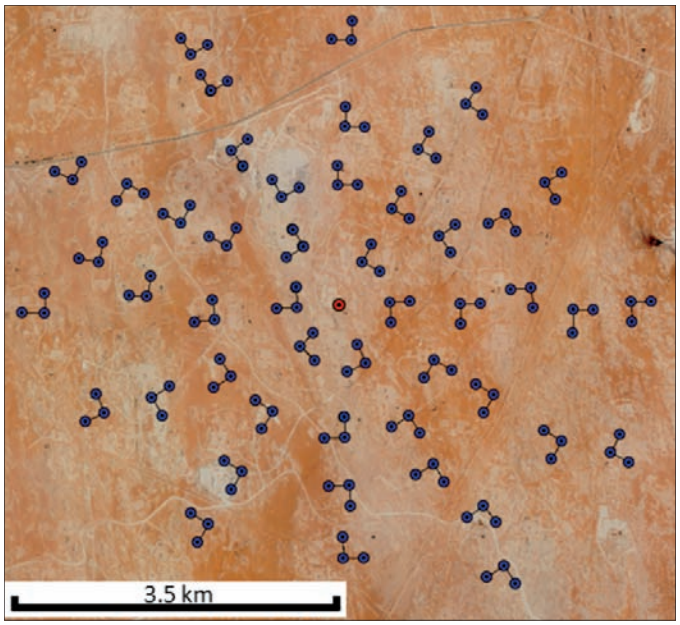

Fig. 2. Distribution of surface dipole electrodes around the monitoring well. The "L" shaped setup provides radial and tangential polarization directions maximizing the strength of the vertical electric and vertical magnetic fields, respectively, in the borehole receiver array.

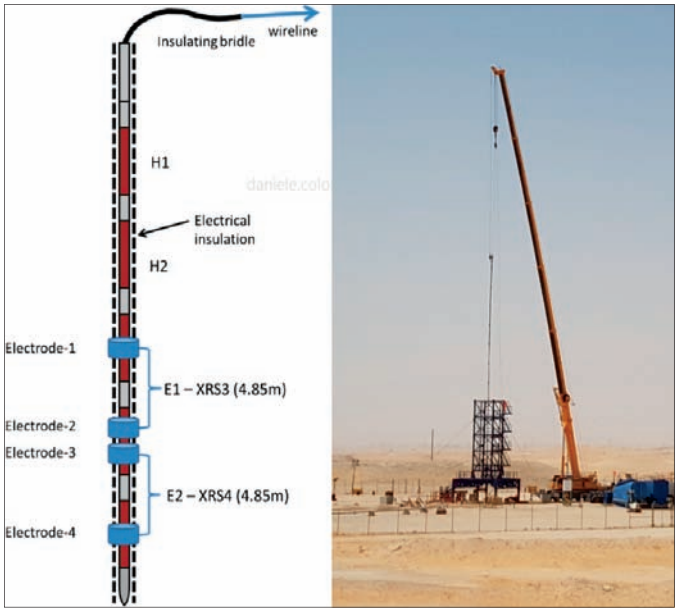

Fig. 3. Details of the electric/magnetic borehole receiver array and wireline operations at the observation well.

inline (radial direction) and 48 crossline (tangential direction) dipoles generating a vertical E_z and vertical magnetic field at the observation well, Fig. 2. An average contact resistance of 2.1 ohm was achieved for the 144 electrodes representing an excellent result, considering the dry surface conditions characteristic of the desert environment. A nominal current of 100 amps at the fundamental frequency of 8 *Hz* was transmitted to the ground enabling a source moment of 20,000 amps for each Tx position.

The borehole receiver comprised two vertical magnetic field sensors — H1 and H2 — and two vertical E_z sensors — E1 and E2 — coupled to the borehole walls by means of well centralizers. The receiver array was operated as a wireline tool where special care had to be taken to insulate the electrodes from the wireline cable and from the body of the tool, Fig. 3. The receiver setup was operated by means of a crane, and the Tx receiver synchronization was provided by GPS timing. Possible distortions of the vertical E_z signal at the Tx electrodes (typically called galvanic distortions or "statics") can be generated by localized heterogeneities in the resistivity structure that need to be accurately described.

For this purpose, time domain EM measurements relying on EM induction — magnetic field measurements — were acquired for each electrode position at the surface to provide a detailed model of the near surface resistivity. Low frequency magnetotellurics (MT) and surface-surface CSEM data were also acquired to build a 3D model of the overburden. The additional data provides primary sensitivity to the overburden, and during interpretation allows us to control and separate the response of the overburden from the response of the reservoir.

The measured data are of good quality, and recorded the fundamental transmitted frequency of 8 *Hz* even from the most distant Tx positions at 3.5 km — horizontal distance — from the observation well. Figure 4 shows the spectra of the recorded fields for a Tx position located 2.6 km away from the well. The 8 *Hz* transmitted signal is clearly visible and is not affected by other signals such as telemetry or power line harmonics. Considering that this was the first time that such surface-to-borehole EM measurements were taken, this represented a first milestone of the experiment, suggesting that the acquisition setup was effective and working as expected.

DATA ANALYSIS

Figure 5 shows the data measured in the reservoir for different Tx offsets along one of the radial acquisition lines. Starting from the analysis of the vertical magnetic field, it can be seen that the amplitude measurements slowly decay with depth as the distance from the Tx source increases. The relative offset between the curves (color coded) is related to the increasing distance from the Tx position from the well, Fig. 5a. An azimuthal analysis around the well also shows small variations of the magnetic field suggesting little sensitivity to the reservoir saturation variations. The vertical E_z measurements provide a large sensitivity to the resistivity structure at the well when compared with the resistivity log, Figs. 5b and 5c. Vertical changes in resistivity cause changes in the vertical E_z at the borehole due to the requirement that the vertical current density be continuous.

Given that the EM sensitivity is mainly concentrated at the

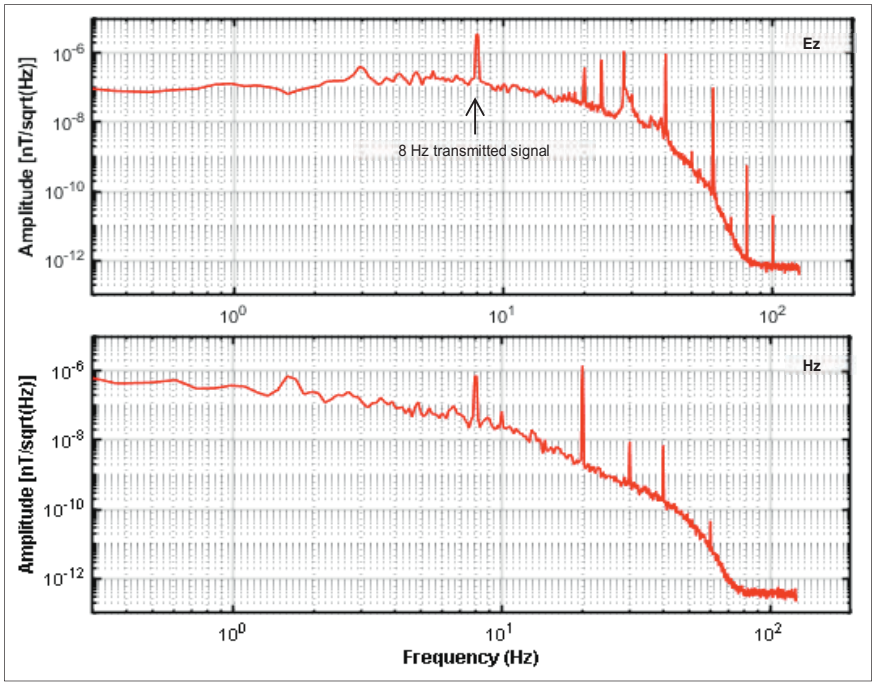

Fig. 4. Fourier transform of the signal recorded by the vertical E_z and vertical magnetic fields with the Tx positioned at 2.6 km away from the well.

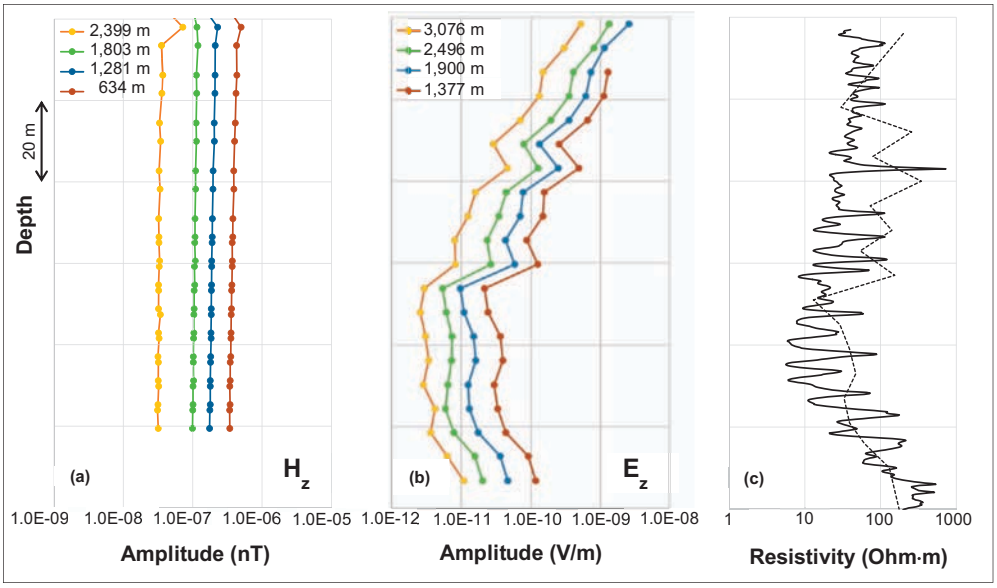

Fig. 5. Comparison of field measurements vs. parameter variations in the reservoir section, including: (a) H_z amplitude at various Tx offsets, (b) vertical E_z amplitude at various Tx offsets, and (c) induction log resistivity (continuous curve) with reconstructed resistivity from vertical E_z measurements (dashed line).

source and receiver locations[4, 10] it is clear the measured vertical E_z is primarily influenced by the reservoir resistivity structure at the well position. Using a reference resistivity of a vertical E_z logged section beneath the reservoir, we can calibrate the relative vertical E_z variations and reconstruct the reservoir resistivity profile directly from the vertical E_z measurements, Fig. 5c. The reconstructed resistivity distribution matches quite well with the log resistivity except for the upper section of the reservoir where the effect of the casing starts to influence the vertical E_z measurements. The vertical E_z measurements need to be corrected for the secondary field produced by the steel casing, which is rapidly decaying with increasing distance from the casing shoe. Estimation of the casing effects and its removal from the measured data is ongoing and different approaches are being evaluated, including semi-analytical[11] and finite element[12] solutions.

Azimuthal and offset variations in the data are compared using circular plots of the interpolated vertical E_z data and the corresponding resistivity variations derived from the reservoir simulator, Fig. 6. It should be noted that the vertical E_z data — phase in this case — is the residual value obtained from the difference between the observed data and the forward modeled fields using a constant reservoir resistivity, and the overburden horizontal (Rh) and vertical (Rv) resistivities are modeled based on the logs acquired in the observation well. A finite difference (FD) representation of the steel casing is also incorporated in the model during the forward calculation.

The residual vertical E_z phase data in Fig. 6 is therefore the primary source of information for the saturation-related resistivity distributions in the reservoir. Clearly, a marked anisotropy (azimuthal variation) exists from the W to the E directions relative to the well. This pattern is in very good agreement with the saturation estimates provided by the reservoir simulator. Similar spatial variations are observed in the vertical E_z amplitudes while variations in the magnetic field (amplitude or phase) are much smoother and lower amplitude, though they still correlate well with estimated reservoir saturation variations. These observations are in agreement with the results of the modeling study on the same well, which concluded that the only EM field with enough signal-to-noise to map reservoir saturation variations in the reservoir was the vertical E_z[4].

Measurement Repeatability

Until now, we have evaluated the sensitivity of the surface-to-borehole CSEM data to the static distribution of reservoir resistivity around the observation well. The next step is to analyze the sensitivity of the vertical E_z measurements to the variations of the waterfront in time — time-lapse analysis.

The first objective of the project, in fact, is to detect and map the variations of the waterfront position to enable the

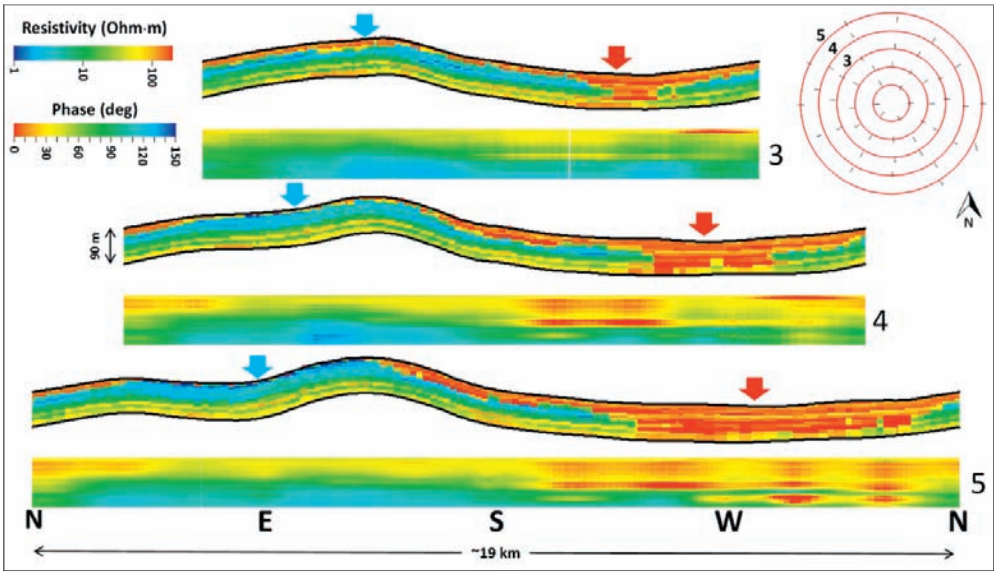

Fig. 6. Common offset phase profiles at 1,800 m, 2,400 m, and 3,000 m offsets compared to coincident profiles estimated from the reservoir simulator model. The blue and red arrows show regions of low and high resistivity, respectively.

use of this information for reservoir management decisions. Time-lapse analysis is useful for this goal because given a reliable baseline resistivity distribution, the time-related changes are occurring only in the reservoir and are unbiased by prior assumptions on saturation distributions. These observations of the waterfront movement are very important and an independent source of information that can be directly utilized in reservoir management. Effectiveness of time-lapse observations are inherently related to the amount of signal and amount of noise in the measurements that are also related to the rate of movement of the waterfront. It is therefore critical to analyze the amount of signal change produced in a certain time frame, or the time frame necessary to achieve a sufficient signal change above an estimated noise threshold.

Acquisition of a depth profile was repeated with an interval of four days from a Tx position at 2.3 km from the well. The vertical E_z profiles in terms of amplitude and phase indicate overall good repeatability of the measurements, Fig. 7, where the upper section of the well performed better — 0.3% error in log amplitude and 1.2% error in phase — than the lower interval — 0.4% error in log amplitude and 4.7% error in phase — where the caliper information indicated the presence of a washout. The wellbore rugosity may have influenced the repeated measurements by tilting of the electrode assemblage that is galvanically coupled to the borehole walls by means of metal centralizers. Verticality is a very important prerequisite

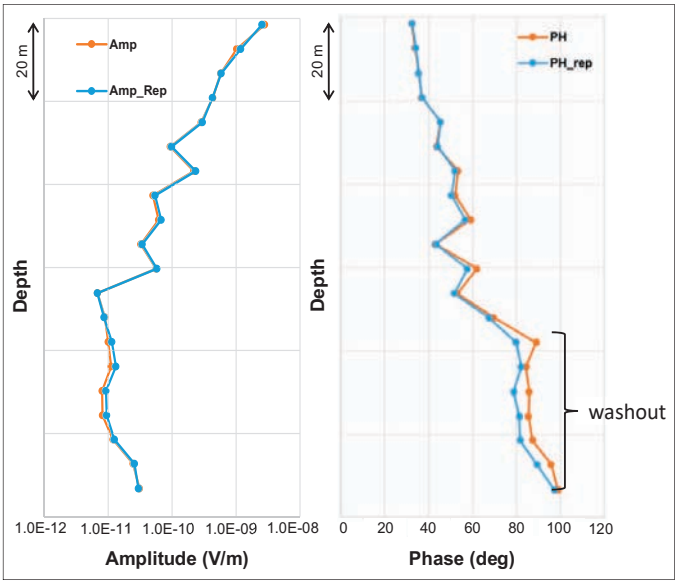

Fig. 7. Repetition of the vertical E_z depth profile from a Tx distance of 2.3 km from the well. The lower part of the well is affected by washout and shows larger repetition errors.

for vertical E_z measurements[13]. Other sources of measurement errors can be related to depth errors in the positioning of the wireline tool (currently estimated to be a few tens of cm), intrinsic instrumentation noise and possible variations in the well fluids over time. During the survey, the well fluids were slowly depleting and required repeated pumping operations. Tilting, depth errors, and fluid composition variations

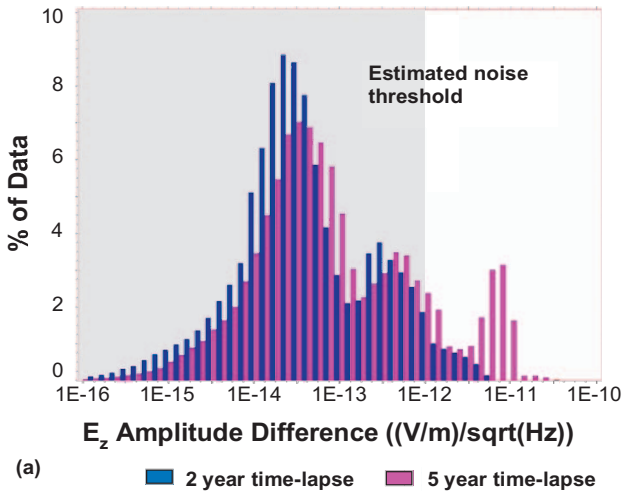

Time-lapse field strength change

Tx	Rx	2 year time-lapse	5 year time-lapse
Jx (radial)	Ex	$4x10^{-12}$ V/m	$5x10^{-12}$ V/m
	Ez	**$5x10^{-12}$ V/m**	**$3x10^{-11}$ V/m**

(b)

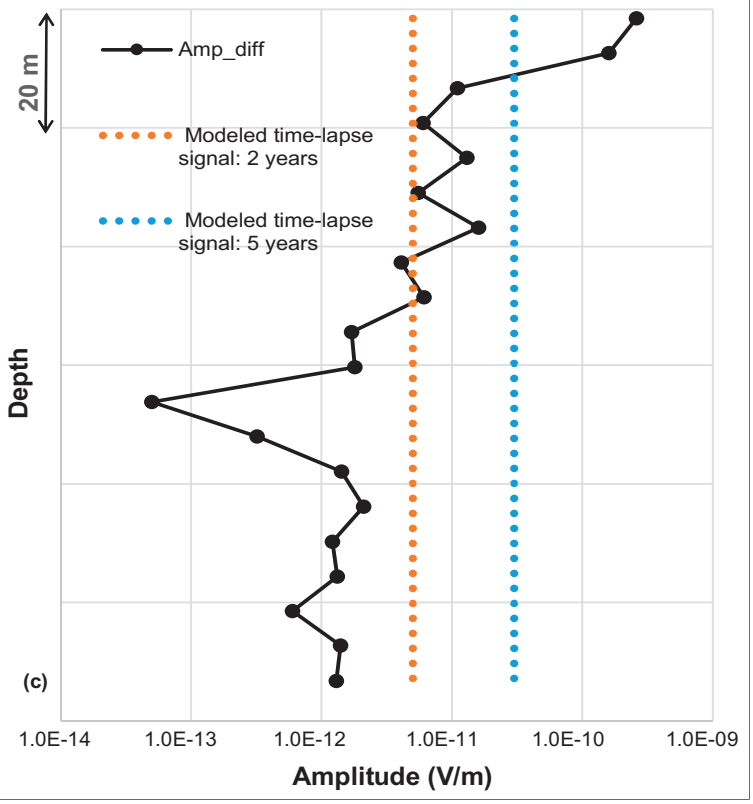

Fig. 8. Time-lapse electric field signal variations as a result of waterflooding (modeled data) vs. the vertical E_z amplitude repetition error as measured in the well: (a) histogram showing the variations of the vertical E_z signal over 2 and 5 years of waterflooding from modeling[4]; (b) maximum field strength variations; and (c) comparison between repetition error and time-lapse field strength variations.

can be modeled to obtain estimates of their impact on the measurements.

The repetition errors in the vertical E_z are then compared to the estimated signal changes estimated from reservoir simulator modeling[4]. The calculated 2-year and 5-year time-lapse vertical E_z signal, normalized by the source moment and by the receiver electrode separation, is then compared to the amplitude differences from the repeated measurements, Fig. 8. A few observations can be made. The measurement noise threshold in the Colombo and McNeice (2013)[4] study is estimated at 1E-12 V/m, Fig. 8a, which corresponds to the smallest error in the repeated measurements, Fig. 8c. The time-lapse signal due to waterflooding is estimated to be above the repetition noise after 2 years in the lower portion of the reservoir, and substantially above the time-lapse noise after 5 years, Figs. 8b and 8c, except where the measurements are influenced by the presence of casing. The repeatability analysis suggests that the time-lapse measurements should be able to provide the requested information about the waterfront evolution.

DATA INTERPRETATION WORKFLOW

Having assessed the signal-to-noise and repeatability of the surface-to-borehole measurements, we now identify the key steps to derive a robust estimate of 3D resistivity distribution. An analysis of the processing steps for data conditioning leading to the final 3D inversion is shown in Fig. 9. Some of the most important aspects in this workflow are modeling the steel casing effect and the strategies to account for it in the data. Steel casing has a strong signature on the measurement of the borehole's vertical E_z, and strategies for dealing with it range from embedding a scaled up representation of the casing directly into the model using the material property mapping theory and FD or finite element numerical methods[12, 14, 15], or by modeling and subtracting its effects from the data using semi-analytical solutions[9]. Here we have opted for a numerical representation of the casing effect modeling it by directly using a FD scheme while finite element and semi-analytical

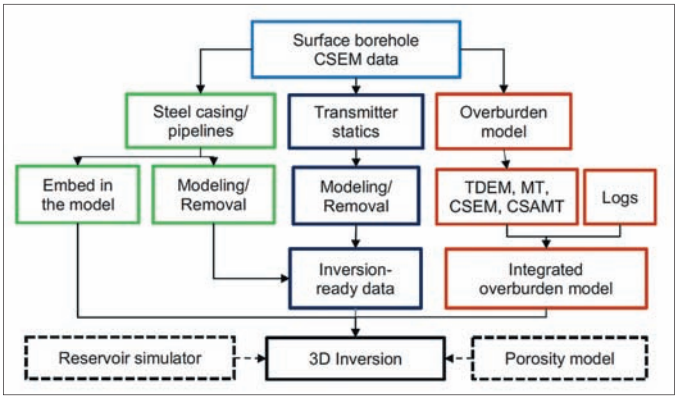

Fig. 9. Data interpretation workflow highlighting the key data conditioning and model building steps to enable robust 3D inversions of the surface-to-borehole CSEM data set.

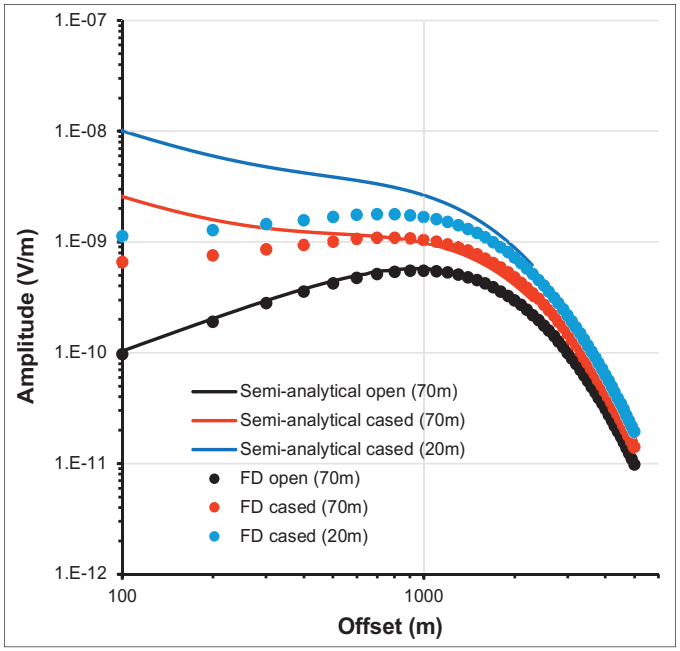

Fig. 10. Plot of the modeled CSEM amplitude for receivers at 20 m and 70 m below the casing shoe for varying Tx offset.

solutions are currently being explored. Figure 10 compares the responses of the semi-analytical solution[11] with an FD solution obtained by embedding the casing in the model. The calculation is performed for a reservoir without casing and with casing at an increasing Tx distance from the well, and for different measurement depths in the reservoir, corresponding to an increasing distance from the casing shoe. The FD approach matches perfectly with the semi-analytical solution when the casing is not present and tends to approximate the semi-analytical solution as a function of the Tx distance and depth of observation in the reservoir when the casing is considered. At -70 m from the casing shoe, the FD solution is valid for Tx offsets greater than 500 m, while at -20 m from the casing shoe, the FD response matches the semi-analytical solution only when the transmitter is beyond 2 km from the well.

Galvanic distortions can occur at the source electrode sites. These effects are described as a local accumulation of charges caused by 3D heterogeneous resistivity distributions in the near surface and typically referred to as vertical E_z "statics." Such effects are well-known in MT and land CSEM measurements, and techniques to remove them based on magnetic induction methods are described in the literature[16, 17]. The vertical E_z data measured in the borehole are well behaved showing a smooth azimuthal variation, suggesting that, if present, such galvanic distortion effects are of minor concern and could be dealt with directly in the inversion phase by solving for additional free parameters representing statics[15].

The last preparatory phase leading to the 3D inversion consists of overburden characterization. The 3D surface-to-borehole CSEM inversion problem is typically underdetermined with a much larger number of unknowns than observations. Such an inverse problem can be solved only by the introduction of constraints. The reservoir section is the target of the

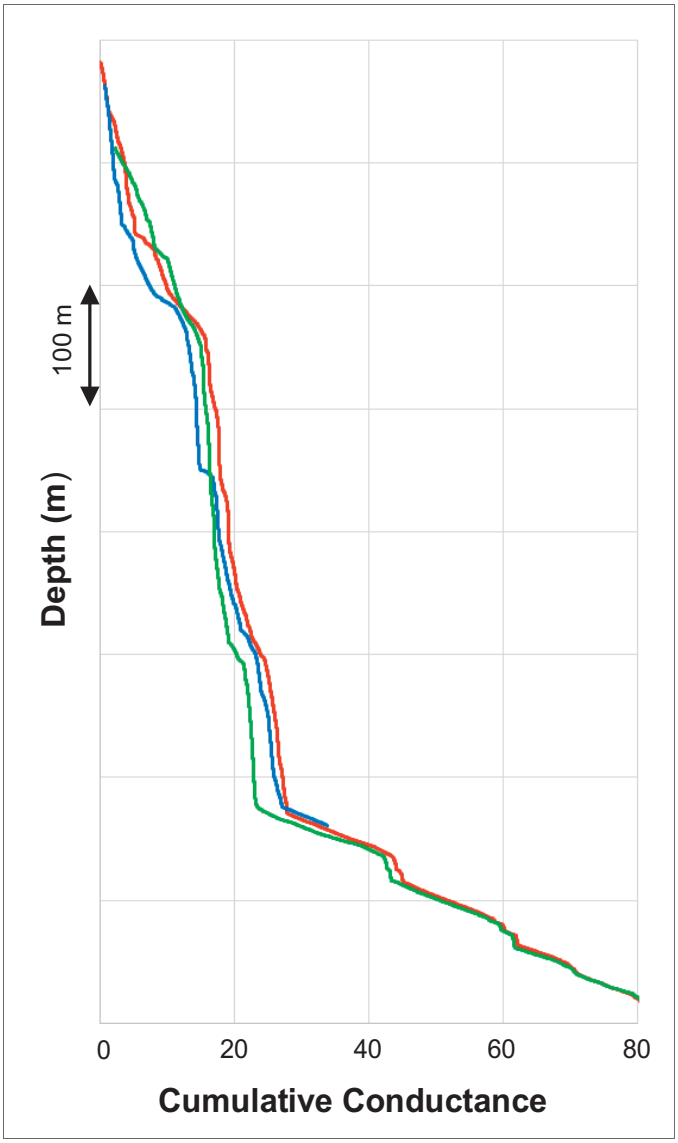

Fig. 11. Plot of the cumulative conductance for three wells in the area, including the observation well and two other wells at a distance of 1 km and 6 km.

inversion and is the part of the model that is subject to the largest resistivity variations both in static and dynamic, i.e., time-lapse, conditions due to waterflooding. The overburden is therefore the portion of the model that does not change but needs to be characterized for the static, i.e., present-day, 3D inversion to decouple it from the reservoir response.

The overburden resistivity structure is obtained from a combination of additional measurements and resistivity log analysis. A full suite of logs were acquired in the monitoring well from the surface to the reservoir comprising triaxial resistivity logs. The Rh and Rv resistivity models are obtained at the well location by an upscaling procedure, which takes into consideration both the cumulative conductance and the cumulative transverse resistance. An optimal geoelectric structure of the overburden suited for inversion is represented at the well position[4]. Analysis of the cumulative conductance for nearby wells has shown that the general geoelectric structure is fairly homogeneous for the overburden section for three wells in the area, including the observation well and for two other wells at a distance of 1 km and 6 km, Fig. 11. The overburden is therefore assumed to be laterally homogeneous, and at this stage of the inversion work, it is derived primarily from upscaling vertical and horizontal well log resistivity measurements. Future refinements of the overburden resistivity structure will be obtained from the inversion of time domain EM, MT and CSEM (surface-surface) soundings.

The steps described here have led to a first 3D inversion for the reservoir resistivity distribution that represents the baseline for future time-lapse monitoring phases. In the framework of the 3D inversion, additional work is being conducted for the introduction of external regularization methods based on rock physics and/or structure operators. The external regularization can be embedded in the inversion procedure in a Bayesian approach as reference models, spatial structure regularization operators or as rock physics operators[18].

3D INVERSION

The 3D inversion for the reservoir resistivity distribution is performed using the vertical E_z data at 8 *Hz*. A representation of the well casing is incorporated into the model using a FD scheme and material property averaging techniques as previously described. The inversion was run for a single depth of observation located 70 m below the casing shoe, which enables the use all the available Tx data from about 500 m distance to the maximum offset at 3.5 km without incurring significant errors in the approximated steel casing representation. The geometry of the layers was derived from depth conversion of the 3D time domain seismic volume using the observation well for calibrating depths and velocities to tie the formation tops. Figure 12 shows the overburden Rh resistivity derived from the lateral extrapolation of the upscaled triaxial

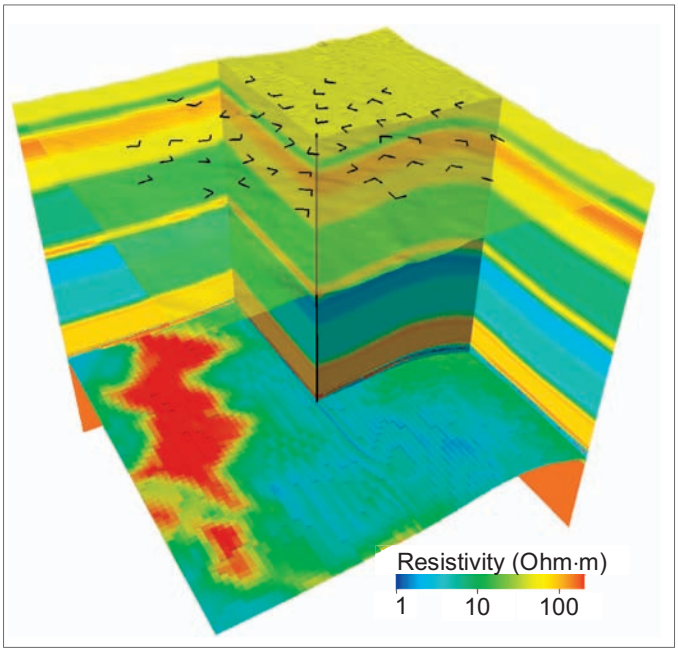

Fig. 12. Overburden resistivity structure (Rh) used for the inversion and reservoir resistivity distribution from the simulator.

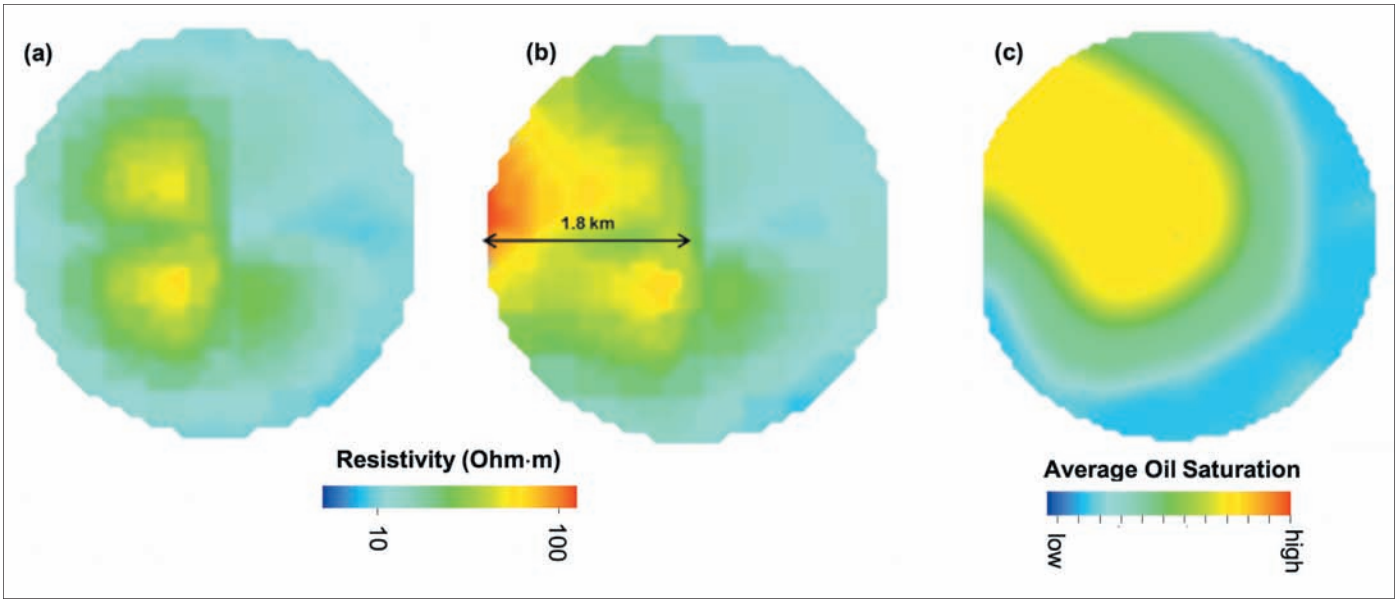

Fig. 13. 3D inversion results using the vertical E_z component: (a) resistivity distribution by starting the inversion from a uniform 10 ohm·m reservoir resistivity model; (b) inversion result by starting from a smoothed version of the reservoir simulator resistivity distribution; and (c) reference average oil saturation from C/O production logs acquired in nearby wells.

log data at the observation well. The overburden resistivity structure is then fixed during the inversion.

The starting model for the reservoir section is initially set to a constant resistivity of 10 ohm·m to test the sensitivity and stability of the inversion process without additional constraints. The 3D surface-to-borehole CSEM inversion is carried out using a FD forward modeling algorithm[19] with the nonlinear conjugate gradient method used for the minimization of the objective function[20]. Inversion results starting from the uniform 10 ohm·m reservoir resistivity distribution show a net increase in the resistivity to the western side of the well, and a decrease of the resistivity to the eastern side, Fig. 13a. Inversion results are consistent from what was already observed from spatial variations in the vertical E_z.

Repeating the inversion using a smoothed version of the reservoir simulator resistivity distribution as a starting model further extends the sensitivity of the inversion to approximately 1.8 km from the monitoring well, Fig. 13b. The consistency of the two inversion results indicates the overall robustness of the inversion procedure with little dependency on the starting model. An independent evaluation of the inversion results is provided by the average oil saturation map derived from periodic carbon-oxygen (C/O) logging measurements from nearby wells. The overall shape of the recovered anomaly from inversion is consistent with the oil saturation observations from production logs, Fig. 13c.

The quality of the inversion results can be seen from the good match between the measured data and forward calculated fields after inversion for six radial profiles crossing the monitoring well, Fig. 14, resulting in an overall root-mean-squared misfit of 1.4.

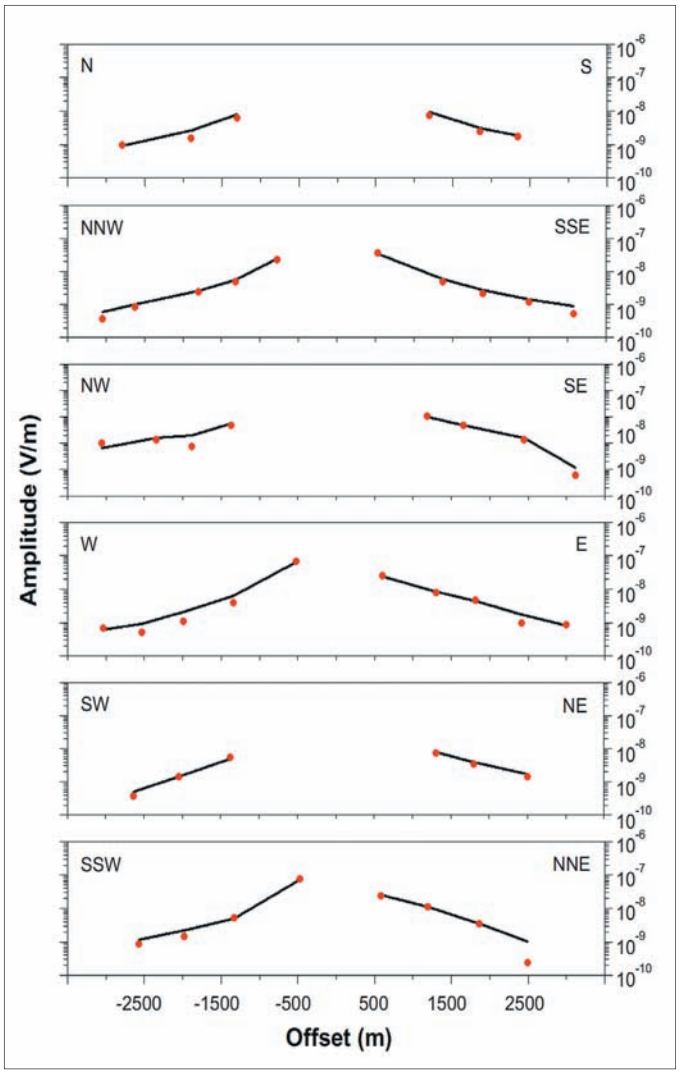

Fig. 14. Data fit for the vertical E_z amplitude (points = data; curves = modeled fields) for the six radial profiles across the monitoring well.

CONCLUSIONS

A novel surface-to-borehole CSEM technology was tested for the first time over a relatively deep reservoir in a large onshore oil field. Several new aspects characterize the project and can be summarized as follows: development of new borehole vertical E_z sensors shielded from spurious electric noise sources, development of a new powerful electric transmitter capable of producing 2,000 V and 500 amps with excellent current and phase stability for signal-to-noise enhancement through stacking, and a new design of shallow borehole surface electrodes incorporating engineering standards for the preparation of anode beds for cathodic protection. The surface electrode design was able to achieve low contact resistance — 2.1 ohm as average — in a desert environment, and minimized the impact of galvanic distortions caused by near surface heterogeneities.

Different approaches (numerical and analytical) implemented for accounting for the steel casing effects — some of the research still ongoing — proved to be effective to enable robust, 3D CSEM inversions. Static imaging of saturation-related resistivity distributions within the reservoir proved to be robust, showing little dependency on the starting model. The estimated resistivity distribution is consistent with independent saturation information derived from periodic C/O logging performed for production monitoring. Analysis of repeated measurements in the well during the surface-to-borehole CSEM survey indicates repetition errors below the expected time-lapse signal variation as predicted from modeling. The results provide positive indications for the repetition of the survey after 5 years of waterflooding, Fig. 15. Time-lapse monitoring should provide an indirect independent assessment of saturation variations to be used for reservoir management and reservoir simulator history matching purposes.

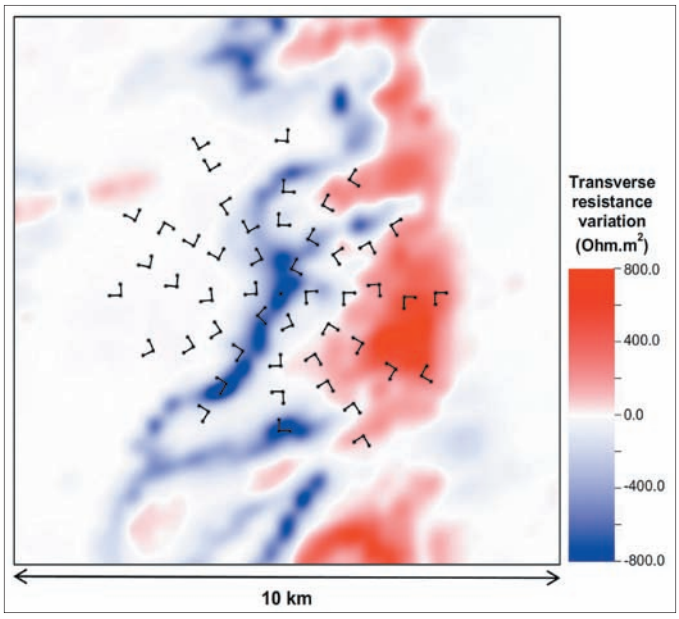

Fig. 15. Predicted change of transverse resistance over 5 years of waterflooding. The monitoring well and the surface-to-borehole acquisition setup are ideally positioned for detecting and mapping the saturation changes in the reservoir.

The surface-to-borehole CSEM pilot survey, with the technological solutions identified and the theoretical framework built around the interpretation of the data, provide very positive indications for the technology to be upscaled to a potential new oil field service, tackling the long-standing problem of waterflooding geophysical monitoring.

ACKNOWLEDGMENTS

The authors would like to thank the management of Saudi Aramco for their support and permission to publish this article.

This article was presented at the SPE Annual Technical Conference and Exhibition, Dallas, Texas, September 24-26, 2018.

REFERENCES

1. Dasgupta, S.N.: "When 4D Seismic is not Applicable: Alternative Monitoring Scenarios for the Arab-D Reservoir in the Ghawar Field," *Geophysical Prospecting*, Vol. 53, Issue 2, March 2005, pp. 215-227.
2. Blake, A., Hare, J. and MacQueen, J.: "Borehole Gravity Monitoring in the Aquistore CO_2 Sequestration Well," SEG paper 2016-13953618, presented at the SEG International Exposition and Annual Meeting, Dallas, Texas, October 16-21, 2016.
3. Colombo, D. and McNeice, G.W.: "Geophysical Monitoring of Waterflooding in Saudi Arabia: Methods and Perspectives," SEG paper 2017-17583120, presented at the SEG International Exposition and Annual Meeting, Houston, Texas, September 24-29, 2017.
4. Colombo, D. and McNeice, G.W.: "Quantifying Surface-to-Reservoir Electromagnetics for Waterflood Monitoring in a Saudi Arabian Carbonate Reservoir," *Geophysics*, Vol. 78, Issue 6, November 2013, pp. E281-E297.
5. Bakulin, A.V., Jervis, M.A., Colombo, D., Tsingas, C., et al.: "Bring Geophysics Closer to the Reservoir — New Paradigm in Reservoir Characterization and Monitoring," SEG paper 2015-5849607, presented at the SEG Annual Meeting, New Orleans, Louisiana, October 18-23, 2015.
6. Wilt, M.J., Morrison, H.F., Becker, A. and Lee, K.H.: "Cross-borehole Electromagnetic Induction for Reservoir Characterization," *SEG Technical Program Expanded Abstracts*, 1991, pp. 456-459.
7. Wilt, M.J., Alumbaugh, D.L., Morrison, H.F., Becker, A., et al.: "Crosswell Electromagnetic Tomography; System Design Considerations and Field Results," *Geophysics*, Vol. 60, Issue 3, June 1995, pp. 871-885.
8. Dogru, A.H., Fung, L.S.K., Middya, U., Al-Shaalan, T.M., et al.: "A Next-generation Parallel Reservoir Simulator for Giant Reservoirs," SPE paper 119272, presented at the SPE

Reservoir Simulation Symposium, The Woodlands, Texas, February 2-4, 2009.

9. Cuevas, N., Colombo, D., McNeice, G.W., Denaclara, H., et al.: "Field Testing and Characterization of a Transmitter-receiver System for Surface to Borehole Electromagnetic Surveys," paper presented at the 77th EAGE Conference and Exhibition, Madrid, Spain, June 1-4, 2015.
10. Wilt, M.J., Spies, B., Alumbaugh, D. and Torres-Verdin, C.: "Measurement of Surface and Borehole Electromagnetic Fields in 2D and 3D Geology," *Three-Dimensional Electromagnetics*, 1999, pp. 545-563.
11. Cuevas, N.H. and Pezzoli, M.: "On the Effect of the Metal Casing in Surface Borehole Electromagnetic Methods," *Geophysics*, Vol. 83, Issue 3, May 2018, pp. E173-E187.
12. Um, E.S., Commer, M., Newman, G.A. and Hoversten, G.M.: "Finite Element Modeling of Transient Electromagnetic Fields near Steel-cased Wells," *Geophysical Journal International*, Vol. 202, Issue 2, June 2015, pp. 901-913.
13. Streich, R.: "Controlled Source Electromagnetic Approaches for Hydrocarbon Exploration and Monitoring on Land," *Surveys in Geophysics*, Vol. 37, Issue 1, September 2015, pp. 47-80.
14. Commer, M. and Newman, G.A.: "An Accelerated Time Domain Finite Difference Simulation Scheme for Three-Dimensional Transient Electromagnetic Modeling Using Geometric Multigrid Concepts," *Radio Science*, Vol. 41, Issue 3, June 2006, pp. 1-15.
15. Commer, M. and Newman, G.A.: "New Advances in Three-Dimensional Controlled Source Electromagnetic Inversion," *Geophysical Journal International*, Vol. 172, Issue 2, February 2008, pp. 513-535.
16. Pellerin, L. and Hohmann, G.W.: "Transient Electromagnetic Inversion: A Remedy for Magnetotelluric Static Shifts," *Geophysics*, Vol. 55, Issue 9, September 1990, pp. 1242-1250.
17. Newman, G.A.: "Deep Transient Electromagnetic Soundings with a Grounded Source over near Surface Conductors," *Geophysical Journal International*, Vol. 98, Issue 3, September 1989, pp. 587-601.
18. Colombo, D. and Rovetta, D.: "Coupling Strategies in Multiparameter Geophysical Joint Inversion," *Geophysical Journal International*, Vol. 215, Issue 2, January 2018, pp. 1171-1184.
19. Alumbaugh, D.L., Newman, G.A., Prevost, L. and Shadid, J.N.: "Three-dimensional Wideband Electromagnetic Modeling on Massively Parallel Computers," *Radio Science*, Vol. 31, Issue 1, 1996, pp. 1-23.
20. Newman, G.A. and Alumbaugh, D.L.: "Three-dimensional Magnetotelluric Inversion Using Nonlinear Conjugate Gradients," *Geophysical Journal International*, Vol. 140, Issue 2, February 2000, pp. 410-424.

BIOGRAPHIES

Dr. Daniele Colombo is a Senior Geophysical Consultant and the Champion of Reservoir Multiphysics Technology working in the Geophysics Technology Division of Saudi Aramco's Exploration and Petroleum Engineering Center – Advanced Research Center (EXPEC ARC). His research interests include seismic and electromagnetic imaging, and multi-parameter joint inversion with application to exploration and reservoir monitoring.

Prior to joining Saudi Aramco in 2009, Daniele held various positions in service companies such as the Technical and R&D Manager for seismic imaging in complex geology, and as the Data Processing Manager for Schlumberger in Milan and Calgary, respectively. He was at the forefront of the development of multi-physics imaging and joint inversion methods for integrated seismic electromagnetic gravity velocity modeling applied to seismic depth imaging.

This research activity gained Daniele several industry recognitions and awards, including a Society of Exploration Geophysicists Honorable Mention for Best Paper in *The Leading Edge* in 2016, and also (with a team) the Saudi Aramco CEO Excellence Award in 2018 for Disruptive Technology Creation.

He published more than 70 papers on a variety of subjects, including microseismic monitoring during reservoir stimulation, multiphysics joint inversion, depth imaging in complex geology, near surface velocity and surface consistent modeling, and electromagnetic applications for reservoir fluid monitoring.

In 1994, Daniele received his Ph.D. degree in Geophysics from Milan University, Milan, Italy, followed by a postdoctoral position at the National Institute for Geophysics and Volcanology in Rome.

Gary W. McNeice is a Geophysical Consultant working in the Geophysics Technology Division of Saudi Aramco's Exploration and Petroleum Engineering Center – Advanced Research Center (EXPEC ARC).

He started his career at the Geological Survey of Canada and then went on to hold technical and management positions with electromagnetic equipment manufacturers and service providers. During this time, Gary has been one of several active participants in the improvement and development of magnetotelluric field systems and interpretation methods. In positions with Geosystem and WesternGeco, he was the primary magnetotellurics geophysicist on exploration projects throughout North America and in many countries around the world.

Gary's research interests include electromagnetic and potential field imaging, and multi-parameter earth model building through joint inversion.

In 1989, he received his B.S. degree in Geology and Physics from Carleton University, Ottawa, Ontario, Canada, and in 1998, Gary received his M.S. degree in Geophysics from Memorial University, St. John's, Newfoundland, Canada.

Dr. Nestor H. Cuevas joined Schlumberger in 2003, and currently works in a Principal position as the Area Geophysicist for Electromagnetic (EM) Methods, at the WesternGeco Geosolutions IEM Center of Excellence in Milan, Italy. In this role, he supervises the data acquisition, and processing and modeling of EM projects. Nestor also leads the development of new technologies, such as the surface borehole electromagnetics.

At the beginning of his career, he worked for Geodatos SAIC in Chile, were he performed dedicated research in the area of induced polarization in measurements of natural EM fields. In 1995, Nestor transferred to California where he worked for ElectroMagnetic Instruments Inc., participating in numerous R&D projects for the development of instrumentation, sensors and processing techniques for magnetotelluric data acquisition systems, EM measurements in the seafloor, and cross well tomography.

Nestor has published several articles in international geophysics journals and at various conferences. He is a member of the European Association of Geoscientists and Engineers (EAGE), and the Society of Exploration Geophysicists (SEG). Nestor actively participates as a reviewer for several journals: *Geophysics*, *Geophysical Prospecting* and *Geophysics Journal International*.

In 1992, he received his B.S. degree in Physics from the Universidad de Santiago, Santiago, Chile. In 2007, Nestor received his M.S. degree, and in 2009 he received his Ph.D. degree — both in Geophysics — from the University of Berkeley, Berkeley, CA, where he developed theories to describe EM sources associated to electrokinetic coupling arising in hydraulic fracture propagation.

Mauro Pezzoli began his career in 2008 when he joined Schlumberger. He is currently a Senior Geophysicist for Electromagnetic (EM) Methods at the WesternGeco Geosolutions IEM Center of Excellence in Milan, Italy. In this role, Mauro participates and manages all stages of EM related geophysical projects, from survey design through data acquisition, processing, modeling, and ultimately delivering the final interpretation of the results. He also collaborates in the research and development of new technologies, such as surface borehole electromagnetics.

Mauro has published several articles in international geophysics journals and at various conferences. He is a member of the European Association of Geoscientists and Engineers (EAGE), and the Society of Exploration Geophysicists (SEG).

In 2006, Mauro received his B.S. degree, and in 2007, he received his M.S. degree — both in Environmental Engineering — from the Politecnico di Milano, Milano, Italy.

A Year of Innovation and Progress

Kimon N. Alexandrou

Since the company's first patent in 1950, Saudi Aramco has contributed significantly to the world's innovation efforts with high-value intellectual property (IP), which has positioned the company as a leader in the energy sector.

In 2018, Saudi Aramco achieved its best year yet, with 309 granted patents from the United States Patent and Trademark Office, which put the company second among oil and gas companies worldwide in the number of patents granted for the year.

A well-developed IP portfolio supports Saudi Aramco's competitive advantage, validates the contributions made by our scientists and researchers, solidifies our position as a technology leader in the energy and chemicals fields, and provides commercialization opportunities for non-core technologies. Patents provide value to the company and the Kingdom of Saudi Arabia by enabling Saudi Aramco to deploy these technologies without the fear of competitors taking the idea and deploying the same or similar technology. To maximize value for the business, only globally competitive technologies are being developed and deployed, affording Saudi Aramco a continued leadership advantage.

Recent published research from Stanford University has found that there are vast differences in the carbon intensity of global upstream operations. Technology governance in drilling and reservoir management are at the heart of operations, sustaining the production of one of the lowest carbon intensities of a barrel of oil equivalent produced globally. At Saudi Aramco, technology is the enabler, and central to our ability to reduce greenhouse gas emissions from across our operations.

From the creation of the Master Gas System in the 1970s that has virtually eliminated flaring in Saudi Arabian oil fields, to methane reduction, to carbon capture, utilization and storage, and to fuel engine matching initiatives in transportation, innovations are making a meaningful difference below and above the ground.

For downstream, our research and development activities seek to develop and implement process improvement and production efficiencies in support of the company's growing petrochemicals business. The direct conversion of crude oil to petrochemicals is a single step process, and is both a promising and significant development that will deliver higher efficiencies in our chemicals business.

Supporting the company's commitment to creating a robust portfolio of IP, the network innovation model that facilitates strategic alliances with world-class organizations has proven successful in enabling Saudi Aramco to enhance its competitiveness, and expand its global technology footprint. These collaborations have contributed to the rise in the number of patented technologies that have been developed between Saudi Aramco and our partners, including leading technical innovators in the industry, as well as leading academic institutions in-Kingdom and around the world.

SAUDI ARAMCO PATENTS GRANTED 2018

Catalysts and Methods for Polymer Synthesis

Granted Patent: U.S. Patent 9,856,349, Grant Date: January 2, 2018

Jay J. Farmer

Header for Air Cooled Heat Exchanger

Granted Patent: U.S. Patent 9,857,127, Grant Date: January 2, 2018

Dhawi A. Al-Otaibi

Systems and Methods for Near Infrared-based Water Cut Monitoring in Multiphase Fluid Flow

Granted Patent: U.S. Patent 9,857,298, Grant Date: January 2, 2018

Muhammad Arsalan, Talha J. Ahmad, and Mohamed N. Noui-Mehidi

Cyclone Separation and Recovery of Carbon Dioxide from Heated Liquid Absorbent

Granted Patent: U.S. Patent 9,861,910, Grant Date: January 9, 2018

Ahmad D. Hammad, Abdulrahman Z. Akhras, Zaki Yusuf, Nayif A. Rasheedi, and Abdullah M. Al-Qahtani

High Temperature Fracturing Fluids with Nano-Crosslinkers

Granted Patent: U.S. Patent 9,862,878, Grant Date: January 9, 2018

Ghaithan A. Al-Muntasheri, Feng Liang, Hooisweng Ow, Jason Cox, and Martin E. Poitzsch

Chemical-based Well Kickoff System for Naturally Flowing Wells

Granted Patent: U.S. Patent 9,863,226, Grant Date: January 9, 2018

Rafael A. Lastra and Mohammed N. Noui-Mehidi

Fracturing Fluid for Subterranean Formations

Granted Patent: U.S. Patent 9,863,231, Grant Date: January 9, 2018

Katherine L. Hull, Mohammed Sayed, and Ghaithan A. Al-Muntasheri

High Efficiency Solar Power Generator for Offshore Applications

Granted Patent: U.S. Patent 9,863,404, Grant Date: January 9, 2018

Michael J. Black and Abubaker S. Saeed

Systems and Methods for Monitoring Casing Cement Integrity

Granted Patent: U.S. Patent 9,863,895, Grant Date: January 9, 2018

Shouxiang Ma, Darryl Trcka, and Robert Wilson

Modular Mobile Inspection Vehicle

Granted Patent: U.S. Patent 9,863,919, Grant Date: January 9, 2018

Pablo Carrasco Zanini, Ali Outa, Fadl H. Abdel Latif, Brian J. Parrott, Hassane Trigui, Sahejad Patel, and Ayman Amer

Aliphatic Polycarbonate Quench Method

Granted Patent: U.S. Patent 9,868,816, Grant Date: January 16, 2018

Jeffrey R. Conuel, David E. Decker, Scott D. Allen, and Anna E. Cherian

Integrated Hydrotreating and Isomerization System with Aromatic Separation

Granted Patent: U.S. Patent 9,868,914, Grant Date: January 16, 2018

Omer R. Koseoglu

Scissor-Mechanism Closing Rams of Blow Out Preventers

Granted Patent: U.S. Patent 9,869,149, Grant Date: January 16, 2018

Mohammad S. Al-Badran

Kalina Cycle-based Conversion of Gas Processing Plant Waste Heat into Power

Granted Patent: U.S. Patent 9,869,209, Grant Date: January 16, 2018

Mohammad S. Al-Badran

Nano-Level Evaluation of Kerogen-Rich Reservoir Rock

Granted Patent: U.S. Patent 9,869,649, Grant Date: January 16, 2018

Katherine L. Hull, Younane N. Abousleiman, and Sebastian Csutak

Method for Non-Intrusive Measurement of Low Water Content in Oil

Granted Patent: U.S. Patent 9,869,664, Grant Date: January 16, 2018

Ezzat M. Hegazi and Abdul-Rahman Z. Akhras

Dual-Phase Acid-based Fracturing Composition with Corrosion Inhibitors and Method of Use Thereof

Granted Patent: U.S. Patent 9,873,829, Grant Date: January 23, 2018

Saleh H. Al-Mutairi, Yaser K. Al-Duailej, Ibrahim S. Al-Yami, Abdullah M. Al-Hajri, and Hameed Al-Badairy

Reversible Aminal Gel Compositions, Methods, and Use

Granted Patent: U.S. Patent 9,879,170, Grant Date: January 30, 2018

Peter J. Boul, B. Raghava Reddy, Matthew Hilfiger, and Carl J. Thaemlitz

Integrated Ebullated Bed Hydroprocessing, Fixed Bed Hydroprocessing and Coking Process for Whole Crude Oil Conversion into Hydrotreated Distillates and Petroleum Green Coke

Granted Patent: U.S. Patent 9,879,188, Grant Date: January 30, 2018

Omer R. Koseoglu

Recovery and Re-Use of Waste Energy in Industrial Facilities

Granted Patent: U.S. Patent 9,879,918, Grant Date: January 30, 2018

Mahmoud B. Noureldin and Hani M. Al-Saed

Dual Catalyst System for Propylene Production

Granted Patent: U.S. Patent 9,884,794, Grant Date: February 6, 2018

Sulaiman S. Al-Khattaf, Arudra Palani, Tazul I. Bhuiyan, Mohammad N. Akhtar, Abdullah M. Aitani, Mohammed A. Al-Yami, and Sohel Shaikh

Polymer Compositions and Methods

Granted Patent: U.S. Patent 9,884,937, Grant Date: February 6, 2018

Wayne R. Willkomm and Scott D. Allen

Cement Oil-based Mud Spacer Formulation

Granted Patent: U.S. Patent 9,884,985, Grant Date: February 6, 2018

Mohammad L. Al-Subhi, Ahmad S. Al-Humaidi, and Scott S. Jennings

Systems, Protective Casings for Smartphones, and Associated Methods to Enhance Use of an Automated External Defibrillator (AED) Device

Granted Patent: U.S. Patent 9,889,311, Grant Date: February 13, 2018

Samantha J. Horseman and Curtis Gonter

Solid Base Catalyst Compositions Useful in Removal of Oxidized Sulfur Compounds and Method for Making Solid Base Catalyst Compositions

Granted Patent: U.S. Patent 9,889,430, Grant Date: February 13, 2018

Omer R. Koseoglu and Abdennour Bourane

Systems, Computer Medium and Computer Implemented Methods for Logging Using a Logging Tool with Adjustable Detectors

Granted Patent: U.S. Patent 9,890,632, Grant Date: February 13, 2018,

Shouxiang Ma, Ali R. Belowi, and Darryl Trcka

Recovery and Re-Use of Waste Energy in Industrial Facilities

Granted Patent: U.S. Patent 9,891,004, Grant Date: February 13, 2018

Mahmoud B. Noureldin and Hani M. Al-Saed

Stand-alone Portable Sensing System for Advanced Nanoparticle Tracers

Granted Patent: U.S. Patent 9,891,170, Grant Date: February 13, 2018

Erika S. Ellis

Highly Selective Polynorbornene Homopolymer Membranes for Natural Gas Upgrading

Granted Patent: U.S. Patent 9,896,527, Grant Date: February 20, 2018

Benjamin J. Sundell and John A. Lawrence

Processes and Systems for Fluidized Catalytic Cracking

Granted Patent: U.S. Patent 9,896,627, Grant Date: February 20, 2018

Omer R. Koseoglu

Integrated Process to Produce Asphalt, Petroleum Green Coke, and Liquid and Gas Coking Unit Products

Granted Patent: U.S. Patent 9,896,629, Grant Date: February 20, 2018

Omer R. Koseoglu

Inflow Control System for Use in a Wellbore

Granted Patent: U.S. Patent 9,896,905, Grant Date: February 20, 2018

Mohamed N. Noui-Mehidi

Using Radio Waves to Fracture Rocks in a Hydrocarbon Reservoir

Granted Patent: U.S. Patent 9,896,919, Grant Date: February 20, 2018

Jin-Hong Chen, Daniel T. Georgi, and Hui-Hai Liu

Three-Dimensional Reservoir Pressure Determination Using Real Time Pressure Data from Downhole Gauges

Granted Patent: U.S. Patent 9,896,930, Grant Date: February 20, 2018

Omar A. Al-Nahdi, Sami A. Al-Nuaim, Alan L. Siu, and Ahmad T. Al-Shammari

Variable Capacity Multiple-Leg Packed Separation Column System and Method of Operation

Granted Patent: U.S. Patent 9,901,868, Grant Date: February 27, 2018

Samusideen Salu and Talal A. Zahrani

Liquid Phase Oxidation of Aromatic Feedstocks with Manganate Recycling to Produce Carboxylic Acids

Granted Patent: U.S. Patent 9,902,677, Grant Date: February 27, 2018

Veera V. Tammana, Kareemuddin M. Shaik, and Guillaume R. Raynel

Multi-Objective Coreflood Test System for Oil Recovery Evaluation

Granted Patent: U.S. Patent 9,903,826, Grant Date: February 27, 2018

Amar J. Alshehri and Anthony R. Kovscek

Apparatus, Computer Readable Medium, and Program Code for Evaluating Rock Properties while Drilling Using Downhole Acoustic Sensors and Telemetry System

Granted Patent: U.S. Patent 9,903,974, Grant Date: February 27, 2018

Yunlai X. Yang

Integrated Process for Producing Anode Grade Coke

Granted Patent: U.S. Patent 9,909,068, Grant Date: March 6, 2018

Omer R. Koseoglu

Integrated Process for in Situ Organic Peroxide Production and Oxidative Heteroatom Conversion

Granted Patent: U.S. Patent 9,909,074, Grant Date: March 6, 2018

Omer R. Koseoglu and Abdennour Bourane

Staged Chemical Looping Process with Integrated Oxygen Generation

Granted Patent: U.S. Patent 9,909,756, Grant Date: March 6, 2018

Tidjani Niass and Mourad V. Younes

Process to Upgrade and Desulfurize Crude Oil by Supercritical Water

Granted Patent: U.S. Patent 9,914,885, Grant Date: March 13, 2018

Ki-Hyouk Choi, Joo-Hyeng Lee, and Mohammad S. Garhoush

Integrated Pump and Compressor and Method of Producing Multiphase Well Fluid Downhole and at Surface

Granted Patent: U.S. Patent 9,915,134, Grant Date: March 13, 2018

Jinjiang Xiao and Randall Shepler

Recovery and Re-Use of Waste Energy in Industrial Facilities

Granted Patent: U.S. Patent 9,915,477, Grant Date: March 13, 2018

Mahmoud B. Noureldin and Hani M. Al-Saed

Supercritical Reactor Systems and Processes for Petroleum Upgrading

Granted Patent: U.S. Patent 9,920,258, Grant Date: March 20, 2018

Ki-Hyouk Choi, Abdullah T. Alabdulhadi, and Mohammed A. Alabdullah

Selective Series-Flow Hydroprocessing System

Granted Patent: U.S. Patent 9,920,265, Grant Date: March 20, 2018

Omer R. Koseoglu

Method to Remove Metals from Petroleum

Granted Patent: U.S. Patent 9,926,467, Grant Date: March 27, 2018

Ki-Hyouk Choi, Emad N. Al-Shafei, Ashok K. Punetha, Joo-Hyeong Lee, and Mohammad A. Al-Abdullah

Compositions with Polyaziridine Crosslinkers for Treating Subterranean Formations

Granted Patent: U.S. Patent 9,932,512, Grant Date: April 3, 2018

Matthew Hilfiger and B. Raghava Reddy

High Power Laser-Fluid Guided Beam for Open Hole Oriented Fracturing

Granted Patent: U.S. Patent 9,932,803, Grant Date: April 3, 2018

Sameeh I. Batarseh and Hazim H. Abass

Method for Decarbonization of a Fuel on Board a Vehicle

Granted Patent: U.S. Patent 9,937,458, Grant Date: April 10, 2018

Ali M. Al-Dawood and Fahad I. Al-Muhaish

Lightweight Foam Concrete

Granted Patent: U.S. Patent 9,938,199, Grant Date: April 10, 2018

Mohammed H. Al-Mehthel, Mohammed Maslehuddin, Saleh Al-Idi, and Mohammed Shameem

Detecting Gas in a Wellbore Fluid

Granted Patent: U.S. Patent 9,938,820, Grant Date: April 10, 2018

Clovis S. Bonavides, Denis P. Schmitt, and Mohd Azizi Ibrahim

Apparatus, Method and System for Detecting Salt in a Hydrocarbon Fluid

Granted Patent: U.S. Patent 9,939,405, Grant Date: April 10, 2018

Naim Akmal, Rashed M. Aleisa, and Milind M. Vaidya

Evaluating Effectiveness of Ceramic Materials for Hydrocarbons Recovery

Granted Patent: U.S. Patent 9,939,421, Grant Date: April 10, 2018

Sameeh I. Batarseh, Hazim H. Abass, and Ayman R. Al Nakhli

Systems, Methods, and Computer Medium to Produce Efficient, Consistent, and High Confidence Image-based Electrofacies Analysis in Stratigraphic Interpretations Across Multiple Wells

Granted Patent: U.S. Patent 9,939,548, Grant Date: April 10, 2018

Gordon Burmester and Keith A. Macpherson

Enhancement of Claus Tail Gas Treatment with Membrane and Reducing Step

Granted Patent: U.S. Patent 9,943,802, Grant Date: April 17, 2018

Feras Hamad, Milind M. Vaidya, Jean-Pierre Ballaguet, Sebastien A. Duval, and Iran D. Charry-Prada

Method for Reducing Fluid Loss during Drilling of a Hydrocarbon Formation Using a Water-based Drilling Fluid Composition Having a Multifunctional Mud Additive

Granted Patent: U.S. Patent 9,944,841, Grant Date: April 17, 2018

Md. Amanullah and Mohammed K. Al-Arfaj

Stage Cementing Tool and Method

Granted Patent: U.S. Patent 9,945,206, Grant Date: April 17, 2018

Shaohua Zhou

System for Monitoring Employee Health

Granted Patent: U.S. Patent 9,949,640, Grant Date: April 24, 2018

Samantha J. Horseman

Catalysts and Methods for Polymer Synthesis

Granted Patent: U.S. Patent 9,951,096, Grant Date: April 24, 2018

Geoffrey W. Coates, Robert E. Lapointe, Chris A. Simoneau, Scott D. Allen, Anna E. Cherian, Jay J. Farmer, and Alexei A. Gridnev

Petroleum Upgrading and Desulfurizing Process

Granted Patent: U.S. Patent 9,951,283, Grant Date: April 24, 2018

Ki-Hyouk Choi and Mohammad F. Al-Jishi

Methods for Co-Processing Carbon Dioxide and Hydrogen Sulfide

Granted Patent: U.S. Patent 9,951,430, Grant Date: April 24, 2018

Stamatios Souentie, Alberto L. Ballesteros, and Fritz Simeon

Fluid Homogenizer System for Gas Segregated Liquid Hydrocarbon Wells and Method of Homogenizing Liquids Produced by Such Wells

Granted Patent: U.S. Patent 9,951,598, Grant Date: April 24, 2018

Brian A. Roth and Rafael A. Lastra

Integrated Calcium Looping Combined Cycle for Sour Gas Applications

Granted Patent: U.S. Patent 9,951,689, Grant Date: April 24, 2018

Mourad Younes, Ali Hoteit, and Aqil Jamal

Preparation and Use of Drilling Fluids with Date Seed Powder Fluid Loss Additive

Granted Patent: U.S. Patent 9,957,433, Grant Date: May 1, 2018

Md. Amanullah, Jothibasu Ramasamy, Turki Alsubaie, and Omar Fuwaires

Petroleum Upgrading Process

Granted Patent: U.S. Patent 9,957,450, Grant Date: May 1, 2018

Ki-Hyouk Choi, Ashok K. Punetha, Mohammed R. Al-Dossary, and Sameer A. Al-Ghamdi

Two-Step Process for Aromatics Production from Natural Gas/ Shale Gas Condensates

Granted Patent: U.S. Patent 9,957,451, Grant Date: May 1, 2018

Raed Abudawoud

Adjusting a Fuel On-Board a Vehicle

Granted Patent: U.S. Patent 9,957,903, Grant Date: May 1, 2018

Esam Z. Hamad and Ibrahim M. Al-Gunaibet

Line Blind Valve Assembly Having an Injection Sealing System

Granted Patent: U.S. Patent 9,958,072, Grant Date: May 1, 2018

Omar M. Al-Amri

Machines for Reservoir Simulation with Automated Well Completions and Reservoir Grid Data Quality Assurance

Granted Patent: U.S. Patent 9,958,571, Grant Date: May 1, 2018

Mohammed S. Al-Nuaim, Omar A. Al-Nahdi, Khalid A. Al-Nasser, Keyang Dai, Tareq Al-Zahrani, Khalid Al-Alwan, and Muath Al-Mulla

Systems, Computer Medium and Computer Implemented Methods for Monitoring and Improving Biomechanical Health of Employees

Granted Patent: U.S. Patent 9,962,083, Grant Date: May 8, 2018

Samantha J. Horseman

Sour Gas Feed Separations and Helium Recovery from Natural Gas Using Block Co-Polyimide Membranes

Granted Patent: U.S. Patent 9,962,646, Grant Date: May 8, 2018

Yahaya Garba, Ahmed Bahamdan, Feras Hamad, Mohammad S. Al-Qahtani, Ahmed Ameen, and Abdulaziz Y. Al-Ammar

Gas Separation Membrane Module for Reactive Gas Service

Granted Patent: U.S. Patent 9,962,659, Grant Date: May 8, 2018

Sudhir S. Kulkarni, Karl S. Beers, Jean-Pierre R. Ballaguet, Milind M. Vaidya, and Sebastien A. Duval

Composition for Enhanced Fracture Cleanup Using Redox Treatment

Granted Patent: U.S. Patent 9,963,631, Grant Date: May 8, 2018

Ayman R. Nakhli, Hazim H. Abass, and Ahmed S. Otaibi

Method to Optimize Crude Slate for Optimum Hydrodesulfurization Performance

Granted Patent: U.S. Patent 9,963,647, Grant Date: May 8, 2018

Omer R. Koseoglu

Caliper Steerable Tool for Lateral Sensing and Accessing

Granted Patent: U.S. Patent 9,963,954, Grant Date: May 8, 2018

Abdulrahman A. Al-Mulhem

Methods for Processing Fumed Metallic Oxides

Granted Patent: U.S. Patent 9,969,621, Grant Date: May 15, 2018

Michele L. Ostraat

Catalyst Composition and a Process for Making Ultra High Molecular Weight Poly (Alpha-Olefin) Drag Reducing Agents

Granted Patent: U.S. Patent 9,969,826, Grant Date: May 15, 2018

Muhammed Atiqullah, Abdel S. Al-Sarkhi, Faisal M. Al-Thenayan, Abdullah R. Al-Malki, Wei Xu, and Anwar Hossaen

Measuring Tensile Strength of Tight Rock Using Electromagnetic Heating

Granted Patent: U.S. Patent 9,970,852, Grant Date: May 15, 2018

Jin-Hong Chen, Daniel T. Georgi, Lorne Davis, and Hui-Hai Liu

Apparatus, Method and System for Detecting Salt in a Hydrocarbon Fluid

Granted Patent: U.S. Patent 9,970,895, Grant Date: May 15, 2018

Naim Akmal, Rashed M. Aleisa, and Milind M. Vaidya

Solar System Comprising Self-Sustainable Condensation, Water Collection, and Cleaning Subassemblies

Granted Patent: U.S. Patent 9,973,141, Grant Date: May 15, 2018

Ahmad Hammad, Stamatios Souentie, and Zaki Yusuf

Rock Formation Drill Bit Assembly with Electrodes

Granted Patent: U.S. Patent 9,976,352, Grant Date: May 22, 2018

Scott Fraser and Ben Bamford

Hydraulically Assisted Deployed ESP System

Granted Patent: U.S. Patent 9,976,392, Grant Date: May 22, 2018

Rafael A. Lastra and Abubaker Saeed

Sulfur Recovery Process for Treating Low to Medium Mole Percent Hydrogen Sulfide Gas Feeds with BTEX in a Claus Unit

Granted Patent: U.S. Patent 9,981,848, Grant Date: May 29, 2018

Jean-Pierre R. Ballaguet, Milind M. Vaidya, Sebastien A. Duval, Aadesh Harale, Anwar H. Khawajah, and Veera Venkata R. Tammana

Processes for High Severity Fluid Catalytic Cracking Systems

Granted Patent: U.S. Patent 9,981,888, Grant Date: May 29, 2018

Mansour Al-Herz, Nathan D. Hould, Ahmed Al-Asseel, Wala Algozeeb, and Muased S. Al-Ghrami

Flow Meter Well Tool

Granted Patent: U.S. Patent 9,982,519, Grant Date: May 29, 2018

Rafael A. Lastra

Monitoring of Reservoir Fluid Moving Along Flow Pathways in a Producing Oil Field Using Passive Seismic Emissions

Granted Patent: U.S. Patent 9,982,535, Grant Date: May 29, 2018

Shivaji N. Dasgupta and Saleh Ruwaily

Determining Rock Properties

Granted Patent: U.S. Patent 9,983,106, Grant Date: May 29, 2018

Hui-Hai Liu, Bitao Lai, Hui Li, and Yanhui Han

Monitoring Hydrocarbon Reservoirs Using Induced Polarization Effect

Granted Patent: U.S. Patent 9,983,328, Grant Date: May 29, 2018

Alberto F. Marsala, Michael S. Zhdanov, and Vladimir Burtman

Determining the Quality of Data Gathered in a Wellbore in a Subterranean Formation

Granted Patent: U.S. Patent 9,988,902, Grant Date: June 5, 2018

Mark Proett and Sami Eyuboglu

Flow Data Acquisition and Telemetry Processing Systems

Granted Patent: U.S. Patent 9,989,387, Grant Date: June 5, 2018

Michael J. Black, Mohamed N. Noui-Mehidi, and Talha J. Ahmad

Methods for Evaluating Rock Properties while Drilling Using Drilling Rig Mounted Acoustic Sensors

Granted Patent: U.S. Patent 9,989,661, Grant Date: June 5, 2018

Yunlai Yang and Yi Luo

Split Range Control Using Proportional Integral Control with Flow Valves

Granted Patent: U.S. Patent 9,989,956, Grant Date: June 5, 2018

Rohit Patwardhan

Polycarbonate Block Copolymers

Granted Patent: U.S. Patent 9,994,760, Grant Date: June 12, 2018

David M. Hatfield, John W. Stevens, Scott D. Allen, John M. Salladay, and Chris A. Simoneau

Integrated Enhanced Solvent Deasphalting and Coking Process to Produce Petroleum Green Coke

Granted Patent: U.S. Patent 9,994,780, Grant Date: June 12, 2018

Omer R. Koseoglu

Permeable Lost Circulation Drilling Liner

Granted Patent: U.S. Patent 9,995,108, Grant Date: June 12, 2018

John T. Allen and Brett Bouldin

Flowing Fracturing Fluids to Subterranean Zones

Granted Patent: U.S. Patent 9,995,120, Grant Date: June 12, 2018

Ayman R. Nakhli and Abeer M. Olayan

Systems and Methods for Constructing and Testing Composite Photonic Structures

Granted Patent: U.S. Patent 9,995,690, Grant Date: June 12, 2018

Enrico Bovero, Abdullah A. Al-Shahrani, and Abdullah S. Al-Ghamdi

Smart Water Flooding Processes for Increasing Hydrocarbon Recovery

Granted Patent: U.S. Patent 10,000,687, Grant Date: June 19, 2018

Ali Alyousef and Subhash Ayirala

Claus Process for Sulfur Recovery with Intermediate Water Vapor Removal by Adsorption

Granted Patent: U.S. Patent 10,005,666, Grant Date: June 26, 2018

Cemal Ercan, Rashid M. Othman, and Yuguo Wang

Propylene Production Using a Mesoporous Silica Foam Metathesis Catalyst

Granted Patent: U.S. Patent 10,005,703, Grant Date: June 26, 2018

Raed Abudawoud, Sulaiman S. Al-Khattaf, Arudra Palani, Tazul I. Bhuiyan, Mohammad N. Akhtar, Abdullah M. Aitani, and Mohammed A. Al-Yami

Pendant Epoxide Polymers and Methods of Treating Subterranean Formations

Granted Patent: U.S. Patent 10,005,930, Grant Date: June 26, 2018

B. Raghava Reddy

System and Method for Fueling Alternative Fuel Vehicles

Granted Patent: U.S. Patent 10,008,730, Grant Date: June 26, 2018

Aqil Jamal and Thang V. Pham

Process to Upgrade Highly Waxy Crude Oil by Hot Pressurized Water

Granted Patent: U.S. Patent 10,010,839, Grant Date: July 3, 2018

Ki-Hyouk Choi, Khalid A. Al-Majnouni, and Ali Al-Shareef

Synthesis of Catalytic Materials for Metathesis and Isomerization Reactions and Other Catalytic Applications via Well Controlled Aerosol Processing

Granted Patent: U.S. Patent 10,010,870, Grant Date: July 3, 2018

Michele L. Ostraat and Brian S. Hanna

Polymer Enhanced Surfactant Flooding for Permeable Carbonates

Granted Patent: U.S. Patent 10,011,760, Grant Date: July 3, 2018

Ming Han, Ali A. Al-Yousif, Alhasan Fuseni, and Salah H. Al-Saleh

Process for Reducing the Sulfur Content from Oxidized Sulfur Containing Hydrocarbons

Granted Patent: U.S. Patent 10,011,782, Grant Date: July 3, 2018

Omer R. Koseoglu, Abdennour Bourane, and Adnan Al-Hajji

Integrated Slurry Hydroprocessing and Steam Pyrolysis of Crude Oil to Produce Petrochemicals

Granted Patent: U.S. Patent 10,011,788, Grant Date: July 3, 2018

Essam Sayed, Raheel Shafi, Abdul R.Z. Akhras, Abdennour Bourane, and Ibrahim A. Abba

Supercritical Water Processes for Upgrading a Petroleum-based Composition while Decreasing Plugging

Granted Patent: U.S. Patent 10,011,790, Grant Date: July 3, 2018

Ki-Hyouk Choi, Joo-Hyeong Lee, Muneef F. Al-Qarzouh, Bader M. Al-Otaibi, and Abdullah T. Al-Abdulhadi

Deployment Mechanism for Passive Normalization of a Probe Relative to a Surface

Granted Patent: U.S. Patent 10,012,618, Grant Date: July 3, 2018

Pablo Carrasco Zanini, Shigeo Hirose, Michele Guanieri, Paulo Debenest, Fadl H. Abdel Latif, and Sahejad Patel

System and Method for Generating Power and Enhanced Oil Recovery

Granted Patent: U.S. Patent 10,014,541, Grant Date: July 3, 2018

Aqil Jamal, Thang V. Pham, and Aadesh Harale

Gas Separation Membrane Module for Reactive Gas Service

Granted Patent: U.S. Patent 10,016,728, Grant Date: July 10, 2018

Sudhir S. Kulkarni, Karl S. Beers, Jean-Pierre R. Ballaguet, Milind M. Vaidya, and Sebastien A. Duval

Integrated Hydrotreating and Steam Pyrolysis System for Direct Processing of a Crude Oil

Granted Patent: U.S. Patent 10,017,704, Grant Date: July 10, 2018

Raheel Shafi, Julio Hasselmeyer, Abdennour Bourane, Ibrahim A. Abba, and Abdul R.Z. Akhras

Fast-Setting Retrievable Slim-Hole Test Packer and Method of Use

Granted Patent: U.S. Patent 10,018,039, Grant Date: July 10, 2018

Shaohua Zhou

Peristaltic Submersible Pump

Granted Patent: U.S. Patent 10,018,193, Grant Date: July 10, 2018

Rafael A. Lastra

Inline Density and Fluorescence Spectrometry Meter

Granted Patent: U.S. Patent 10,018,748, Grant Date: July 10, 2018

Michael J. Black, Talha J. Ahmad, and Mohamed N. Noui-Mehidi

Adaptive Optics for Imaging through Highly Scattering Media in Oil Reservoir Applications

Granted Patent: U.S. Patent 10,018,817, Grant Date: July 10, 2018

Thomas Bifano, Shannon L. Eichmann, Bennett B. Goldberg, Mazen Y. Kanj, Hari P. Paudel, and William Shain

Silicone Rubber Foam Brush

Granted Patent: U.S. Patent 10,020,775, Grant Date: July 10, 2018

Pablo Carrasco Zanini, Brian J. Parrott, and Ali Alshehri

Ethylene Oligomerization Process

Granted Patent: U.S. Patent 10,022,698, Grant Date: July 17, 2018

Kareemuddin Shaik and Wei Xu

Rapidly Dehydrating Lost Circulation Material (LCM)

Granted Patent: U.S. Patent 10,023,781, Grant Date: July 17, 2018

Md. Amanullah

Integrated Gas Oil Separation Plant for Crude Oil and Natural Gas Processing

Granted Patent: U.S. Patent 10,023,811, Grant Date: July 17, 2018

Mohamed Soliman, Samusideen Salu, Talal Al-Zahrani, and Nisar Ansari

Method and Apparatus for Sealing an Undesirable Formation Zone in the Wall of a Wellbore

Granted Patent: U.S. Patent 10,030,467, Grant Date: July 24, 2018

Al-Waleed A. Al-Gouhi

Well Testing through a Generated Exothermic Reaction in the Wellbore

Granted Patent: U.S. Patent 10,030,492, Grant Date: July 24, 2018

Ayman R. Nakhli, Hazim H. Abass, and Mirajuddin R. Khan

Systems, Methods, and Computer Medium to Provide Entropy-based Characterization of Multiphase Flow

Granted Patent: U.S. Patent 10,030,511, Grant Date: July 24, 2018

Talha J. Ahmad, Michael J. Black, Muhammad Arsalan, and Mohamed N. Noui-Mehidi

Systems, Methods, and Computer Medium to Provide Entropy-based Characterization of Multiphase Flow

Granted Patent: U.S. Patent 10,030,512, Grant Date: July 24, 2018

Talha J. Ahmad, Michael J. Black, Muhammad Arsalan, and Mohamed N. Noui-Mehidi

Characterization of an API Gravity Value of Crude Oil by Ultraviolet Visible Spectroscopy

Granted Patent: U.S. Patent 10,031,121, Grant Date: July 24, 2018

Omer R. Koseoglu, Adnan Al-Hajji, and Gordon Jamieson

Process for Maximizing Xylenes Production from Heavy Aromatics for Use Therein

Granted Patent: U.S. Patent 10,035,742, Grant Date: July 31, 2018

Raed Abudawoud, Zhonglin Zhang, Qi Xu, and Ahmad A. Jazzar

Process for Oxidative Desulfurization and Sulfone Management by Gasification

Granted Patent: U.S. Patent 10,035,960, Grant Date: July 31, 2018

Abdennour Bourane, Omer R. Koseoglu, and Stephane C. Kressmann

Apparatus, Computer Readable Medium, and Program Code for Evaluating Rock Properties while Drilling Using Downhole Acoustic Sensors and a Downhole Broadband Transmitting System

Grant Patent: U.S. Patent 10,036,246, Grant Date: July 31, 2018

Yunlai X. Yang

System and Method for Controlling Access to a Plant Network

Granted Patent: U.S. Patent 10,038,670, Grant Date: July 31, 2018

Fouad M. Al-Khabbaz, Zakarya A. Abu Al Saud, Saad A. Al-Harbi, Osama R. Al-Khunaizi, and Hussain A. Al-Salem

Synthesis of Substituted Salicylaldehyde Derivatives

Granted Patent: U.S. Patent 10,040,800, Grant Date: August 7, 2018

Jay J. Farmer and Gabriel E. Job

Two-Step Process for Production of Ron-Enhanced Mixed Butanols and Diisobutenes

Granted Patent: U.S. Patent 10,041,016, Grant Date: August 7, 2018

Kareemuddin M. Shaik, Wei Xu, Thamer Mohammed, Hassan Babiker, and Gautam T. Kalghatgi

Mud Pump Pressure Switch

Granted Patent: U.S. Patent 10,041,600, Grant Date: August 7, 2018

Eyadah Al-Ruothy Al-Shammary

Magnetic Induction-based Localization for Wireless Sensor Networks in Underground Oil Reservoirs

Granted Patent: U.S. Patent 10,042,077, Grant Date: August 7, 2018

Howard K. Schmidt, Ian F. Akyildiz, Shih-Chun Lin, and Abdullah A. Shehri

High Strength Polyurethane Foam Compositions and Methods

Granted Patent: U.S. Patent 10,047,188, Grant Date: August 14, 2018

Scott D. Allen, Aisa Sendijarevic, and Vahid Sendijarevic

Hydrocarbon Recovery Using Complex Water and Carbon Dioxide Emulsions

Granted Patent: U.S. Patent 10,047,275, Grant Date: August 14, 2018

Fawaz M. Al-Otaibi and Sunil L. Kokal

Densifying Carbon Dioxide with a Dispersion of Carbon Dioxide Philic Water Capsules

Granted Patent: U.S. Patent 10,047,276, Grant Date: August 14, 2018

Fawaz M. Al-Otaibi, Sunil L. Kokal, Howard K. Schmidt, and Yun Chang

Non-Acidic Exothermic Sandstone Stimulation Fluids

Granted Patent: U.S. Patent 10,047,277, Grant Date: August 14, 2018

Mohammad N. Al-Dahlan, Ayman R. Al-Nakhli, and Abdullah M. Al-Harith

High Temperature Viscoelastic Surfactant (VESs) Fluids Comprising Polymeric Viscosity Modifiers

Granted Patent: U.S. Patent 10,047,279, Grant Date: August 14, 2018

Leiming Li, Sehmus Ozden, Ghaithan A. Al-Muntasheri, Feng Liang, and B. Raghava Reddy

Carbon-based Fluorescent Tracers as Oil Reservoir Nano-Agents

Granted Patent: U.S. Patent 10,047,283, Grant Date: August 14, 2018

Mazen Y. Kanj, Mohammad H. Rashid, and Emmanuel P. Giannelis

Determining Rock Properties

Granted Patent: U.S. Patent 10,048,179, Grant Date: August 14, 2018

Bitao Lai, Hui Li, Hui-Hai Liu, and Yanhui Han

Characterization of Crude Oil by Ultraviolet Visible Spectroscopy

Granted Patent: U.S. Patent 10,048,194, Grant Date: August 14, 2018

Omer R. Koseoglu, Adnan Al-Hajji, and Gordon Jamieson

Characterizing Petroleum Product Contamination Using Fluorescence Signal

Granted Patent: U.S. Patent 10,048,205, Grant Date: August 14, 2018

Ezzat M. Hegazi, Vincent Cunningham, Christoph Stamm, and Christof Brunner

Triaxial NMR Test Instrument

Granted Patent: U.S. Patent 10,048,336, Grant Date: August 14, 2018

Mustafa Hakimuddin

Magnetic Induction-based Localization for Wireless Sensor Networks in Underground Oil Reservoirs

Granted Patent: U.S. Patent 10,048,400, Grant Date: August 14, 2018

Howard K. Schmidt, Ian F. Akyildiz, Shih-Chun Lin, and Abdullah A. Shehri

Predicting and Modeling Changes in Capillary Pressure and Relative Permeabilities in a Porous Medium due to Mineral Precipitation and Dissolution

Granted Patent: U.S. Patent 10,049,172, Grant Date: August 14, 2018

Shuo Zhang and Hui-Hai Liu

Floor Mat System and Associated, Computer Medium and Computer Implemented Methods for Monitoring and Improving Health and Productivity of Employees

Granted Patent: U.S. Patent 10,052,023, Grant Date: August 21, 2018

Samantha J. Horseman

Dual Catalyst System for Propylene Production

Granted Patent: U.S. Patent 10,052,618, Grant Date: August 21, 2018

Sulaiman S. Al-Khattaf, Arudra Palani, Tazul I. Bhuiyan, Mohammad N. Akhtar, Abdullah M. Aitani, Mohammed A. Al-Yami, and Sohel Shaikh

Process for Recovery of Light Alkyl Mono-Aromatic Compounds from Heavy Alkyl Aromatic and Alkyl-Bridged non-Condensed Alkyl Aromatic Compounds

Granted Patent: U.S. Patent 10,053,401, Grant Date: August 21, 2018

Bruce R. Beadle, Vinod Ramaseshan, Rakan S. Bilaus, Omer R. Koseoglu, and Robert P. Hodgkins

In Situ Generation of Nano-Clay Drilling Fluid

Granted Patent: U.S. Patent 10,053,611, Grant Date: August 21, 2018

Abdullah S. Al-Yami, Vikrant B. Wagle, Ziad AlAbdullatif, Faramak Almassi, Abdulaziz Bubshait, and Ali Al-Safran

Plugging and Sealing Subterranean Formations

Granted Patent: U.S. Patent 10,053,613, Grant Date: August 21, 2018

Rajendra A. Kalgaonkar, Vikrant B. Wagle, Abdullah Al-Yami, and Jin Huang

Compositions for Enhanced Fracture Cleanup Using Redox Treatment

Granted Patent: U.S. Patent 10,053,614, Grant Date: August 21, 2018

Ayman R. Nakhli, Hazim H. Abass, and Ahmed S. Otaibi

Encapsulated Nanocompositions for Increasing Hydrocarbon Recovery

Granted Patent: U.S. Patent 10,053,616, Grant Date: August 21, 2018

Yun Chang

Methods and Apparatus for Collecting and Preserving Core Samples from a Reservoir

Granted Patent: U.S. Patent 10,053,938, Grant Date: August 21, 2018

Anuj Gupta, Daniel T. Georgi, and Katherine L. Hull

System and Method for Condensate Blockage Removal with Ceramic Material and Microwaves

Granted Patent: U.S. Patent 10,053,959, Grant Date: August 21, 2018

Muhammad Ayub, Sameeh I. Batarseh, and Nabeel S. Habib

Computer Implemented Methods for Reservoir Simulation with Automated Well Completions and Reservoir Grid Data Quality Assurance

Granted Patent: U.S. Patent 10,054,712, Grant Date: August 21, 2018

Mohammed S. Al-Nuaim, Omar A. Al-Nahdi, Tareq Al-Zahrani, Khalid Al-Alwan, and Muath Al-Mulla

Field Deployable Docking Station for Mobile Robots

Granted Patent: U.S. Patent 10,054,950, Grant Date: August 21, 2018

Pablo Carrasco Zanini, Ali H. Outa, Fadl H. Abdel Latif, Brian J. Parrott, Sahejad Patel, Hassane Trigui, Ayman M. Amer, and Ali Shehri

Three-Dimensional Fluid Micromodels

Granted Patent: U.S. Patent 10,055,884, Grant Date: August 21, 2018

Ali Alkhatib, Amar Alshehri, and Ming Han

Non-Catalytic Hydrogen Generation Process for Delivery to a Hydrodesulfurization Unit and a Solid Oxide Fuel Cell System Combination for Auxiliary Power Unit Application

Granted Patent: U.S. Patent 10,056,631, Grant Date: August 21, 2018

Thang V. Pham, Hasan Imran, and Mohamed Daoudi

Enhanced Electrochemical Oxidation of Carbonaceous Deposits in Liquid Hydrocarbon Fueled Solid Oxide Fuel Cells

Granted Patent: U.S. Patent 10,056,635, Grant Date: August 21, 2018

Stamatios Souentie and Ahmad Hammad

Chair Pad System and Associated, Computer Medium and Computer Implemented Methods for Monitoring and Improving Health and Productivity of Employees

Granted Patent: U.S. Patent 10,058,285, Grant Date: August 28, 2018

Samantha J. Horseman

Processes for High Severity Fluid Catalytic Cracking Systems

Granted Patent: U.S. Patent 10,059,642, Grant Date: August 28, 2018

Mansour Al-Herz, Nathan D. Hould, Ahmed Al-Asseel, Wala Algozeeb, and Muased S. Al-Ghrami

Systems and Methods for Producing Propylene

Granted Patent: U.S. Patent 10,059,645, Grant Date: August 28, 2018

Sohel Shaikh, Aqil Jamal, and Zhonglin Zhang

Methods and Compositions for in Situ Polymerization Reaction to Improve Shale Inhibition

Granted Patent: U.S. Patent 10,059,868, Grant Date: August 28, 2018

Abeer M. Al-Olayan

Production of Upgraded Petroleum by Supercritical Water

Granted Patent: U.S. Patent 10,059,891, Grant Date: August 28, 2018

Ki-Hyouk Choi, Joo-Hyeong Lee, Mohammad S. Garhoush, and Ali H. Alshareef

Methods and Apparatus for Collecting and Preserving Core Samples from a Reservoir

Granted Patent: U.S. Patent 10,060,215, Grant Date: August 28, 2018

Anuj Gupta, Daniel T. Georgi, and Katherine L. Hull

Systems and Methods for Developing Hydrocarbon Reservoirs

Granted Patent: U.S. Patent 10,060,227, Grant Date: August 28, 2018

Waqas A. Khan, Keyang Dai, Lautaro Rayo, Abdulhamed Alfaleh, and Khalid A. Nasser

Adaptive High Integrity ESD System

Granted Patent: U.S. Patent 10,060,552, Grant Date: August 28, 2018

Abdelghani Daraiseh, Patrick Flanders, and Juan Simeoni

Characterizing Lubricant Oil Degradation Using Fluorescence Signals

Granted Patent: U.S. Patent 10,060,899, Grant Date: August 28, 2018

Ezzat M. Hegazi, Vincent Cunningham, and Maha Nour

Systems, Methods, and Apparatuses for Downhole Lateral Detection Using Electromagnetic Sensors

Granted Patent: U.S. Patent 10,061,049, Grant Date: August 28, 2018

Muhammad Arsalan, Talha J. Ahmad, and Mohamed N. Noui-Mehidi

Coupling Photovoltaic and Concentrated Solar Power Technologies for Desalination

Granted Patent: U.S. Patent 10,065,868, Grant Date: September 4, 2018

Yazeed S. Alshahrani

Systems and Methods for Producing Propylene

Granted Patent: U.S. Patent 10,065,906, Grant Date: September 4, 2018

Sohel Shaikh, Aqil Jamal, and Zhonglin Zhang

Viscosifying Proppants for Use in Carbon Dioxide-based Fracturing Fluids and Methods of Making and Use Thereof

Granted Patent: U.S. Patent 10,066,155, Grant Date: September 4, 2018

Feng Liang, Leiming Li, Ghaithan A. Al-Muntasheri, and B. Raghava Reddy

Supercritical Carbon Dioxide Emulsified Acid

Granted Patent: U.S. Patent 10,066,156, Grant Date: September 4, 2018

Bader G. Al-Harbi, Fawaz M. Al-Otaibi, and Mohammed H. Al-Khaldi

Supercritical Water Upgrading Process to Produce Paraffinic Stream from Heavy Oil

Granted Patent: U.S. Patent 10,066,172, Grant Date: September 4, 2018

Ki-Hyouk Choi, Mohammed A. Alabdullah, Ashok K. Punetha, and Emad N. Al-Shafei

Supercritical Water Upgrading Process to Produce High Grade Coke

Granted Patent: U.S. Patent 10,066,176, Grant Date: September 4, 2018

Ki-Hyouk Choi, Mohammed A. Alabdullah, Emad N. Al-Shafei, Massad S. Alanzi, Bandar K. Alotaibi, Bandar H. Alsolami, and Ali M. Alsomali

Integrated Sediment and Water Analysis Device and Method

Granted Patent: U.S. Patent 10,067,091, Grant Date: September 4, 2018

James C. Hassell and Luiz Do Val

Automatic Quality Control of Seismic Traveltime

Granted Patent: U.S. Patent 10,067,255, Grant Date: September 4, 2018

Daniele Colombo, Federico Miorelli, Diego Rovetta, and Gary McNeice

In Situ Gravitational Separation of Electrolyte Solutions in Flow Redox Battery Systems

Granted Patent: U.S. Patent 10,069,161, Grant Date: September 4, 2018

Ahmad D. Hammad and Stamatios Souentie

Auto Thermal Reforming (ATR) Catalytic Structures

Granted Patent: U.S. Patent 10,071,909, Grant Date: September 11, 2018

Jorge N. Beltramini, Moses O. Adebajo, Joao Carlos Diniz Da Costa, Gao Q. Lu, Thang V. Pham, and Sai P. Katikaneni

Combined Heavy Reformate Dealkylation-Transalkylation Process for Maximizing Xylenes Production

Granted Patent: U.S. Patent 10,071,939, Grant Date: September 11, 2018

Raed Abudawoud

Systems and Methods for Wirelessly Monitoring Well Conditions

Granted Patent: U.S. Patent 10,072,495, Grant Date: September 11, 2018

Chinthaka P. Gooneratne, Bodong Li, and Shaohua Zhou

Variable Speed Pipeline Pig with Internal Flow Cavity

Granted Patent: U.S. Patent 10,077,863, Grant Date: September 18, 2018

Mohamed A. Soliman

Hydrocracking Catalyst for Hydrocarbon Oil, Method for Producing Hydrocracking Catalyst, and Method for Hydrocracking Hydrocarbon Oil with Hydrocracking Catalyst

Granted Patent: U.S. Patent 10,081,009, Grant Date: September 25, 2018

Omer R. Koseoglu, Adnan Al-Hajji, Ali M. Al-Somali, Ali H. Al-Abdulal, Mishaal Al-Thukair, Masaru Ushio, Ryuzo Kuroda, Takashi Kameoka, Kouji Nakano, and Yuichi Takamori

Modification of Bentonite Properties for Drilling Fluids

Granted Patent: U.S. Patent 10,081,751, Grant Date: September 25, 2018

Mansour A. Al-Shafei, Akram A. Alfliow, Awadh M. Al-Mofleh, Jamal M. Al-Aamri, Syed R.A. Zaidi, and Amer A. Al-Tuwailib

Loss Circulation Material Composition Comprising Oil Swellable and Desolvated Polymer Gels

Granted Patent: U.S. Patent 10,081,756, Grant Date: September 25, 2018

B. Raghava Reddy and Matthew Hilfiger

Process for Oxidative Desulfurization and Sulfone Disposal Using Solvent Deasphalting

Granted Patent: U.S. Patent 10,081,770, Grant Date: September 25, 2018

Abdennour Bourane, Omer R. Koseoglu, and Stephane C. Kressmann

Compositions of and Methods for Making Stable Carbonaceous Nanomaterials

Granted Patent: U.S. Patent 10,082,016, Grant Date: September 25, 2018

Carlos A. Zuniga, John B. Goods, Jason R. Cox, and Timothy M. Swager

Rapidly Dehydrating Lost Circulation Material (LCM)

Granted Patent: U.S. Patent 10,087,353, Grant Date: October 2, 2018

Md. Amanullah

Oil-based Drilling Fluids Containing an Alkaline Earth Diamondoid Compound as Rheology Modifier

Granted Patent: U.S. Patent 10,087,355, Grant Date: October 2, 2018

Musarrat H. Mohammed, Hugh C. Greenwell, Manohara G. Veerabhadrappa, John A. Hall, Gasan Alabedi, Andrew Whiting, and Michael Hodder

Oxidative Desulfurization of Oil Fractions and Sulfone Management Using an FCC

Granted Patent: U.S. Patent 10,087,377, Grant Date: October 2, 2018

Abdennour Bourane, Omer R. Koseoglu, and Stephane C. Kressmann

Laser Propelled Tractor with Laser Operated Logging Tools

Granted Patent: U.S. Patent 10,087,692, Grant Date: October 2, 2018

Mohammed S. Al-Dabbous and David R. Lewis

Sealing an Undesirable Formation Zone in the Wall of a Wellbore

Granted Patent: U.S. Patent 10,087,708, Grant Date: October 2, 2018

Alwaleed A. Al-Gouhi and Nabil S. Alkhanaifer

Multilateral Well Drilled with Underbalanced Coiled Tubing and Stimulated with Exothermic Reactants

Granted Patent: U.S. Patent 10,087,736, Grant Date: October 2, 2018

Abdulrahman A. Al-Mulhem

Flow Data Acquisition and Telemetry Processing System

Granted Patent: U.S. Patent 10,088,347, Grant Date: October 2, 2018

Michael J. Black, Mohamed N. Noui-Mehidi, and Talha J. Ahmad

Combined Water Cut and Salinity Meter

Granted Patent: U.S. Patent 10,088,442, Grant Date: October 2, 2018

Michael J. Black and Mohamed N. Noui-Mehidi

Energy Performance Metric in Hydrocarbon Producing Facilities

Granted Patent: U.S. Patent 10,088,507, Grant Date: October 2, 2018

Kamarul A. Amminudin

Separation Unit for Microbial and Scale Treatment

Granted Patent: U.S. Patent 10,092,860, Grant Date: October 9, 2018

Faisal Alabbas and Anthony Kakpovbia

Auto Thermal Reforming (ATR) Catalytic Structures

Granted Patent: U.S. Patent 10,093,542, Grant Date: October 9, 2018

Jorge N. Beltramini, Moses O. Adebajo, Joao Carlos Diniz Da Costa, Gao Qing Lu, Thang V. Pham, and Sai P. Katikaneni

Sulfur Asphalt in Roofing, Damp Proofing and Water Proofing

Granted Patent: U.S. Patent 10,093,803, Grant Date: October 9, 2018

Mohammed H. Al-Mehthel, Ibnelwaleed A. Hussein, Hamad I. Al-Abdulwahhab, and Saleh H. Al-Idi

Encapsulation of an Acid Precursor for Oil Field Applications

Granted Patent: U.S. Patent 10,093,851, Grant Date: October 9, 2018

Yun Chang, Mazen Y. Kanj, and Curt Thies

Desulfurization and Sulfone Removal Using a Coker

Granted Patent: U.S. Patent 10,093,870, Grant Date: October 9, 2018

Omer R. Koseoglu, Stephane C. Kressmann, and Abdennour Bourane

Desulfurization and Sulfone Removal Using a Coker

Granted Patent: U.S. Patent 10,093,871, Grant Date: October 9, 2018

Omer R. Koseoglu, Stephane C. Kressmann, and Abdennour Bourane

Oxidative Desulfurization of Oil Fractions and Sulfone Management Using an FCC

Granted Patent: U.S. Patent 10,093,872, Grant Date: October 9, 2018

Omer R. Koseoglu, Stephane C. Kressmann, and Abdennour Bourane

Process to Recover Gasoline and Diesel from Aromatic Complex Bottoms

Granted Patent: U.S. Patent 10,093,873, Grant Date: October 9, 2018

Omer R. Koseoglu, Robert Hodgkins, Bruce R. Beadle, Vinod Ramaseshan, and Rakan S. Bilaus

Estimating Measures of Formation Flow Capacity and Phase Mobility from Pressure Transient Data under Segregated Oil and Water Flow Conditions

Granted Patent: U.S. Patent 10,094,202, Grant Date: October 9, 2018

Hasan A. Nooruddin and Noor M. Anisur Rahman

Method for Nonlinear High Salinity Water Cut Measurements

Granted Patent: U.S. Patent 10,094,796, Grant Date: October 9, 2018

Michael J. Black and Mohamed N. Noui-Mehidi

Enhancing Acid Fracture Conductivity

Granted Patent: U.S. Patent 10,100,245, Grant Date: October 16, 2018

Aslan Bulekbay and Ahmed M. Gomaa

Integrated Isomerization and Hydrotreating Process

Granted Patent: U.S. Patent 10,100,261, Grant Date: October 16, 2018

Omer R. Koseoglu

Expandable Tool Having Helical Geometry

Granted Patent: U.S. Patent 10,100,589, Grant Date: October 16, 2018

Rafael A. Lastra

Hanger for an Umbilically Deployed Electrical Submersible Pumping System

Granted Patent: U.S. Patent 10,100,596, Grant Date: October 16, 2018

Brian A. Roth, Jinjiang Xiao, and Rafael A. Lastra

Expandable Tools Using Segmented Cylindrical Sections

Granted Patent: U.S. Patent 10,100,600, Grant Date: October 16, 2018

Rafael A. Lastra

Downhole Chemical Injection Method and System for Use in ESP Applications

Granted Patent: U.S. Patent 10,100,825, Grant Date: October 16, 2018

Jinjiang Xiao and Hattan Banjar

System and Method for Power Generation with a Closed-Loop Photocatalytic Solar Device

Granted Patent: U.S. Patent 10,103,416, Grant Date: October 16, 2018

Stamatios Souentie, Ahmad D. Hammad, Konstantinos Kotsovos, and Zaki Yusuf

Synthesis of Transition Metal Adamantane Salts and Oxide Nanocomposites, and Systems and Methods, including the Salts or the Nanocomposites

Granted Patent: U.S. Patent 10,105,684, Grant Date: October 23, 2018

Manohara G. Veerabhadrappa, Hugh C. Greenwell, Gasan Alabedi, John A. Hall, and Andrew Whiting

Heat Generating Catalyst for Hydrocarbons Cracking

Granted Patent: U.S. Patent 10,105,689, Grant Date: October 23, 2018

Ali S. Ola, Hussain Al-Yami, Mark P. Kaminsky, Sohel Shaikh, and Xu Wei

Enhancement of Claus Tail Gas Treatment by Sulfur Dioxide Selective Membrane Technology

Granted Patent: U.S. Patent 10,106,410, Grant Date: October 23, 2018

Milind M. Vaidya, Iran D. Charry-Prada, Sebastien A. Duval, and Jean-Pierre Ballaguet

Enhancement of Claus Tail Gas Treatment by Sulfur Dioxide Selective Membrane Technology and Sulfur Dioxide Selective Absorption Technology

Granted Patent: U.S. Patent 10,106,411, Grant Date: October 23, 2018

Jean-Pierre Ballaguet, Milind M. Vaidya, Iran D. Charry-Prada, Sebastien A. Duval, Feras Hamad, John O'Connell, and Rashid Othman

Oxycombustion Systems and Methods with Thermally Integrated Ammonia Synthesis

Granted Patent: U.S. Patent 10,106,430, Grant Date: October 23, 2018

Mourad Younes and Tidjani Niass

Synthesis of Magnesium Adamantane Salts and Magnesium Oxide Nanocomposites, and Systems and Methods, including the Salts or the Nanocomposites

Granted Patent: U.S. Patent 10,106,482, Grant Date: October 23, 2018

Manohara G. Veerabhadrappa, Hugh C. Greenwell, Gasan Alabedi, John A. Hall, and Andrew Whiting

Oil Recovery Process Using an Oil Recovery Composition of Aqueous Salt Solution and Dilute Polymer for Carbonate Reservoirs

Granted Patent: U.S. Patent 10,106,726, Grant Date: October 23, 2018

Subhash C. Ayirala, Abdulkareem Sofi, and Ali A. Yousef

Viscosifying Modified Proppant System for Carbon Dioxide-based Fracturing Fluids

Granted Patent: U.S. Patent 10,106,733, Grant Date: October 23, 2018

Feng Liang, Leiming Li, Ghaithan A. Al-Muntasheri, and B. Raghava Reddy

Method to Remove Sulfur and Metals from Petroleum

Granted Patent: U.S. Patent 10,106,748, Grant Date: October 23, 2018

Ki-Hyouk Choi, Ashok K. Punetha, and Muneef F. Al-Qarzouh

Development of Continuous Online Salt-in-Crude Analyzer

Granted Patent: U.S. Patent 10,106,749, Grant Date: October 23, 2018

Mohamed A. Soliman

Electrical Submersible Pump Assembly for Separating Gas and Oil

Granted Patent: U.S. Patent 10,107,274, Grant Date: October 23, 2018

Mohamed N. Noui-Mehidi and Rabea Ahyad

Statistical Methods for Assessing Downhole Casing Integrity and Predicting Casing Leaks

Granted Patent: U.S. Patent 10,107,932, Grant Date: October 23, 2018

Abdulrahman Mishkhes, Mohammed Al-Ajmi, and Mubarak Al-Shammari

Systems, Computer Medium and Computer Implemented Methods for Monitoring Health of Employees Using Mobile Devices

Granted Patent: U.S. Patent 10,108,783, Grant Date: October 23, 2018

Samantha J. Horseman

Compositions with Polyaziridine Crosslinkers for Treating Subterranean Formations

Granted Patent: U.S. Patent 10,113,100, Grant Date: October 30, 2018

Matthew Hilfiger and B. Raghava Reddy

Sequential Fully Implicit Well Model with Tridiagonal Matrix Structure for Reservoir Simulation

Granted Patent: U.S. Patent 10,113,400, Grant Date: October 30, 2018

Ali H. Dogru

Apparatus and Method Employing Perforating Gun for Same Location Multiple Reservoir Penetrations

Granted Patent: U.S. Patent 10,113,401, Grant Date: October 30, 2018

Al-Waleed A. Al-Gouhi

Formation Fracturing Using Heat Treatment

Granted Patent: U.S. Patent 10,113,402, Grant Date: October 30, 2018

Khaled A. Al-Buraik

Pulsed Hydraulic Fracturing with Nanosilica Carrier Fluid

Granted Patent: U.S. Patent 10,113,406, Grant Date: October 30, 2018

Noor O. Baqader, Ahmed M. Gomaa, Rajendra A. Kalgaonkar, Jin Huang, Khalid R. Noaimi, and Ghaithan A. Al-Muntasheri

Determining Spotting Fluid Properties

Granted Patent: U.S. Patent 10,113,422, Grant Date: October 30, 2018

Md. Amanullah and Turki T. Alsubaie

Organic Rankine Cycle-based Conversion of Gas Processing Plant Waste Heat into Power

Granted Patent: U.S. Patent 10,113,448, Grant Date: October 30, 2018

Mahmoud B. Noureldin and Akram H. Kamel

Systems for Recovery and Re-Use of Waste Energy in Hydrocracking-based Configuration for Integrated Crude Oil Refining and Aromatics Complex

Granted Patent: U.S. Patent 10,113,805, Grant Date: October 30, 2018

Mahmoud B. Noureldin and Hani M. Al-Saed

System and Method for Harvesting Energy Downhole from an Isothermal Segment of a Wellbore

Granted Patent: U.S. Patent 10,115,880, Grant Date: October 30, 2018

Mohamed N. Noui-Mehidi

Environment Aware Cross-Layer Communication Protocol in Underground Oil Reservoirs

Granted Patent: U.S. Patent 10,117,042, Grant Date: October 30, 2018

Ian F. Akyildiz, Howard K. Schmidt, Shih-Chun Lin, and Abdallah A. Al-Shehri

Methods for Producing Hierarchical Mesoporous Zeolite Beta

Granted Patent: U.S. Patent 10,118,163, Grant Date: November 6, 2018

Ke Zhang

Systems and Methods for Configuring Field Devices Using a Configuration Device

Granted Patent: U.S. Patent 10,118,292, Grant Date: November 6, 2018

Brian J. Parrott and Pablo Carrasco Zanini

Hinged Vehicle Chassis

Granted Patent: U.S. Patent 10,118,655, Grant Date: November 6, 2018

Ali Outa, Brian J. Parrott, Pablo Carrasco Zanini, and Fadl H. Abdel Latif

Viscosifying Modified Proppant System for Carbon Dioxide-based Fracturing Fluids

Granted Patent: U.S. Patent 10,119,068, Grant Date: November 6, 2018

B. Raghava Reddy, Vidyasagar Adiyala, Feng Liang, Leiming Li, Ghaithan A. Al-Muntasheri, and George John

Carbon-based Fluorescent Tracers as Oil Reservoir Nano-Agents

Granted Patent: U.S. Patent 10,119,072, Grant Date: November 6, 2018

Mazen Y. Kanj, Mohammad H. Rashid, and Emmanuel P. Giannelis

Supercritical Reactor Systems and Processes for Petroleum Upgrading

Granted Patent: U.S. Patent 10,119,081, Grant Date: November 6, 2018

Ki-Hyouk Choi, Abdullah T. Alabdulhadi, and Mohammed A. Alabdullah

Measuring behind Casing Hydraulic Conductivity between Reservoir Layers

Granted Patent: U.S. Patent 10,119,396, Grant Date: November 6, 2018

Noor M. Anisur Rahman

Variable Speed Pipeline Pig with Internal Flow Cavity

Granted Patent: U.S. Patent 10,119,647, Grant Date: November 6, 2018

Mohamed A. Soliman

Recovery and Re-Use of Waste Energy in Industrial Facilities

Granted Patent: U.S. Patent 10,119,764, Grant Date: November 6, 2018

Mahmoud B. Noureldin and Hani M. Al-Saed

Method for Nonlinear High Salinity Water Cut Measurements

Granted Patent: U.S. Patent 10,119,930, Grant Date: November 6, 2018

Michael J. Black and Mohamed N. Noui-Mehidi

Sulfur Solubility in Gas Measurement System

Granted Patent: U.S. Patent 10,119,948, Grant Date: November 6, 2018

Abderrazak Traidia, Abdelmounam Sherik, Arnold Lewis, and Abduljalil Rasheed

Evaluation of Rock Boundaries and Acoustic Velocities Using Drill Bit Sound during Vertical Drilling

Granted Patent: U.S. Patent 10,120,090, Grant Date: November 6, 2018

Maher I. Marhoon and Yunlai Yang

On-Board Fuel Adjustment by Molecular Separation

Granted Patent: U.S. Patent 10,124,294, Grant Date: November 13, 2018

Esam Z. Hamad and Christos M. Kalamaras

Coordinated Water Environment Mobile Robots

Granted Patent: U.S. Patent 10,124,494, Grant Date: November 13, 2018

Ali Outa, Fadl Abdellatif, Sahejad Patel, Ammar Al Nahwi, and Ihsan Al-Taie

Methods and Compositions for in Situ Polymerization Reaction to Improve Shale Inhibition

Granted Patent: U.S. Patent 10,125,301, Grant Date: November 13, 2018

Abeer M. Al-Olayan

Filter Cake Removal Composition for Drilling Fluids and Method of Use Thereof

Granted Patent: U.S. Patent 10,125,305, Grant Date: November 13, 2018

Abdullah M. Al Moajil and Hisham A. Nasr-El-Din

Stabilization of Petroleum Surfactants for Enhancing Oil Recovery

Granted Patent: U.S. Patent 10,125,307, Grant Date: November 13, 2018

Yun Chang

Process for Producing High Quality Coke in Delayed Coker Utilizing Mixed Solvent Deasphalting

Granted Patent: U.S. Patent 10,125,318, Grant Date: November 13, 2018

Omer R. Koseoglu

Integrated Process to Produce Asphalt and Desulfurized Oil

Granted Patent: U.S. Patent 10,125,319, Grant Date: November 13, 2018

Omer R. Koseoglu and Abdennour Bourane

Integrated Heavy Liquid Fuel Coking with Chemical Looping Concept

Granted Patent: U.S. Patent 10,125,323, Grant Date: November 13, 2018

Ali Hoteit, Mourad Younes, and Aqil Jamal

Controlling Hydrocarbon Production

Granted Patent: U.S. Patent 10,125,586, Grant Date: November 13, 2018

Huseyin O. Balan, Anuj Gupta, Ali Al-Khatib, and Alberto F. Marsala

Organic Rankine Cycle-based Conversion of Gas Processing Plant Waste Heat into Power and Cooling

Granted Patent: U.S. Patent 10,125,639, Grant Date: November 13, 2018

Mahmoud B. Noureldin and Akram H. Kamel

Modified Goswami Cycle-based Conversion of Gas Processing Plant Waste Heat into Power and Cooling with Flexibility

Granted Patent: U.S. Patent 10,125,640, Grant Date: November 13, 2018

Mahmoud B. Noureldin and Akram H. Kamel

Recovery and Re-Use of Waste Energy in Industrial Facilities

Granted Patent: U.S. Patent 10,126,067, Grant Date: November 13, 2018

Mahmoud B. Noureldin and Hani M. Al-Saed

Multi-Layer Flow and Level Visualizer

Granted Patent: U.S. Patent 10,126,155, Grant Date: November 13, 2018

Fawaz A. Al-Sahan

Sequential Fully Implicit Well Modeling of Transmissibility for Reservoir Simulation

Granted Patent: U.S. Patent 10,126,465, Grant Date: November 13, 2018

Ali H. Dogru

Attachment Mechanisms for Stabilization of Subsea Vehicles

Granted Patent: U.S. Patent 10,131,057, Grant Date: November 20, 2018

Fadl H. Abdel Latif, Ali Outa, Sahejad Patel, Hassane Trigui, Abdullah Arab, Ammar Al Nahwi, and Ihsan Al-Taie

N-Hydroxyalkylated Polyamines, Methods of Making N-Hydroxyalkylated Polyamines, and Fluids Containing an N-Hydroxyalkylated Polyamine

Granted Patent: U.S. Patent 10,131,622, Grant Date: November 20, 2018

Matthew Hilfiger and B. Raghava Reddy

Method for Preventing Formation of Water-Oil Emulsions Using Additives

Granted Patent: U.S. Patent 10,131,830, Grant Date: November 20, 2018

Abduallah A. Al-Ghamdi, Aziz Fihri, Ihsan Al-Taie, Remi Mahfouz, Enrico Bovero, Mohammed Shahrani, and Haitham Aljahani

Self-Suspending Proppants for Use in Carbon Dioxide-based Fracturing Fluids and Methods of Making and Use Thereof

Granted Patent: U.S. Patent 10,131,832, Grant Date: November 20, 2018

B. Raghava Reddy, Vidyasagar Adiyala, Feng Liang, Leiming Li, Ghaithan A. Al-Muntasheri, and George John

Self-Suspending Modified Proppant System for Carbon Dioxide-based Fracturing Fluids

Granted Patent: U.S. Patent 10,131,833, Grant Date: November 20, 2018

B. Raghava Reddy, Vidyasagar Adiyala, Feng Liang, Leiming Li, Ghaithan A. Al-Muntasheri, and George John

Self-Suspending Modified Proppant System for Carbon Dioxide-based Fracturing Fluids

Granted Patent: U.S. Patent 10,131,834, Grant Date: November 20, 2018

B. Raghava Reddy, Vidyasagar Adiyala, Feng Liang, Leiming Li, Ghaithan A. Al-Muntasheri, and George John

Systems and Methods for Constructing and Testing Composite Photonic Structures

Granted Patent: U.S. Patent 10,132,758, Grant Date: November 20, 2018

Abdullah A. Al-Shahrani, Abdullah S. Al-Ghamdi, Victor Cunningham, Aziz Fihri, Enrico Bovero, Ilham Mokhtari, and Remi Mahfouz

Sensor for Measuring the Electromagnetic Fields on Land and Underwater

Granted Patent: U.S. Patent 10,132,952, Grant Date: November 20, 2018

Alberto F. Marsala and Andrew Hibbs

Field Deployable Docking Station for Mobile Robots

Granted Patent: U.S. Patent 10,133,277, Grant Date: November 20, 2018

Pablo Carrasco Zanini, Ali H. Outa, Fadl H. Abdel Latif, Brian J. Parrott, Sahejad Patel, Hassane Trigui, Ayman M. Amer, and Ali Shehri

Securing SCADA Network Access from a Remote Terminal Unit

Granted Patent: U.S. Patent 10,134,207, Grant Date: November 20, 2018

Hassan Al-Yousef, Fouad Al-Khabbaz, Zakarya Abu-Al-Saud, and Solomon Almadi

High Aspect Ratio Layered Double Hydroxide Materials and Methods for Preparation Thereof

Granted Patent: U.S. Patent 10,138,199, Grant Date: November 27, 2018

Manohara G. Veerabhadrappa, Hugh C. Greenwell, Gasan Alabedi, John Hall, and Abdullah Al-Shahrani

Polymer Compositions and Methods

Granted Patent: U.S. Patent 10,138,369, Grant Date: November 27, 2018

Jay J. Farmer

Downhole Self-Isolating Wellbore Drilling Systems

Granted Patent: U.S. Patent 10,138,686, Grant Date: November 27, 2018

Shaohua Zhou

Equal Walled Gerotor Pump for Wellbore Applications

Granted Patent: U.S. Patent 10,138,885, Grant Date: November 27, 2018

Chidirim E. Ejim, Rafael A. Lastra, and Jinjiang Xiao

Two-Stage Corrosion under Insulation Detection Methodology and Modular Vehicle with Dual Locomotion Sensory Systems

Granted Patent: U.S. Patent 10,139,372, Grant Date: November 27, 2018

Ayman Amer, Ali Shehri, and Brian J. Parrott

3D Blending and Illumination of Seismic Volumes for Automatic Derivation of Discontinuities

Granted Patent: U.S. Patent 10,139,510, Grant Date: November 27, 2018

Andrew M. Morton and Roger R. Sung

Heat Generating Catalyst for Hydrocarbons Cracking

Granted Patent: U.S. Patent 10,144,003, Grant Date: December 4, 2018

Ali S. Ola, Hussain Al-Yami, Mark P. Kaminsky, Sohel Shaikh, and Xu Wei

Loss Circulation Compositions Having Portland Cement Clinker

Granted Patent: U.S. Patent 10,144,859, Grant Date: December 4, 2018

B. Raghava Reddy

Loss Circulation Compositions Comprising Portland Cement Clinker, a Suspending Medium and a High Aspect Ratio Material

Granted Patent: U.S. Patent 10,144,860, Grant Date: December 4, 2018

B. Raghava Reddy

High Temperature Crosslinked Fracturing Fluids

Granted Patent: U.S. Patent 10,144,866, Grant Date: December 4, 2018

Ghaithan A. Al-Muntasheri, Leiming Li, Feng Liang, and B. Raghava Reddy

Hydraulically Assisted Deployed ESP System

Granted Patent: U.S. Patent 10,145,212, Grant Date: December 4, 2018

Rafael A. Lastra and Abubaker Saeed

Chemical Attenuator Sleeve

Granted Patent: U.S. Patent 10,145,217, Grant Date: December 4, 2018

Rommel E. Arias Urbina

Measuring Spatial Wettability of a Porous Material Surface by Nuclear Magnetic Resonance Gas Isotherm Technique

Granted Patent: U.S. Patent 10,145,774, Grant Date: December 4, 2018

Hyung T. Kwak and Ahmad M. Al Harbi

Computer Processing of Borehole to Surface Electromagnetic Transmitter Survey Data

Granted Patent: U.S. Patent 10,145,975, Grant Date: December 4, 2018

Alberto F. Marsala, Muhammad H. Al-Buali, Tang Biyan, and Zhanxiang He

Settable, Form-Filling Loss Circulation Control Compositions Comprising in Situ Foamed Non-Hydraulic Sorel Cement Systems and Method of Use

Granted Patent: U.S. Patent 10,150,905, Grant Date: December 11, 2018

B. Raghava Reddy

Triggering Exothermic Reaction Using Microwave

Granted Patent: U.S. Patent 10,151,186, Grant Date: December 11, 2018

Ayman R. Al-Nakhli

Location Sensor for a Rigless Deployed ESP System

Granted Patent: U.S. Patent 10,151,194, Grant Date: December 11, 2018

Brian A. Roth and Jinjiang Xiao

Nano-Level Evaluation of Kerogen-Rich Reservoir Rock

Granted Patent: U.S. Patent 10,151,714, Grant Date: December 11, 2018

Katherine L. Hull, Younane N. Abousleiman, and Sebastian Csutak

Nano-Level Evaluation of Anisotropic Mechanical Properties of Source Shale

Granted Patent: U.S. Patent 10,151,715, Grant Date: December 11, 2018

Younane N. Abousleiman and Katherine L. Hull

Magnetic Induction-based Localization for Wireless Sensor Networks in Underground Oil Reservoirs

Granted Patent: U.S. Patent 10,151,851, Grant Date: December 11, 2018

Howard K. Schmidt, Ian F. Akyildiz, Shih-Chun Lin, and Abdullah A. Shehri

Sequential Fully Implicit Well Modeling of Transmissibility for Reservoir Simulation

Granted Patent: U.S. Patent 10,151,855, Grant Date: December 11, 2018

Ali H. Dogru

Novel Modular Electrochemical Cell and Stack Design

Granted Patent: U.S. Patent 10,153,497, Grant Date: December 11, 2018

Ahmad D. Hammad, Stamatios Souentie, and Issam T. Amr

New Olefin Hydration Process Using Oscillatory Baffled Reactor

Granted Patent: U.S. Patent 10,155,707, Grant Date: December 18, 2018

Abeer Arjah, Kareemuddin Shaik, and Wei Xu

Oil Swellable, Desolvated Polymer Gels and Methods of Using the Same for Preventing Loss of Non-Aqueous Wellbore Fluids to the Subterranean Formation

Granted Patent: U.S. Patent 10,155,898, Grant Date: December 18, 2018

B. Raghava Reddy

Downhole Self-Isolating Wellbore Drilling Systems

Granted Patent: U.S. Patent 10,156,100, Grant Date: December 18, 2018

Shaohua Zhou

Novel Method to Create Connectivity between Wellbore and Subterranean Formation

Granted Patent: U.S. Patent 10,156,129, Grant Date: December 18, 2018

Fakuen F. Chang

Systems and Methods for Wirelessly Monitoring Well Conditions

Granted Patent: U.S. Patent 10,156,136, Grant Date: December 18, 2018

Chinthaka P. Gooneratne, Bodong Li, and Shaohua Zhou

Methodology to Quantify Reservoir Mineral of Chert

Granted Patent: U.S. Patent 10,156,137, Grant Date: December 18, 2018

Anas M. Al-Marzoug

A Simple Method of Measuring the Connectivity between Different Pore Types in Porous Media by Using Low-Field NMR and Fast Field Cycling NMR Technique

Granted Patent: U.S. Patent 10,156,531, Grant Date: December 18, 2018

Hyung T. Kwak, Ali A. Yousif, and Salah H. Saleh

Method of Monitoring Fluids in Subsurface Reservoirs Using Nanoparticles and Induced Polarization Effect

Granted Patent: U.S. Patent 10,156,654, Grant Date: December 18, 2018

Alberto F. Marsala, Michael S. Zhdanov, and Vladimir Burtman

System and Method for the Spectroscopic Detection of Oil Field Chemicals and Tracer Materials

Granted Patent: U.S. Patent 10,156,658, Grant Date: December 18, 2018

Shannon L. Eichmann, Sehoon Chang, and Wei Wang

Oil Swellable, Desolvated Polymer Gels and Methods of Using the Same for Preventing Loss of Non-Aqueous Wellbore Fluids to the Subterranean Formation

Granted Patent: U.S. Patent 10,160,901, Grant Date: December 25, 2018

B. Raghava Reddy

Maleic Anhydride Polymers and Methods of Treating Subterranean Formations

Granted Patent: U.S. Patent 10,160,902, Grant Date: December 25, 2018

B. Raghava Reddy

Downhole Self-Isolating Wellbore Drilling Systems

Granted Patent: U.S. Patent 10,161,192, Grant Date: December 25, 2018

Shaohua Zhou

Electromagnetic Logging Using EM Impulses from Tilted Antennas

Granted Patent: U.S. Patent 10,161,245, Grant Date: December 25, 2018

Teruhiko Hagiwara

3D Blending and Illumination of Seismic Volumes for Automatic Derivation of Discontinuities

Granted Patent: U.S. Patent 10,162,071, Grant Date: December 25, 2018

Andrew M. Morton and Roger R. Sung

SUBSCRIPTION ORDER FORM

To begin receiving the *Saudi Aramco Journal of Technology* at no charge, please complete this form.

Please print clearly.

Name _____

Title _____

Organization _____

Address _____

City _____

State/Province _____

Postal code _____

Country _____

E-mail address _____

Number of copies _____

TO ORDER

By phone/email:

Saudi Aramco Corporate Communication Support Department
JOT Distribution
+966-013-876-0498
william.bradshaw.1@aramco.com

By mail:

Saudi Aramco Corporate Communication Support Department
JOT Distribution
Box 5000
Dhahran 31311
Saudi Arabia

Current issues, select back issues and multiple copies of some issues are available upon request.

The *Saudi Aramco Journal of Technology* is published by the Saudi Aramco Corporate Communication Support Department, Saudi Arabian Oil Company, Dhahran, Saudi Arabia.

GUIDELINES FOR SUBMITTING AN ARTICLE TO THE SAUDI ARAMCO JOURNAL OF TECHNOLOGY

These guidelines are designed to simplify and help standardize submissions. They need not be followed rigorously. If you have additional questions, please feel free to contact us at CCSD. Our address and phone numbers are listed on page 84.

Length

Varies, but an average of 2,500-3,500 words, plus illustrations/photos and captions. Maximum length should be 5,000 words. Articles in excess will be shortened.

What to send

Send text in Microsoft Word format via email or on disc, plus one hard copy. Send illustrations/photos and captions separately but concurrently, both as email or as hard copy (more information follows under file formats).

Procedure

Notification of acceptance is usually within three weeks after the submission deadline. The article will be edited for style and clarity and returned to the author for review. All articles are subject to the company's normal review. No paper can be published without a signature at the manager level or above.

Format

No single article need include all of the following parts. The type of article and subject covered will determine which parts to include.

Working title

Abstract

Usually 100-150 words to summarize the main points.

Introduction

Different from the abstract in that it "sets the stage" for the content of the article, rather than telling the reader what it is about.

Main body

May incorporate subtitles, artwork, photos, etc.

Conclusion/summary

Assessment of results or restatement of points in introduction.

Endnotes/references/bibliography

Use only when essential. Use author/date citation method in the main body. Numbered footnotes or endnotes will be converted. Include complete publication information. Standard is *The Associated Press Stylebook*, 52nd ed. and *Webster's New World College Dictionary*, 5th ed.

Acknowledgments

Use to thank those who helped make the article possible.

Illustrations/tables/photos and explanatory text

Submit these separately. **Do not place in the text.** Positioning in the text may be indicated with placeholders. Initial submission may include copies of originals; however, publication will require the originals. When possible, submit both electronic versions, printouts and/or slides. Color is preferable.

File formats

Illustration files with .EPS extensions work best. Other acceptable extensions are .TIFF, .JPEG and .PICT.

Permission(s) to reprint, if appropriate

Previously published articles are acceptable but can be published only with written permission from the copyright holder.

Author(s)/contributor(s)

Please include a brief biographical statement.

Submission/Acceptance Procedures

Papers are submitted on a competitive basis and are evaluated by an editorial review board comprised of various department managers and subject matter experts. Following initial selection, authors whose papers have been accepted for publication will be notified by email.

Papers submitted for a particular issue but not accepted for that issue will be carried forward as submissions for subsequent issues, unless the author specifically requests in writing that there be no further consideration. Papers previously published or presented may be submitted.

Submit articles to:

Editor
The *Saudi Aramco Journal of Technology*
C-11B, Room AN-1080
North Admin Building #175
Dhahran 31311, Saudi Arabia
Tel: +966-013-876-0498
Email: *william.bradshaw.1@aramco.com.sa*

Submission deadlines

Issue	Paper submission deadline	Release date
Fall 2019	May 15, 2019	September 30, 2019
Winter 2019	August 1, 2019	December 31, 2019
Spring 2020	November 12, 2019	March 21, 2020
Summer 2020	February 11, 2020	June 30, 2020

NOTES:

NOTES:

NOTES:

Shale Gas Reservoir Development Strategies Using Complex Well Architectures Operating under Fixed Plateau Rate Conditions

Dr. Mari H. Alqahtani, Prof. Turgay Ertekin, and Sultan M. Almalki

ABSTRACT

In this study, artificial neural networks (ANN) were used to develop a shale gas reservoir expert system. The developed expert system provides solutions for complex wells instead of the typical massively hydraulically fractured horizontal wells (MHFHWs).

Holistic Evaluation of Water Cut in High GOR Wells for Better Production Management

Mohammad S. Al-Kadem, Dr. Dhafer A. Al-Shehri, Dr. Mohamed Mahmoud, and Dr. Rahul N. Gajbhiye

ABSTRACT

Water cut measurement becomes essential in fields where there is significant water production, especially when combined with gas production, making the measurement of all three phases difficult. In other words, water cut measured values are affected by the presence of gas near the surface. Therefore, the objective of this study is to estimate the water cut in high gas-oil ratio (GOR) wells with values greater than 2,000 standard cubic ft/stock tank barrel (scf/stb)[1].

Introduction of Real-Time Flow Measurements Opens New Paths to Overcome Challenges Encountered during the Acid Stimulation of Extended Reach Wells

Laurie S. Duthie, Hussain A. Al-Saiood, Hamad M. Almarri, and Danish Ahmed

ABSTRACT

Challenges related to matrix acid stimulation and fluid placement in extended reach horizontal wells are usually exaggerated, and demand a constant flow of innovation. The optimization of real-time fluid placement, increasing the reservoir contact and establishing uniform fluid distribution for better production/injection across the open hole interval, is one area that can benefit from these new innovations.

Estimating Transport Properties of Carbonate and Sandstone Rock Samples of Different Bedding Orientations: Digital Rock Physics and Laboratory Measurements

Abrar A. Alabbad and Dr. Jack Dvorkin

ABSTRACT

Using coarse resolution digital images to estimate the effective transport properties of a rock provides us with a large field of view, and a better representation of the rock's textural heterogeneity. In this article, a digital rock physics (DRP) workflow was developed to estimate a rock's porosity, permeability, and electrical resistivity, using the bulk density, ρ_b, and photoelectric factor, P_f, of the 3D data of nine core plugs that are comprised of sandstone. At each voxel, grain density, ρ_g, was estimated by partitioning the sample between two minerals, and as such, porosity, ϕ, was calculated.